

IPICYT

INSTITUTO POTOSINO DE INVESTIGACIÓN
CIENTÍFICA Y TECNOLÓGICA, A.C.
POSGRADO EN CIENCIAS APLICADAS

**Synthesis, Characterization and Physical
Properties of Carbon and Boron Nitride Low
Dimensional Systems**

Tesis que presenta

Eduardo Cruz Silva

Para obtener el grado de

Doctor en Ciencias Aplicadas

En la opción de

Nanociencias y Nanotecnología

Realizada bajo la codirección de:

Dr. Mauricio Terrones Maldonado

Dr. Florentino López Urías

Dr. Emilio Muñoz Sandoval



Constancia de aprobación de la tesis

La tesis **Synthesis, Characterization and Physical Properties of Carbon and Boron Nitride Low Dimensional Systems** presentada para obtener el Grado de de Doctor en Ciencias Aplicadas en la opción Nanociencias y Nanotecnología fue elaborada por **Eduardo Cruz Silva** y aprobada el **dd de mm de aaaa** por los suscritos, designados por el Colegio de Profesores de la División de Materiales Avanzados del Instituto Potosino de Investigación Científica y Tecnológica, A.C.

Dr. Mauricio Terrones Maldonado
Codirector de la tesis

Dr. Florentino López Urías
Codirector de la tesis

Dr. Emilio Muñoz Sandoval
Codirector de la tesis

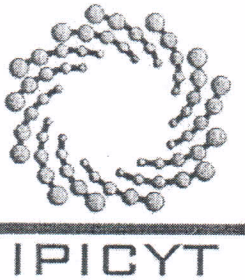
June 10, 2008



Créditos Institucionales

Esta tesis fue elaborada en la División de Materiales Avanzados del Instituto Potosino de Investigación Científica y Tecnológica, A.C., bajo la codirección de los doctores Mauricio Terrones Maldonado, Florentino López Urías y Emilio Muñoz Sandoval.

Durante la realización del trabajo el autor recibió una beca académica del Consejo Nacional de Ciencia y Tecnología (Registro No. 182491) y del Instituto Potosino de Investigación Científica y Tecnológica, A. C.



Instituto Potosino de Investigación Científica y Tecnológica, A.C.

Acta de Examen de Grado

El Secretario Académico del Instituto Potosino de Investigación Científica y Tecnológica, A.C., certifica que en el Acta 025 del Libro Primero de Actas de Exámenes de Grado del Programa de Doctorado en Ciencias Aplicadas en la opción de Nanociencias y Nanotecnología está asentado lo siguiente:

En la ciudad de San Luis Potosí a los 20 días del mes de junio del año 2008, se reunió a las 11:00 horas en las instalaciones del Instituto Potosino de Investigación Científica y Tecnológica, A.C., el Jurado integrado por:

Dr. Mauricio Terrones Maldonado	Presidente	IPICYT
Dr. Florentino López Urías	Secretario	IPICYT
Dr. Bobby G. Sumpter	Sinodal externo	ORNL, EUA
Dr. Emilio Muñoz Sandoval	Sinodal	IPICYT
Dr. Fernando Jaime Rodríguez Macías	Sinodal	IPICYT

a fin de efectuar el examen, que para obtener el Grado de:

DOCTOR EN CIENCIAS APLICADAS EN LA OPCIÓN DE NANOCIENCIAS Y NANOTECNOLOGÍA

sustentó el C.

Eduardo Cruz Silva

sobre la Tesis intitulada:

Synthesis, Characterization and Physical Properties of Carbon and Boron Nitride Low Dimensional Systems

que se desarrolló bajo la dirección de

Dr. Emilio Muñoz Sandoval
Dr. Florentino López Urías
Dr. Mauricio Terrones Maldonado

El Jurado, después de deliberar, determinó

APROBARLO

Dándose por terminado el acto a las 13:45 horas, procediendo a la firma del Acta los integrantes del Jurado. Dando fé el Secretario Académico del Instituto.

A petición del interesado y para los fines que al mismo convengan, se extiende el presente documento en la ciudad de San Luis Potosí, S.L.P., México, a los 20 días del mes de junio de 2008.

Dr. Marcial Bonilla Marín
Secretario Académico

L.C.C. Ivonne Lizette Cuevas Velez
Jefa del Departamento de Asuntos Escolares



Acknowledgements

I would like to acknowledge to Mauricio Terrones, Florentino López Urías, Emilio Muñoz Sandoval, and Humberto Terrones, who have supported me and have guided this work.

Also, to my host professors through these years: Vincent Meunier and Bobby G. Sumpter from Oak Ridge National Lab; David J. Smith and Martha R. McCartney from Arizona State University; Jean-Cristophe Charlier from Université Catholique de Louvain; Millie S. Dresselhauss and Gene Dresselhauss from Massachusetts Institute of Technology; and Riichiro Saito from Tohoku University.

To my present and past labmates and collaborators: José Manuel Romo, Ana Laura Elias, Teresa Martínez, Adalberto Zamudio, Julio Rodríguez, David Meneses, Xavier Lepró, Andrés Botello, Jéssica Campos, Aaron Morelos, Edson Hernández, David A. Cullen, Lin Gu, and Paola Ayala.

To the academic staff from IPICyT: Fernando Rodriguez, Yadira Vega, José Luis Rodriguez, Haret Rosu, Sergio Díaz, and Elisabeth Huber-Sannwald.

To the technical staff of the Advanced Materials Department: Grisel Ramírez, Daniel Ramírez, Gabriela Pérez Assaf, Lisette Noyola, Adolfo Martínez, Magdalena Martínez, and Dulce Partida.

To CONACyT, IPICyT and SOMENANO, for their financial and institutional support.

And last, but not least, to my Family.

Synthesis, Characterization and Physical Properties of Carbon and Boron Nitride Low Dimensional Systems

Eduardo Cruz Silva

Submitted for the degree of Doctor of Philosophy
June 2008

Abstract

Carbon nanotubes are versatile materials with promising applications based on their exceptional physical properties. Their applications depend strongly on the interactions that nanotubes have with their environment. In this sense, doping of carbon nanotubes, understood as the incorporation of foreign species into the nanotube lattice, has proven as a very good method for modifying and tuning their physical and chemical properties, broadening the range of possible applications.

In this work, the heteroatomic doping of multiwalled carbon nanotubes with phosphorus and nitrogen atoms is presented. These nanotubes were successfully synthesized and thoroughly characterized by several electron microscopy and microanalysis techniques, and changes in their chemical properties were surveyed by thermogravimetric analysis. In addition, first principles calculations were performed to understand the structural and electronic modifications that heteroatomic doping cause on single walled nanotubes.

In the other hand, small carbon clusters and one-dimensional nanostructures could occur during doping of carbon nanostructures by heat treatment procedures. In this context, the energetic and electronic properties of small carbon clusters of 10, 12 and 14 atoms were studied by ab initio calculations, with special interest in their spin polarization.

In addition, the vibrational properties of monoatomic carbon chains occurring during the boron doping process of double walled nanotubes and their relation with

the Coalescence Induce Mode of their Raman spectra was also studied. Finally, the properties of boron nitride nanoribbons synthesized by a substitution reaction in carbon nanostructures that exhibit a surprising metallic behavior are explored by ab initio calculations.

Contents

Abstract	ix
Acknowledgements	xi
1 Introduction	1
1.1 Carbon allotropes	1
1.2 Carbon Nanotubes structure and properties	3
1.2.1 Discovery of carbon nanotubes	3
1.2.2 Structure of carbon nanotubes	8
1.2.3 Electronic, Mechanical and Chemical properties	9
1.3 Carbon Nanotube synthesis methods	14
1.3.1 Electric arc-discharge	15
1.3.2 Laser Ablation of graphite	16
1.3.3 Electrolysis	17
1.3.4 Hydrocarbon Pyrolysis	17
1.4 Doping of carbon nanotubes	19
2 Synthesis and Characterization of Phosphorus-Nitrogen Doped Multiwalled Carbon Nanotubes	25
2.1 Importance of doping in carbon nanotubes	25
2.2 Phosphorus as an impurity in carbon systems	26
2.2.1 Phosphorus and diamond-like thin films	26
2.2.2 Phosphorus and vapor-grown carbon fibers	28
2.2.3 Phosphorus and Carbon Nanotubes	30
2.3 Synthesis of PN-doped multiwalled Carbon nanotubes	31

2.4	Characterization of PN-doped multiwalled Carbon nanotubes	34
2.5	Growth of PN-doped Carbon Nanotubes	49
2.6	Conclusions	52
3	PN Heteroatomic doping of carbon nanotubes	57
3.1	Methods	57
3.2	Graphene as a large nanotube model	58
3.2.1	Structural characteristics of doped graphene	59
3.2.2	Total energy calculations for doped graphene systems	61
3.3	P and PN doped Nanotubes	62
3.3.1	Structural changes of doped Nanotubes	62
3.3.2	Total Energy calculations for Doped Nanotubes	65
3.3.3	Electronic structure	66
3.4	Transport Properties	68
3.5	Oxidation of phosphorus doped carbon nanotubes	71
3.6	Conclusions	75
4	Boron Nitride nanoribbons	80
4.1	Introduction	80
4.2	Boron nitride nanostructures	81
4.3	Heterostructured Boron Nitride/Carbon Nanotubes	83
4.4	Could boron nitride be metallic?	85
4.4.1	Ab initio calculations of Boron nitride nanoribbons	89
4.5	Conclusions	93
5	Studies of non-graphitic carbon nanostructures	99
5.1	The Coalescence Induced Mode	99
5.2	Resonant Raman study of the CIM mode	103
5.3	<i>Ab initio</i> calculations of linear carbon chains	108
5.4	Small Carbon Clusters	111
5.5	<i>Ab initio</i> calculations of Small Carbon Clusters	116
5.6	Conclusions	123

6 Perspectives

129

List of Figures

1.1	a) Sample of bulk graphite; b) Atomic model of the unit cell of the graphite Crystal; and c) $3 \times 3 \times 2$ Supercell of graphite.	1
1.2	a) Crystalline diamond cut; b) Atomic model of diamond conventional cubic cell; and c) $3 \times 3 \times 3$ supercell of a primitive unit cell of diamond.	2
1.3	a) Image of two crossing carbon fibers synthesized by hydrocarbon pyrolysis. Notice that in the center of each fiber is a hollow carbon nanotube, covered with carbonaceous material. The arrow indicates a clear section of a SWNT with a diameter of ca. 4 nm; b) Images of hollow carbon fibers reported in 1952. Unfortunately, TEM resolution was not enough to resolve graphite lattice interspacings, and hence these fibers cannot be identified as carbon nanotubes. Adapted from [1] (a) and [2] (b).	4
1.4	a) Time-of-flight mass spectrum of the outcome of the laser ablation experiment from Kroto's report[3]. Notice the dominant peak at the $N = 60$ atoms position, followed by the peak at $N = 70$. The structural model of the truncated icosahedron is depicted on the inset; and b) bulk crystals of C_{60} obtained by evaporation from solution in benzene. The crystalline form of C_{60} is known as "fullerite", and has an fcc crystal structure with fullerene motifs on lattice sites, as shown in the inset. Adapted from [3] (a) and citeKrats90 (b).	5
1.5	a,b,c) Multiwalled carbon nanotubes with few layers, observed by Iijima and reported in [5], b) shows a double walled nanotube; and d,e,f) carbon nanotubes obtained by the large-scale production method of Ebbesen and Ajayan. Adapted from [5] (a-c) and [6] (d-f).	6

- 1.6 a) High resolution transmission electron micrographs of the entangled SWNT reported by Iijima and Ichihashi [7]; and b) high resolution image of an isolated single walled nanotube, as reported by Bethune et al. [8]. Notice that the nanotube has a carbonaceous deposits. The inset depicts an overview of the entangled nanotubes obtained by this method. Adapted from [7] (a) and [8] (b). 7
- 1.7 Structural models for achiral and chiral nanotubes. A (6,6) *armchair* nanotube (left) and a (8,0) *zigzag* nanotube (center) are depicted as examples of achiral nanotubes. 9
- 1.8 Schematic of the construction of a single walled nanotube out from a graphene sheet, indicating its main geometrical descriptors. The nanotube is obtained by wrapping the section of graphene sheet indicated by $OABB'$, and making coincide equivalent points O, A and B, B' . The vector \mathbf{C}_h is the chirality vector, while \mathbf{T} is the translational vector to create the 1D structure. Adapted from [9]. 10
- 1.9 Band structures for three different cases of single walled carbon nanotubes. a) Metallic (6,6) nanotube; b) semimetallic (12,0) nanotube; and c) semiconductive (13,0) nanotube. 11
- 1.10 a) Atomically resolved STM images of SWNT deposited over Au(111) surface. Dashed lines represent the vector \mathbf{T} , and the vector \mathbf{H} is perpendicular to the armchair direction. The angle ϕ is related to the chiral angle θ by $\theta + \phi = 30^\circ$; b) normalized dI/dV which corresponds to the density of states (DOS) of a semiconductive nanotube. Notice the shift in the Fermi energy, due to hybridization with Au orbitals. c) Energy gaps of different nanotubes, displaying an inverse relation with nanotube diameter, confirming the theoretical prediction of $E_{gap} = 2\gamma_0 a_{C-C}/d_t$. Adapted from [13]. 12

1.11 a,b) TEM images show the effect of the thermal vibrations in MWC-NTs, notice the increased blurring in nanotubes after the temperature was increased from 300K to 600K. Treacy et al. relate this vibrations to the Young modulus of nanotubes; and c-f) AFM images of a MWNT subject to lateral stress by the AFM tip. The nanotube is bent in two opposite directions, without suffering major structural damage. Adapted from [18] (a,b) and [19] (c-f). 14

1.12 a) Schematic of the arc-discharge device employed for carbon nanotube production; and b) cross-section image of a typical cathode carbonaceous deposit. Adapted from [20]. 15

1.13 a) Schematic of the laser vaporization device employed for carbon nanotube production; b) SEM images of SWNT bundles synthesized by the laser method; and c) HRTEM image of the cross-section of a SWNTs hexagonal packed rope, with nanotubes of similar diameter. Adapted from [20]. 16

1.14 a) Schematic of the electrolysis device used for production of carbon nanotubes. b) TEM image of the entanglement of carbon nanotubes. Encapsulated metal particles and amorphous carbon are also present. c) High resolution image of a nanotube synthesized by this method. Adapted from [20]. 18

1.15 Different growth models of carbon fibers proposed for the CVD method
19

2.1 Plots showing the performance of P-doped diamond thin films obtained by Epitaxial deposition over $\{1\ 1\ 1\}$ diamond surfaces. a) Doping profile showing the B-doped and P-doped interface, b) Emission Spectra of a *pn*-junction. c) Photoresistive device using a *pin*-junction and its response spectrum to solar light. Adapted from Koizumi et al. [15](a,b) and Nesladek [16](c). 28

- 2.2 a), b) Morphology of the helical carbon fibers obtained using Phosphorus as impurity for Nickel catalytic particles; c) coiled fibers yield response to variations in the impurity sources and flow rates, and d) TEM image showing nano-fibers obtained by pyrolysis of benzene, ferrocene and triphenylphosphine. Adapted from Motojima et al. [18] (a,b,c) and Ci et al. [20] (d). 29
- 2.3 (a,b) SEM images of matchstick-like nanotubes grown over anodic alumina substrates using Ni/Fe catalyst. (c,d,e) TEM images of “matchstick-like” carbon nanotubes, where the head-tail structure can be appreciated. Adapted from Jourdain et al. [24]. 32
- 2.4 Schematic diagram of the pyrolysis setup employed in the synthesis of PN-doped multiwalled carbon nanotubes. Argon is used as carrier gas. 33
- 2.5 Scanning electron microscope (SEM) images of PN-doped multiwalled carbon nanotubes (MWCNTs) from sample A. a) General overview of the sample; b) view of two nanotube mats, where the long range order can be appreciated; c) side view of a nanotube mat, the nanotube length (ca. $18\mu m$) is considerably shorter when compared to N-doped MWCNT, usually around $70\mu m$ in length. EDX spectrum of the central region of nanotubes shown in image (c). The Carbon peak was cut off to show the detail, its height is ca. 7000 counts. 35
- 2.6 SEM images of PN-doped MWCNTs from sample B. a,b) Overview of the sample; c,d) further details of the sample confirm that it is composed of nanotube mats, whose height is only a few micrometer long; e) full detail of a nanotube mat. The nanotube length is only $3.5\mu m$, and is highly disordered. f) overview of a different zone, confirming that the sample is composed mainly by MWCNT. 36
- 2.7 Comparison of the length of PN doped MWCNT with different TPP content in the hydrocarbon solution. a) Sample c, 0.0 wt% TPP, ca. $70\mu m$ long. b) Sample a, 2.5 wt% TPP, ca. $12\mu m$ long. c) Sample b, 3.3 wt% TPP, ca. $3\mu m$ long. 37

- 2.8 SEM images of PN-doped MWCNT mats indicating a root-growth process. a) A nanotube mat viewed from the top; and b) another mat viewed from the bottom; c,d) higher magnification of images a and b; e) detailed image of a nanotube mat viewed from the top. It is seen a disperse coating of amorphous carbon over the nanotube mat; and f) image of a nanotube mat viewed from the bottom, where the location of metal nanoparticles is evident, indicating a root-growth process. 39
- 2.9 Elemental maps of pure carbon (pristine), N- and PN-doped MWCNT by EDX spectroscopy. Pure carbon MWCNT map is used as control signal and is displayed on the top frame, N-doped MWCNT map is on the center frame and PN-doped MWCNT map is on the lower frame. It is observed that while nitrogen signal can be observed both in N- and PN-doped nanotubes, its signal is lost for pure carbon nanotubes. In addition, phosphorus signal is only present in PN-doped nanotubes. 40
- 2.10 Thermogravimetric scan of samples A and C, compared to a control sample of N-doped MWCNT synthesized at 850°C. The reduction in the synthesis temperature causes a shift of ca. 20°C to lower oxidation temperatures, and the inclusion of phosphorus causes a further shift of ca. 15°C. 41
- 2.11 X-ray diffractogram of PN-doped MWCNT from sample A. Two phases of iron phosphide (Fe_2P and Fe_3P) and one of iron carbide (Fe_3C , bainite) are present. 42

- 2.12 Structure and chemical composition of a PN-doped MWCNT tip.
a) High resolution image of a nanotube tip displaying the conical shape of the metal particle; b) detail of the metal particle structure. Lattice fringes are clearly seen; c) Fourier transform of the image from (b), where the bright spot indicated by the arrow represents the family of lattice planes seen on the fringes of image (b); d) high angle annular dark field (HAADF) STEM image of a nanotube tip. The EDX elemental line profile is displayed, showing an homogeneous composition of Fe and P within the catalytic particle. 44
- 2.13 High resolution transmission electron microscope (HRTEM) images of sample A. a) Low magnification image displaying the general overview of a nanotube mat; b) image displaying the bamboo structure of nanotubes; c) high resolution image of a nanotube wall, displaying a high graphitization degree; d) image of a typical nanotube tip revealing a conical catalytic particle; and e) high resolution image of the interface of the metal particle and the carbon nanotube from d). . . . 45
- 2.14 Energy filtered elemental maps of PN-doped MWCNTs, with maps for carbon (C), iron (Fe), and phosphorus (P). It can be observed that the metallic particles are composed of an iron phosphide phase, while the signal of phosphorus is not strong enough to appear on the nanotube lattice. 46
- 2.15 Energy filtered elemental maps of the metallic catalytic particles of PN-doped MWCNT, with maps for oxygen (O), iron (Fe), and phosphorus (P). The presence of oxygen in the far end of the nanotube tip could be due to air-oxidation or acquired from the quartz substrate during growth. 47
- 2.16 Electron energy loss spectrum of a PN-doped MWCNT from sample A, obtained from the spot marked in the high angle annular dark field (HAADF) image. The position of the carbon edge is clear, while small signals from nitrogen and phosphorus are masked by the tail of the carbon edge and the inelastic scattering peak, respectively. . . . 48

- 2.17 Elemental line profiles of PN-doped MWCNT. a) Phosphorus (P), silicon (Si) and carbon (C) profiles, displaying a phosphorus profile that corresponds to carbon signal; b) Nitrogen (N) and carbon (C) profiles, displaying a clear content of gaseous nitrogen in the nanotube core, while also displaying traces of nitrogen within nanotube walls. 49
- 2.18 Root growth model proposed for the PN doped nanotubes. A metal particle attached to the substrate (a) nucleates a graphitic layer (b,c), which also includes P and N present in the environment. The stress induced by curvature and a high surface diffusion rate causes the nanotube to start growing from this particle (d). The diffusion through the catalyst of C, P, and N causes the formation of a graphite layer in the interior of the nanotube, which in turn displaces the growing nanotube (e) and crates a bamboo compartment (f). the repetition of this process leads to a bamboo-like PN doped nanotube. 50
- 3.1 Molecular models of the studied systems, displaying their full supercell size. a) 7x7 graphene supercell. b) 5 cells of a (10,0) zigzag nanotube. c) 8 cells of a (6,6) armchair nanotube. 59
- 3.2 Molecular models of the doped graphene structures after relaxation. The hexagonal red line indicates the position of the undoped graphene network. 60
- 3.3 Molecular model for zigzag doped carbon nanotubes. a) Substitutional nitrogen; b) substitutional phosphorus; and c) heteroatomic P-N doped nanotube. 63
- 3.4 Molecular model for armchair doped carbon nanotubes. a) Substitutional nitrogen; b) substitutional phosphorus; and c) heteroatomic P-N doped nanotube. 64
- 3.5 Bands structure for zigzag carbon nanotubes. From left to right: pristine (10,0) nanotube, nitrogen doped (10,0), phosphorus doped (10,0) and PN-doped (10,0). The presence of new states is indicated by arrows. The energies are relative to the pure carbon nnaotube Fermi level, and the dotted ines are the Fermi level on each system. 67

- 3.6 Bands structure for armchair carbon nanotubes. From left to right: pristine (6,6) nanotube, nitrogen doped (6,6), phosphorus doped (6,6) and PN-doped (6,6). The presence of new states is shown by arrows. The energies are relative to the pure carbon nnaotube Fermi level, and the dotted ines are the Fermi level on each system. 68
- 3.7 Density of states for (6,6) armchair nanotubes (top) and (10,0) zigzag nanotubes(bottom). The reference Energy is the Fermi level for pristine nanotubes. 69
- 3.8 Plots of the wavefunctions for localized states around the defect sites for nitrogen, phosphorus and phosphorus-nitrogen doped (6,6) nanotubes. It can be seen that in the phosphorus-doped case, the state is highly localized around the phosphorus atom, while in the PN-doped case, the localization is higher for the top valence band, although in th bottom conduction band there is still some localization around PN defect. 70
- 3.9 Calculated conductance of nitrogen-doped (6,6) (left) and (10,0) (right) carbon nanotubes, compared to the pristine nanotube conductance, in dashed red line (top). Electronic density of states (DOS) for the above mentioned nanotubes, compared to the pristine nanotube DOS, shown in dashed red line (bottom). It can be observed that for the armchair nanotube, the states created by the extra nitrogen electron (shown as peaks in the DOS) cause two reductions in the nanotube conductance when compared to pristine nanotubes, similar to the results of Choi et al. [12]. 71
- 3.10 Calculated conductance of phosphorus doped (6,6) (left) and (10,0) (right) carbon nanotubes, compared to the pristine nanotube conductance, in dashed red line (top). Calculated density of states (DOS) for the above mentioned nanotubes, compared to the pristine nanotube DOS, shown in dashed red line (bottom). 72

- 3.11 Calculated conductance of phosphorus-nitrogen doped (6,6) (left) and (10,0) (right) carbon nanotubes, compared to the pristine nanotube conductance, in dashed red line (top). Calculated density of states (DOS) for the above mentioned nanotubes, compared to the pristine nanotube DOS, shown in dashed red line (bottom). 72
- 3.12 Oxidation of a (6,6) P-doped carbon nanotube. It is observed that oxygen atoms bond to the fourth orbital of the phosphorus atom. . . 73
- 3.13 Band structure of an oxidized (6,6) P-doped nanotube and calculated conductance of the same nanotube, compared to an unoxidized P-doped nanotube and a pristine nanotube 74
- 4.1 Structural models of boron nitride allotropes. The hexagonal phase (top left) is structurally similar to graphite, while the cubic phase (top right) exhibits a structure similar to diamond. The wurtzite-like structure (bottom) is a high pressure phase that corresponds to the corrugated or “buckled graphite” structure. 81
- 4.2 Band structure (left) and density of states (right) for a single layer of hexagonal Boron Nitride, showing that the material is an insulator with a calculated band gap of ca. 4.5 eV. Notice that this local density approximation underestimates the energy gap, and that other studies using the quasiparticle approximation reveal a band gap of 6.0 eV for this system. 82
- 4.3 Densities of electronic states for heterostructured boron nitride / carbon (5,5) nanotubes with different compositions. It can be seen that the energy gap can be tuned depending on the composition of B, C and N within the nanotube. 84

- 4.4 Boron Nitride nanospheres resembling sea urchin morphologies. a,b) SEM images displaying the morphology of the synthesized nanospheres. The arrows in a) show small peaks in the sphere surface. c,d) TEM images displaying the porous morphology of the nanospheres. It can be seen in d) that the spheres are composed of multiple ribbon like structures e) to h) Elemental map for a BN nanosphere, confirming that the substitution reaction was complete and the sphere is composed only of boron nitride. i) EEL spectrum clearly displaying the boron and nitrogen edges, while carbon edge is not visible. 86
- 4.5 HRTEM images of the surface of a BN nanourchin. It can be seen that BN layers protrude from the surface with exposed edges. The image shown in d) has a higher magnification and displays the hexagonal pattern of BN. 87
- 4.6 a) Field emission I-V curves for BN nanospheres films. The inset shows the Fowler-Nordheim for the I-V curves obtained at $220\mu\text{m}$ and $270\mu\text{m}$. b) Current stability of the BN nanourchin films, showing a relative stability for periods over 9000 s. 88
- 4.7 Hexagonal Boron Nitride nanoribbons with armchair (top) and zigzag (bottom) edges. It can be seen that the atoms near the edge are displaced from their ideal positions 90
- 4.8 Band structure for hydrogenated and free-edge armchair and zigzag boron nitride nanoribbon. After dehydrogenation, a pair of dangling bond states, indicated with arrows, appear below the bottom conduction band for armchair ribbons and just above the valence edge state in zigzag ribbons, and cross the Fermi Level. 92
- 4.9 Charge density plots of the wavefunctions associated with the dangling bond states (top) and the edge states (bottom) 93
- 5.1 Raman spectra of double-walled carbon nanotubes taken at 2.33eV, either pristine or at different heat treatment temperatures (HTT). a) Without boron doping, and b) with boron doping. Adapted from [1] 100

- 5.2 High resolution transmission electron micrographs of undoped (a-c) and boron doped (d-i) double walled carbon nanotubes treated at different temperatures. Pristine undoped DWNT (a), DWNT treated at 1500 (b), and 2000°C (c). Boron doped DWNT, treated at 1300 to 1700°C (d-h) and 2000°C (i). Adapted from Endo et al. [3]. . . . 102
- 5.3 a) Deconvolution of the CIM feature obtained at $E_{\text{laser}}=2.2$ eV at different locations of an undoped sample heat treated at 1500°C. Black lines are the collected spectra, blue lines represent the Lorentzian functions and the green lines represent the fitted spectra. b) Frequency vs E_{laser} for all Lorentzian peaks used to fit the CIM feature. Notice the distribution of frequencies around four main values, indicated with continuous lines. c) Resonant Raman profile for the CIM feature of the undoped sample heat treated at 1500°C, and d) for the boron-doped sample heat treated at 1300°C. The arrows indicate the resonance local maxima with E_{laser} . Adapted from Fantini et al. [8]. 104
- 5.4 Low frequency (a) and first-order Raman spectra (b) from DWNT thermally treated at 1500°C, and their air-oxidized samples at 400, 500 and 600°C. c) Profile of the CIM intensity values with different oxidation temperatures. d) Schematic of the stacking of DWNT as derived from their XRD patterns. 105
- 5.5 Low frequency (a) and first-order Raman spectra (b) from DWNT thermally treated at 1500°C, and their chemically doped samples after treatment in sulfuric acid at room temperature (RT) and 100°C for 1 minute. 107
- 5.6 Relaxed Structures of carbon chains containing from 3 to 10 atoms. Notice that the outer bonds are longer due to the dangling bonds in the outer atoms. 108

- 5.7 Frequencies for the normal vibrational stretching modes for free-standing and fixed-end linear carbon chains. Black lines represent the free chains, while the red lines represent carbon chains with their outer atoms held at fixed positions, resembling atoms that have reduced mobility due to bonding to larger carbon structures. 109
- 5.8 Top-left: Geometries of all sp^2 -like carbon clusters with 10 atoms and one π electron per atom. Isomers d to i exhibit a ferrimagnetic ground state. Top-right: Geometries of sp^2 -like carbon clusters with 12 atoms that exhibit a ferrimagnetic ground state. Twenty additional structures were analyzed, displaying a ground state with $S = 0$. Bottom: Ferrimagnetic geometries found for carbon clusters with 14 atoms. All structures have three-coordinated carbon atoms that form highly strained structures, such as carbon chains, as well as triangular and squared rings. 115
- 5.9 Relaxed structures for 10 (letters) and 12 atom (numbers) carbon clusters after relaxation. All stable clusters are shown for the 10 atom case, where clusters a, g, and h have a total spin of $S = 1$ and cluster c has a total spin of $S = 2$. The prismane-like cluster with pentagonal rings is in position g. In the 12 atom case, only spin-polarized clusters that were stable after relaxation are shown. In this case, only cluster number 3 has a total spin of $S = 2$, while the rest have $S = 1$ 117
- 5.10 Stable structures for 14 atom carbon clusters that exhibit spin-polarization after relaxation. Clusters A2 and E8 exhibit a total spin of $S = 2$, while the rest have $S = 1$. Notice the presence of the prismane-like cluster in position E3, with heptagonal rings. 120

- 5.11 Electronic Density of States (DOS) calculated for (a) an isolated pentagonal prismane-like molecule (iso-g from figure 5.9. b) Prismane-like cluster inside a C_{60} molecule, (c) a C_{70} molecule, and (d) a C_{80} fullerene. Each figure has independent Spin-up (black) and Spin-down (red) plots. The system was first relaxed using conjugate gradient. The Fermi level has been shifted to zero, and represented by the vertical dashed line. 122

List of Tables

1.1	Parameters for Carbon Nanotubes.	10
2.1	Synthesis conditions of the samples selected for characterization. . . .	34
3.1	Total and binding energies for different doped graphene systems, as well as the energy cost associated with the particular defect. All energies are in eV.	62
3.2	Total and binding energies for (10,0) and (6,6) nanotube doped systems, as well as the energy cost associated with the particular defect. All energies are in eV.	65
5.1	Vibrational stretching mode frequencies (ω_{chain}) and gap energy (E_{gap}) for carbon chains with fixed ends, calculated for carbon chains containing 3–7 atoms. The Raman-active modes are boldface.	110
5.2	Values for dimensionless parameter β for which C_{10} cluster exhibit ferrimagnetic ground state.	113
5.3	Values for dimensionless parameter β for which C_{12} cluster exhibit ferrimagnetic ground state.	114
5.4	Total and Binding Energy for several C_{10} clusters, sorted by increasing binding energy. ΔE is the difference in binding energy with the most stable structure. Total spin is also calculated.	118
5.5	Total and Binding Energy for several C_{12} clusters sorted by increasing binding energy. ΔE is the difference in binding energy with the most stable structure. Total spin is also calculated.	119

5.6	Total and Binding Energy for several C ₁₄ clusters sorted by increasing binding energy. ΔE is the difference in binding energy with the most stable structure. Total spin is also calculated.	121
-----	--	-----

Chapter 1

Introduction

1.1 Carbon allotropes

Pure carbon occurs in several structural forms, or allotropes. The most commonly known allotropes of carbon are Graphite and Diamond. Graphite is a flaky black mineral, which is an electrical conductor; and is the most stable form of carbon under standard conditions. Its structure can be described as a layered material, composed of hexagonal sheets stacked by Van der Waals interactions (see figure 1.1). Due to these weak interlamellar couplings, graphite is often used as a solid dry lubricant.

Carbon atoms in graphite bond with a sp^2 hybridization, that is, each atom has three co-planar bonds with a separation of 120° with a length of 1.42 \AA , creating the hexagonal lattice of graphite, and the interlayer separation is 3.35 \AA . The fourth

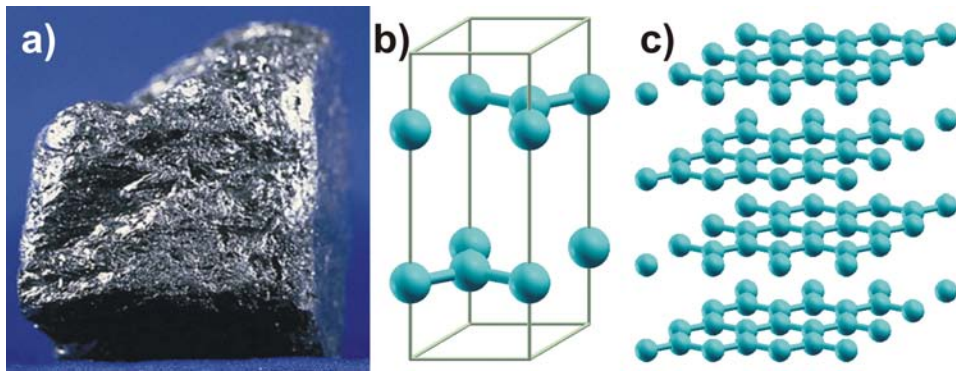


Figure 1.1: a) Sample of bulk graphite; b) Atomic model of the unit cell of the graphite Crystal; and c) $3 \times 3 \times 2$ Supercell of graphite.

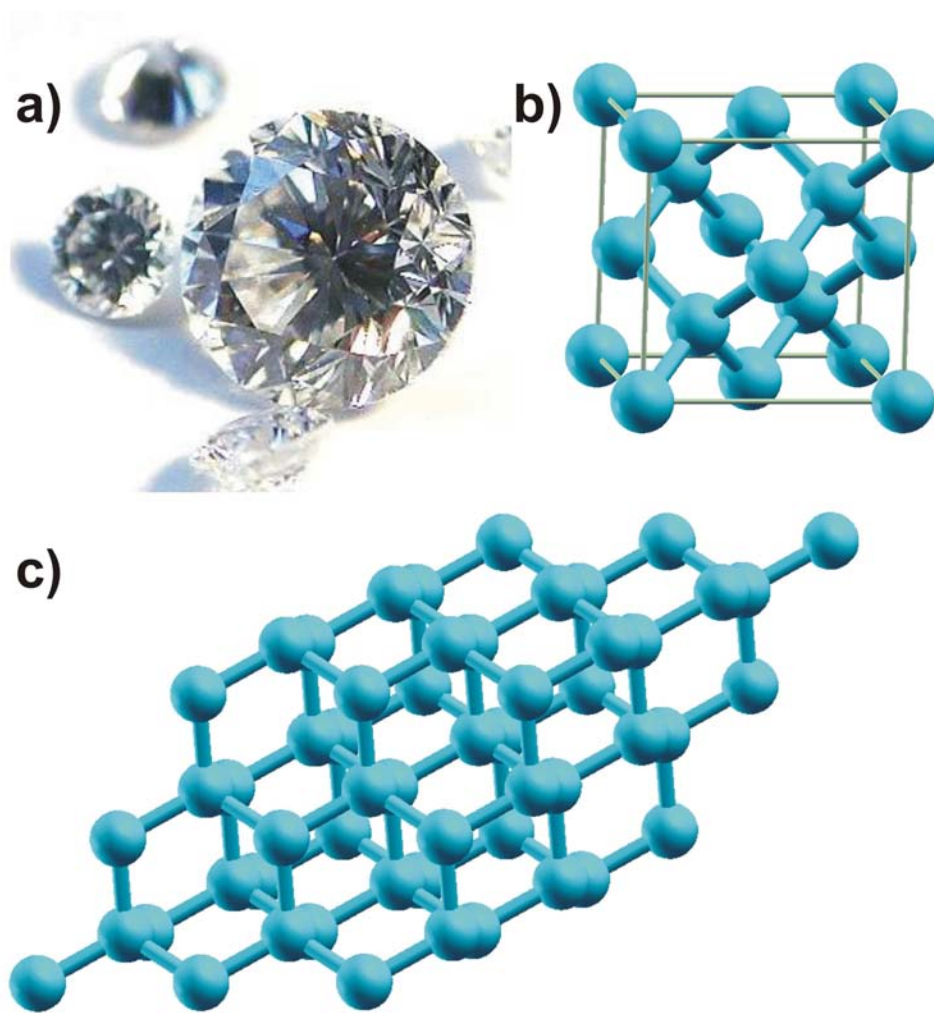


Figure 1.2: a) Crystalline diamond cut; b) Atomic model of diamond conventional cubic cell; and c) $3 \times 3 \times 3$ supercell of a primitive unit cell of diamond.

electron in each atom create an out-of-plane π -electron network that is strongly delocalized, and which is responsible of the electrical conductivity present in graphite, and contributes to the Van der Waals forces that bind layers together.

In contrast to graphite, diamond is the hardest natural material. In its pure form, is a transparent and colorless material with a high thermal conductivity and a high light dispersion. Due to its physical properties, diamond has been highly valued as a gemstone. Its hardness has also given to diamond important industrial applications, most of the diamond that can be used as a gemstone (due to its size, color or faults) ends up as industrial diamond, specially in cutting, drilling, grinding, and polishing tools and applications. Its structure is based in a sp^3 hybridization,

in which each carbon atom is bonded to other four atoms following the zincblende structure (see figure 1.2), with a bond length of 1.545 Å.

1.2 Carbon Nanotubes structure and properties

1.2.1 Discovery of carbon nanotubes

Carbon Nanotubes were first observed more than thirty years ago by Oberlin, Endo, and Koyama [1] in 1976, while studying the growth process of carbon fibers by benzene decomposition at 1100°C. The authors found that the growth consisted of two stages, first, the catalytic growth of a thin carbon filament from a metal particle; which was subsequently thickened by the deposition of carbonaceous material over the primary filament, and hence it was called “filamentous growth”. They published an image of a single walled carbon nanotube with a diameter of ca. 4 nm in diameter (see figure 1.3a).

A previous observation of hollow carbon nanofibers formed by CO decomposition over an iron substrate was reported in 1952 by Radushkevich and Lukyanovich [2]. Although the structure of tubular graphitic carbon with a catalytic metal particle at the tip is very similar to a multiwalled carbon nanotube (figure 1.3b), the TEM resolution at that time was not able to resolve individual graphite layers, and therefore the structure could not be fully identified from a similar carbon scroll (that is, a graphene layer rolled without coincident ends).

In 1985, a new allotropic form of carbon was discovered by Kroto et al. [3]. The authors were interested in the formation of long carbon-chain molecules known as polyynes. For this purpose, graphite was evaporated in a laser ablation experiment under an helium flow, and then the outcoming carbon material was photoionized and detected on a time-of-flight mass spectrometer. It was found that the mass spectra was dominated by carbon clusters of 60 atoms (see figure 1.4).

The authors proposed that a truncated icosahedron (i.e, a soccer football) was the most likely structure for the C60 cluster, which they named “Buckminsterfullerene”, in honor to Richard Buckminster Fuller, an architect who designed several geodesic structures, to which the C60 cage is related. The proposed structure was correct,

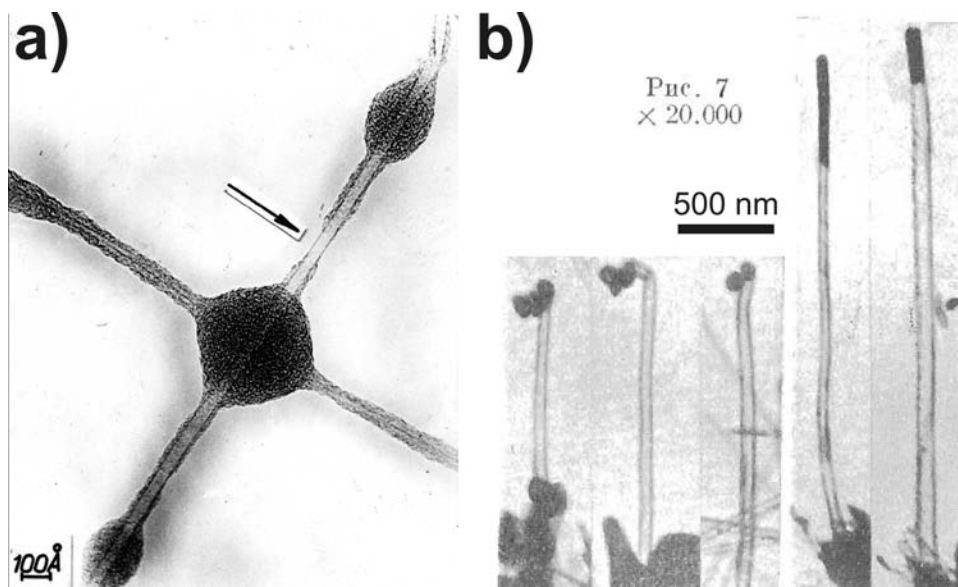


Figure 1.3: a) Image of two crossing carbon fibers synthesized by hydrocarbon pyrolysis. Notice that in the center of each fiber is a hollow carbon nanotube, covered with carbonaceous material. The arrow indicates a clear section of a SWNT with a diameter of ca. 4 nm; b) Images of hollow carbon fibers reported in 1952. Unfortunately, TEM resolution was not enough to resolve graphite lattice interspacings, and hence these fibers cannot be identified as carbon nanotubes. Adapted from [1] (a) and [2] (b).

and a new research field of carbon nanostructures, including other cage-like clusters, was launched; and the family of carbon cage-like molecules was simply called “fullerenes”.

A few years later, Kratschmer et al. [4] reported a synthesis and purification method that was capable of producing C₆₀ in bulk quantities, that involved the evaporation of graphite electrodes in an arc discharge device carried out in an inert helium atmosphere. The soot obtained was subsequently dispersed in benzene, where the C₆₀ molecule dissolves to form a wine-red solution. This solution was then separated from the undissolved soot and evaporated, yielding a new crystalline form of C₆₀. This crystal is an fcc lattice with C₆₀ molecules, and is called “fullerite” (see figure 1.4).

In 1991, Iijima [5] found that graphitic carbon needles with diameters ranging from 4–30 nm were grown on the negative electrode used in a d.c. arc-discharge experiment on a reactor similar to that of Kratschmer et al. [4], but with lower helium

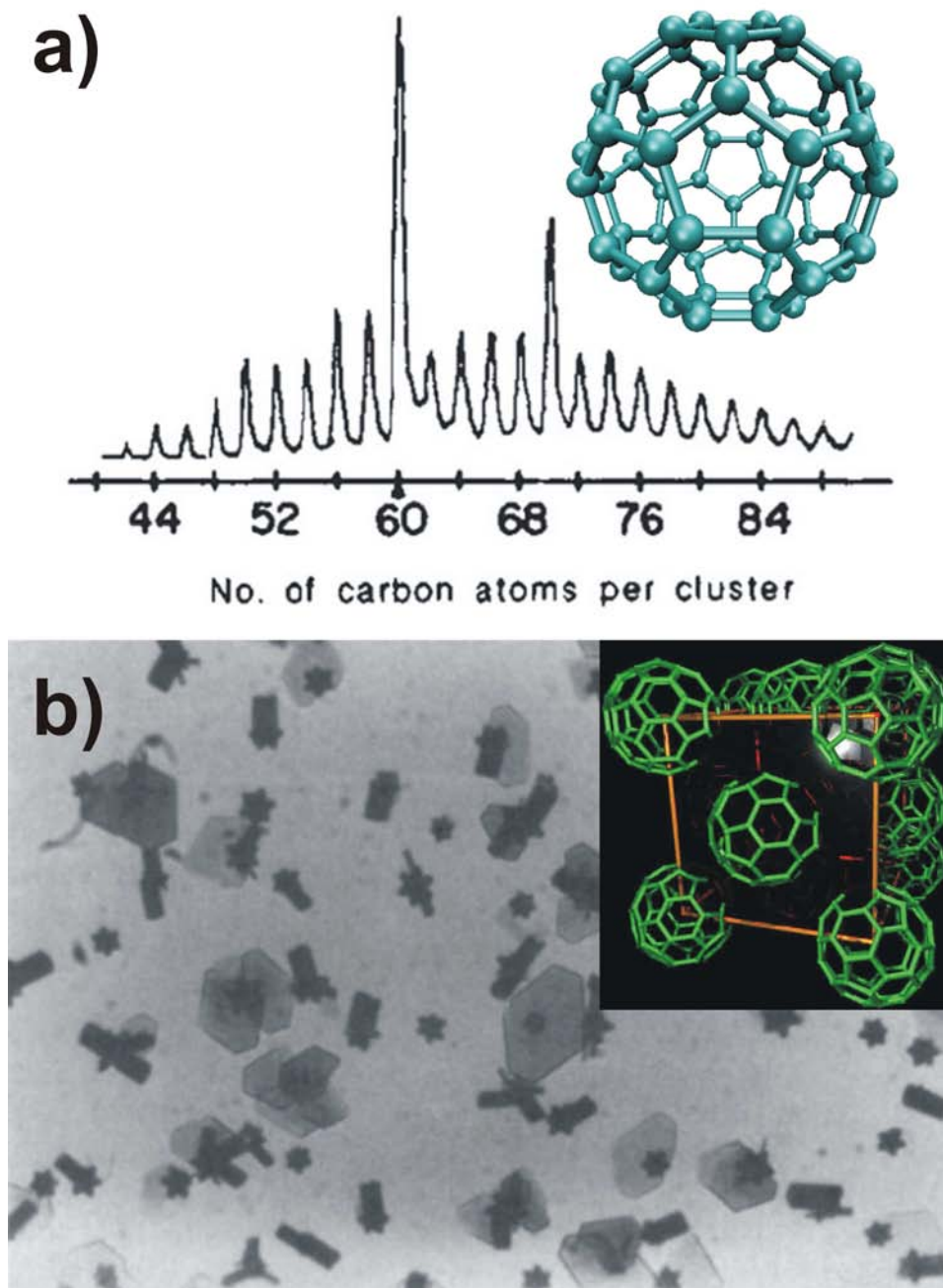


Figure 1.4: a) Time-of-flight mass spectrum of the outcome of the laser ablation experiment from Kroto's report[3]. Notice the dominant peak at the $N = 60$ atoms position, followed by the peak at $N = 70$. The structural model of the truncated icosahedron is depicted on the inset; and b) bulk crystals of C_{60} obtained by evaporation from solution in benzene. The crystalline form of C_{60} is known as "fullerite", and has an fcc crystal structure with fullerene motifs on lattice sites, as shown in the inset. Adapted from [3] (a) and citeKrats90 (b).

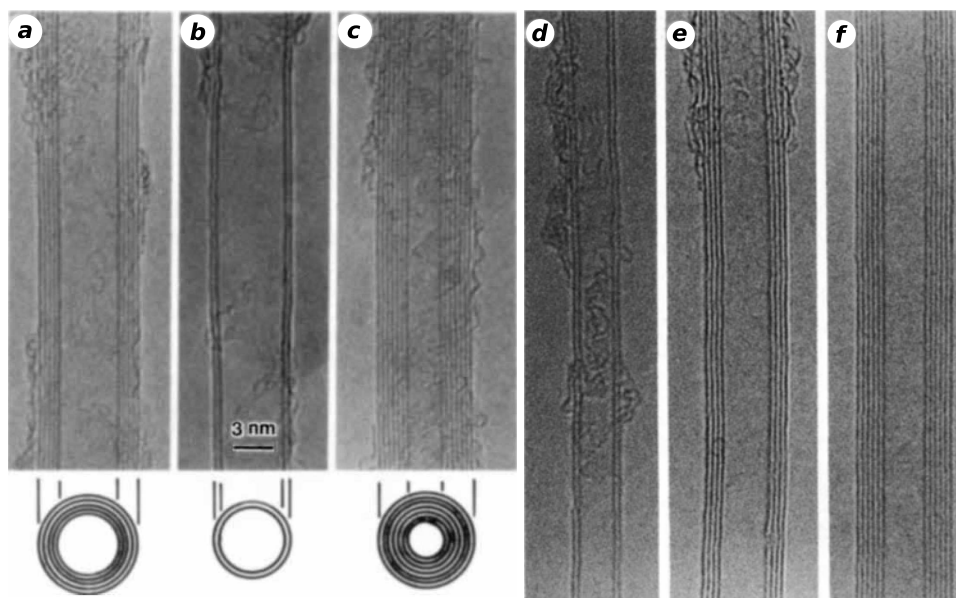


Figure 1.5: a,b,c) Multiwalled carbon nanotubes with few layers, observed by Iijima and reported in [5], b) shows a double walled nanotube; and d,e,f) carbon nanotubes obtained by the large-scale production method of Ebbesen and Ajayan. Adapted from [5] (a-c) and [6] (d-f).

pressure. These needles were characterized by high resolution electron microscopy, finding they were hollow fibers with equal number of graphite layers on each side, from which he deduced these fibers had tubular structure (figure 1.5). From electron diffraction images, Iijima was able to conclude that the structure was indeed coaxial tubes, and that each layer had a different chirality, from which he denominated nanotubes as “helical microtubules”.

Only a year later, Ebbesen and Ajayan [6] reported a synthesis method capable of producing multiwalled carbon nanotubes in large scale. The method consisted in an arc-discharge device, under an inert gas atmosphere with a controlled pressure. A potential of ca. 18 V is applied to two graphite rods of different diameter (6 and 8 mm), while they are kept at a very small distance (ca. 1 mm). A discharge occurs with a current close to 100 A, and a plasma is formed between the rods. The smaller rod is consumed, while in the larger rod a carbonaceous deposit containing nanotubes is formed. The authors found optimum growth conditions for 500 torr of helium pressure. Although the potential did not seem to have a major effect when varied from 10 to 18 V, it was found that yield was reduced when applying

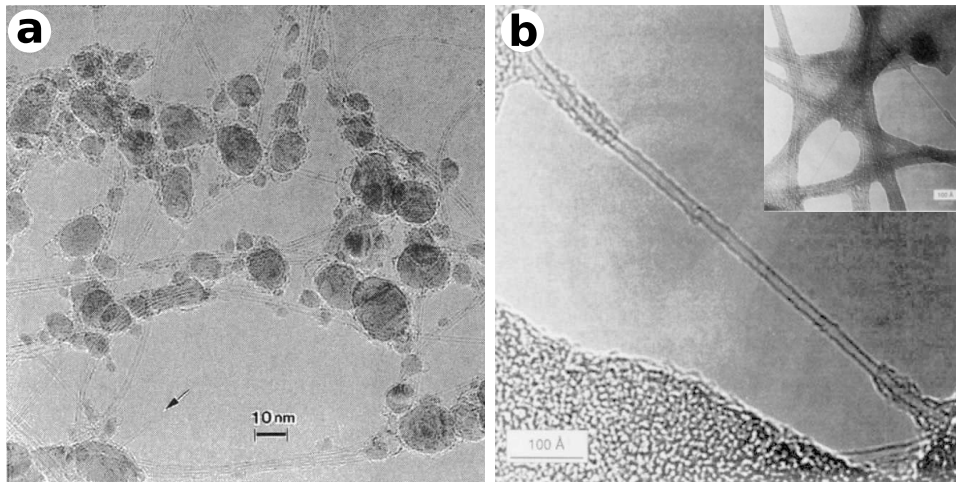


Figure 1.6: a) High resolution transmission electron micrographs of the entangled SWNT reported by Iijima and Ichihashi [7]; and b) high resolution image of an isolated single walled nanotube, as reported by Bethune et al. [8]. Notice that the nanotube has a carbonaceous deposits. The inset depicts an overview of the entangled nanotubes obtained by this method. Adapted from [7] (a) and [8] (b).

alternate current. The diameter of the produced nanotubes were 2–20 nm, and they were several micrometers long. Also, the author found that the fibres grew aligned parallel to the electric current direction.

In 1993, two independent groups reported at the same time the successful synthesis of single walled carbon nanotubes (SWCNT). In both cases, the synthesis involved the presence of transition metals. Iijima and Ichihashi used an arc-discharge device where the electrodes were placed vertically. The upper electrode was the anode, a 10 mm carbon rod, while the cathode was a 20 mm carbon rod with a hole filled with a small iron piece. The chamber is filled with a mixture of argon and methane. The potential to generate the arc was 20 V, with a 200 A current between electrodes. The vaporization of iron takes place during the evaporation of carbon and consequent production of soot. The produced nanotubes were arranged as bundles, although isolated tubes were also present (figure 1.6a). The diameters of the single walled nanotubes varied from 0.7 to 1.6 nm [7]

At the same time, Bethune et al. also found a synthesis route to SWCNT while working in the synthesis of metallofullerenes [8]. They also used an arc-discharge device with 6 mm diameter carbon rods. In this case, 4 mm diameter holes were

bored in the anodes, and filled with powdered metals and graphite (ca. 2 at. % of Co, Fe or Ni), and vaporized with a current of 95–105 A in an helium atmosphere with a pressure of 100–500 torr. When using cobalt, the author found that the soot deposited changed its consistency from *crumbly* to *rubbery* and also spiderweb-like deposits were present. Transmission electron microscopy images of the web-like material showed the presence of small fibers consisting of bundles of SWCNTs (see figure 1.6b).

1.2.2 Structure of carbon nanotubes

A single walled carbon nanotube can be obtained by rolling a section of a graphene layer into a cylindrical shape. This can be done in many different ways, and a system to identify all the different geometries is needed. Nanotubes can be classified by their geometrical properties in two groups: achiral and chiral. An achiral nanotube is that whose mirror image has an identical structure, and these are further classified as *zigzag* or *armchair*, based on the shape of the nanotube cross-section (see figure 1.7). An achiral nanotube mirror image is not identical to the original tube due to their helicity.

The structure of the single walled nanotube is defined by the vector which corresponds to equator of the nanotube (vector \overrightarrow{OA} in figure 1.8). The nanotube is formed by rolling the graphene sheet defined by the points O, A, B and B' ; and making them coincide by pairs O, A and B, B' . The vector \overrightarrow{OA} is known as *chiral vector* \mathbf{C}_h , and vector \overrightarrow{OB} is the *translational vector* \mathbf{T} . The chiral vector \mathbf{C}_h can be expressed in terms of the graphene unit cell vectors \mathbf{a}_1 and \mathbf{a}_2 as

$$\mathbf{C}_h = n\mathbf{a}_1 + m\mathbf{a}_2 \equiv (n, m) \quad (1.1)$$

where the indices n, m are integers, and $0 \leq |m| \leq n$. An armchair nanotube corresponds to the case $n = m$, while a zigzag nanotube has $m = 0$. All other (n, m) chiral vectors correspond to chiral nanotubes.

The diameter of the carbon nanotube is related to the length of the chiral vector as:

$$d_t = L/\pi, \text{ and } L = |\mathbf{C}_h| = \sqrt{\mathbf{C}_h \cdot \mathbf{C}_h} = a\sqrt{n^2 + nm + m^2} \quad (1.2)$$

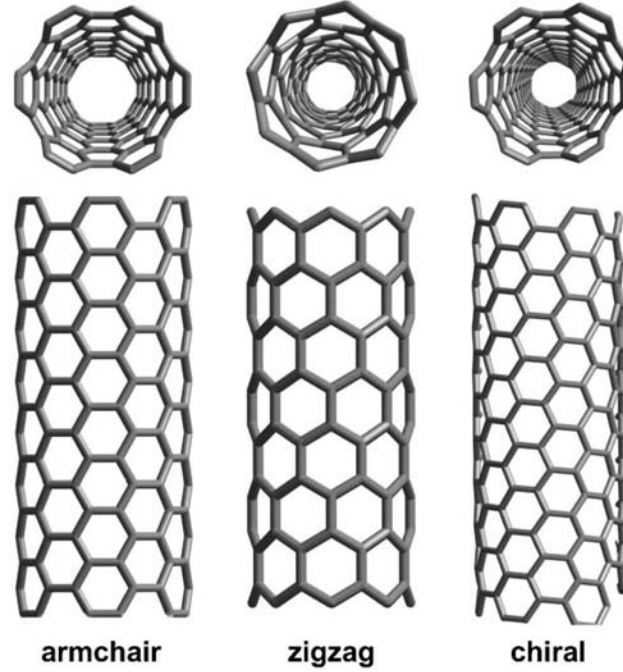


Figure 1.7: Structural models for achiral and chiral nanotubes. A (6,6) *armchair* nanotube (left) and a (8,0) *zigzag* nanotube (center) are depicted as examples of achiral nanotubes.

where a is the length of the unit vector \mathbf{a}_1 , related to the C-C bond length by $a = \sqrt{3}a_{C-C} \approx 2.46 \text{ \AA}$.

The chiral or helicity angle θ is defined as the angle between the chiral vector and \mathbf{a}_1 , and hence:

$$\cos \theta = \frac{\mathbf{C}_h \cdot \mathbf{a}_1}{|\mathbf{C}_h| |\mathbf{a}_1|} = \frac{2n + m}{2\sqrt{n^2 + nm + m^2}} \quad (1.3)$$

with $0 \leq \theta \leq 30^\circ$. In particular, zigzag and armchair nanotubes correspond to $\theta = 0^\circ$ and $\theta = 30^\circ$. These and other parameters of carbon nanotubes are summarized in table 1.1.

1.2.3 Electronic, Mechanical and Chemical properties

In 1992, three independent groups reported, almost simultaneously, the possibility that carbon nanotubes could be metallic. The first report was that of Mintmire et al. [10], that performed all-electron density functional theory (DFT) calculations of a (5,5) carbon nanotube. From the band structure, the authors found that a (5,5) nanotube had two bands crossing at the Fermi energy, at $k \approx 2\pi/3$. These authors

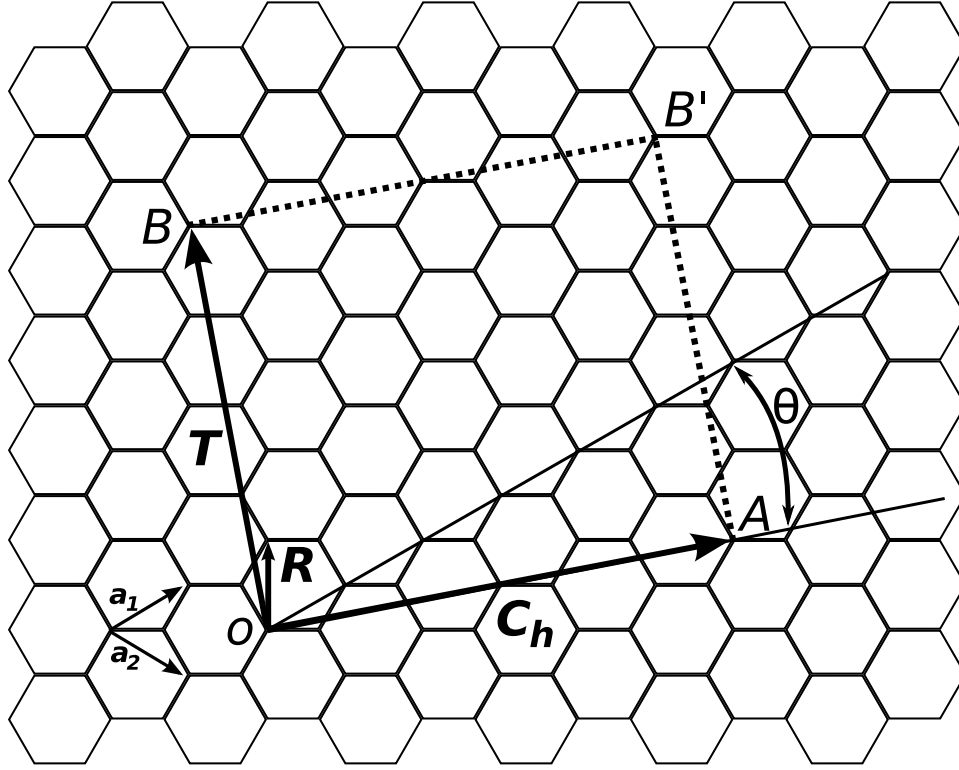


Figure 1.8: Schematic of the construction of a single walled nanotube out from a graphene sheet, indicating its main geometrical descriptors. The nanotube is obtained by wrapping the section of graphene sheet indicated by $OABB'$, and making coincide equivalent points O, A and B, B' . The vector \mathbf{C}_h is the chirality vector, while \mathbf{T} is the translational vector to create the 1D structure. Adapted from [9].

Table 1.1: Parameters for Carbon Nanotubes.

Symbol	Name	Formula	Notes
a	Length of unit vector	$a = \sqrt{3}a_{C-C}$	$a_{C-C} = 1.42\text{\AA}$
\mathbf{C}_h	Chiral vector	$\mathbf{C}_h = n\mathbf{a}_1 + m\mathbf{a}_2 \equiv (n, m)$	$0 \leq m \leq n$
L	Length of chiral vector	$L = \mathbf{C}_h = a\sqrt{n^2 + nm + m^2}$	
d_t	Nanotube diameter	$d_t = L/\pi$	
θ	Chiral angle	$\cos \theta = \frac{2n+m}{2\sqrt{n^2+nm+m^2}}$	$0 \leq \theta \leq \pi/6$
d	$\text{gcd}(n, m)^\dagger$		
d_R	$\text{gcd}(2n+m, 2m+n)^\dagger$	$d_R = 3d$ if $3d \mid (n-m)$, $d_R = d$ otherwise	
\mathbf{T}	Translational vector	$\mathbf{T} = t_1\mathbf{a}_1 + t_2\mathbf{a}_2$ $t_1 = \frac{2m+n}{d_R}, t_2 = -\frac{2n+m}{d_R}$	$\text{gcd}(t_1, t_2) = 1$
T	Length of \mathbf{T} and 1D unit cell	$T = \mathbf{T} = \sqrt{3}L/d_R$	
N	Number of hexagons in unit cell	$N = 2(n^2 + nm + m^2)/d_R$	

$^\dagger \text{gcd}(n, m)$ is the greatest common divisor of integers n and m .

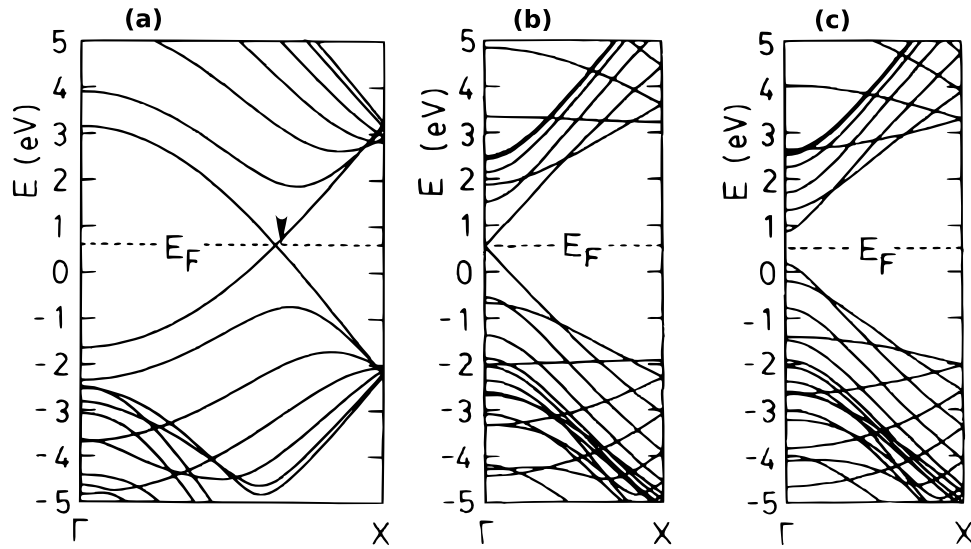


Figure 1.9: Band structures for three different cases of single walled carbon nanotubes. a) Metallic (6,6) nanotube; b) semimetallic (12,0) nanotube; and c) semiconductive (13,0) nanotube.

concluded that the (5,5) nanotube was stable against the Peierls instability.

A month later, a report by Hamada et al. [11] showed the electronic structure of nanotubes using a tight binding approach with $2s$ and $2p$ orbitals as basis, and taking into account the non-orthogonality of the atomic orbitals. By folding and discretizing the graphene Brillouin zone based on the periodic boundary conditions of the nanotube, the authors concluded that in order for a nanotube to be metallic, the K point should lie in one of the 1D Brillouin zones of the nanotube. This was accomplished by all armchair (n, n) nanotubes. Furthermore, nanotubes in which $(n-m)$ is a multiple of 3, have a metallic band structure. The report from Saito et al. [12] reached to the same conclusion by employing also a tight binding model of 1 and 4 orbitals per atom, and sectioning the band structure from graphene according to the 1-D Brillouin zone of the nanotube.

These unusual dependence of the electronic properties on the geometrical structure was not confirmed experimentally until 1998, in which two independent groups led by Cees Dekker and Charles Lieber, performed scanning tunneling spectroscopy (STS) measurements over SWNT atomically resolved by scanning tunneling microscopy (STM) [13, 14].

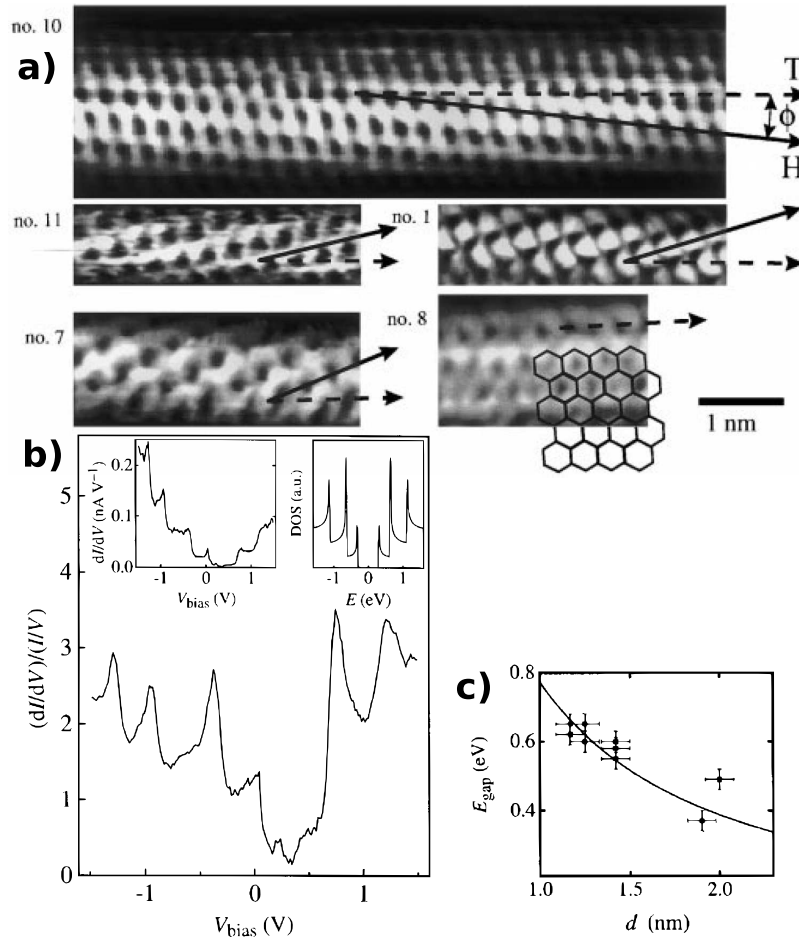


Figure 1.10: a) Atomically resolved STM images of SWNT deposited over Au(111) surface. Dashed lines represent the vector \mathbf{T} , and the vector \mathbf{H} is perpendicular to the armchair direction. The angle ϕ is related to the chiral angle θ by $\theta + \phi = 30^\circ$; b) normalized dI/dV which corresponds to the density of states (DOS) of a semiconductive nanotube. Notice the shift in the Fermi energy, due to hybridization with Au orbitals. c) Energy gaps of different nanotubes, displaying an inverse relation with nanotube diameter, confirming the theoretical prediction of $E_{\text{gap}} = 2\gamma_0 a_{C-C}/d_t$. Adapted from [13].

In Wildöer et al. [13] report, single walled nanotubes were dispersed in 1,2 dichlorobenzene, deposited over an oriented Au(111) substrate, and imaged on a STM operated at 4K. The chirality of the nanotubes was determined by measuring the angle ϕ between the nanotube axis and the nearest armchair edge, which is related to θ by $\theta + \phi = 30^\circ$ (figure 1.10a). With the chiral angle and the nanotube diameter determined by STM observations, the chiral indices (n, m) could be determined, and their calculated electronic properties could be compared to STS

data (figure 1.10b), finding a very good agreement both in the predicted density of states and the presence of the Van Hove singularities. The obtained data also confirmed theoretical work that predicted the energy gap was dependant only on the nanotube diameter, by $E_{gap} = 2\gamma_0 a_{C-C}/d_t$, where γ_0 is the C-C tight binding energy parameter.

The strong carbon-carbon bond in graphite, together with graphene elasticity, are responsible of the notable mechanical properties of carbon nanotubes. Shortly after the publication of the electronic properties of a (5,5) nanotube, Robertson, Brenner, and Mintmire reported the calculations for the energy and axial force constants for all nanotubes with radii of less than 9 Å, using the Tersoff and Tersoff-Brenner potentials [16, 17], as well as the local density functional method developed for carbon nanotubes by Mintmire [10]. The authors found that the strain per carbon atom is reduced to graphene values as the nanotube radio increases, folowing an inverse squared relation. In addition, the authors calculated the tensile strain energy of these nanotubes.

In 1996, Treacy et al. [18] were able to indirectly measure the Young's moduli for several carbon nanotubes, based on the amplitude of their thermal vibrations. The authors observed arc-discharge carbon nanotubes that were supported in a heating holder on a 100kV TEM. At room temperature, it was noticed that it was not possible to focus the tips of long carbon nanotubes, however, their bases were easily focused. After running a series of defocus steps, the authors concluded that the blurring was not due to inclination of the nanotubes, and after increasing the temperature to 600K, the blurring in the tips was significantly increased (figure 1.11a,b), indicating a thermal origin of the nanotube tip vibrations. By measuring the amplitude of the tip vibrations versus the temperature, the authors were able to relate it to the Young moduli of the fibers, assuming these were homogeneous cylindrical cantilevers.

The bending and buckling resistance of carbon nanotubes was studied by Falvo et al. [19], using an atomic force microscope (AFM) tip to manipulate and apply lateral stresses to nanotubes deposited over a mica substrate by solvent evaporation. Nanotubes were subject to a series of distinct manipulations bending and straight-

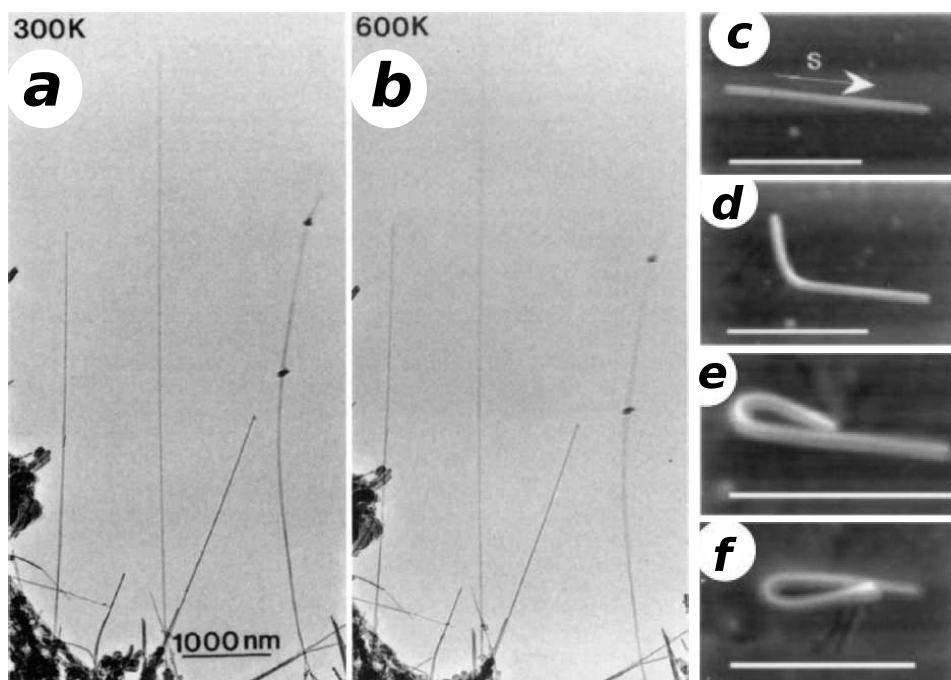


Figure 1.11: a,b) TEM images show the effect of the thermal vibrations in MWCNTs, notice the increased blurring in nanotubes after the temperature was increased from 300K to 600K. Treacy et al. relate this vibrations to the Young modulus of nanotubes; and c-f) AFM images of a MWNT subject to lateral stress by the AFM tip. The nanotube is bent in two opposite directions, without suffering major structural damage. Adapted from [18] (a,b) and [19] (c-f).

ening the tube (see figure 1.11c-f). It was observed that nanotubes bent using a combination of two deformation modes: the Brazier effect causes the change of the cross section from circular to oval over the curved nanotube, while bifurcation leads to a low amplitude rippling of the surface on the inside of the bend. The authors found that nanotubes can be subject to a large deformation stress without having permanent damage.

1.3 Carbon Nanotube synthesis methods

Carbon nanotubes can be synthesized by different methods, most of which involve the vaporization or decomposition of carbon species under out-of-equilibrium conditions. The presence of transition-metal catalytic particles often helps to increase

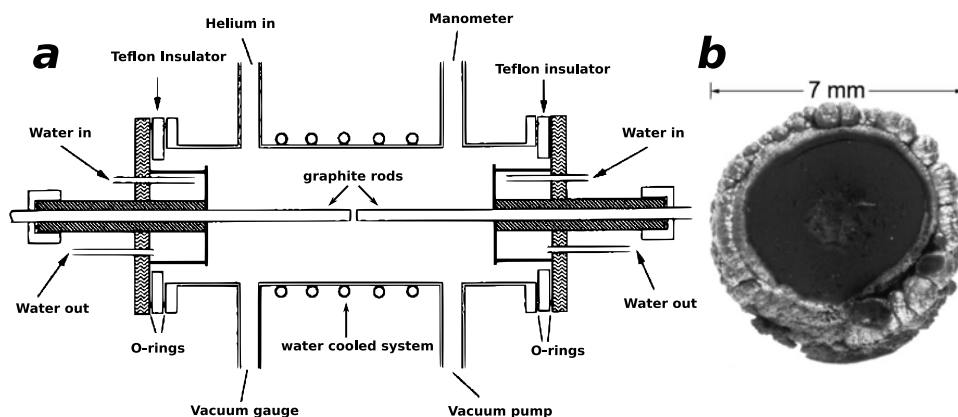


Figure 1.12: a) Schematic of the arc-discharge device employed for carbon nanotube production; and b) cross-section image of a typical cathode carbonaceous deposit. Adapted from [20].

the yield of the produced material.

1.3.1 Electric arc-discharge

The arc-discharge device used for MWCNT synthesis is based upon the fullerene reactor from Kratschmer et al. [4]. The optimal conditions involve a high direct current (80–100 A) passed through two high purity graphite rods (6–10 mm O.D.) with a controlled separation of 1–2 mm, under a helium atmosphere (≈ 500 torr). A schematic drawing is depicted in figure 1.12a. During arcing, the anode is consumed, and a deposit forms in the cathode at a rate of 1 mm/min. The core of the deposit (see figure 1.12b) contains carbon nanotubes and nested polyhedral graphite particles, while the gray outshell is mainly graphite and graphene layers.

The arc discharge method has also been used to produce SWNTs [7, 8]. In this case, a transition metal catalyst is also needed. SWNTs have been synthesized with different metal catalyst compositions, with Fe, Ni, Co being the most common. A mixture of Ni-Y used by Journet et al. [21] resulted in very high yields of SWNTs (70–90 %), allowing large-scale synthesis of SWNTs by the arc-discharge method.

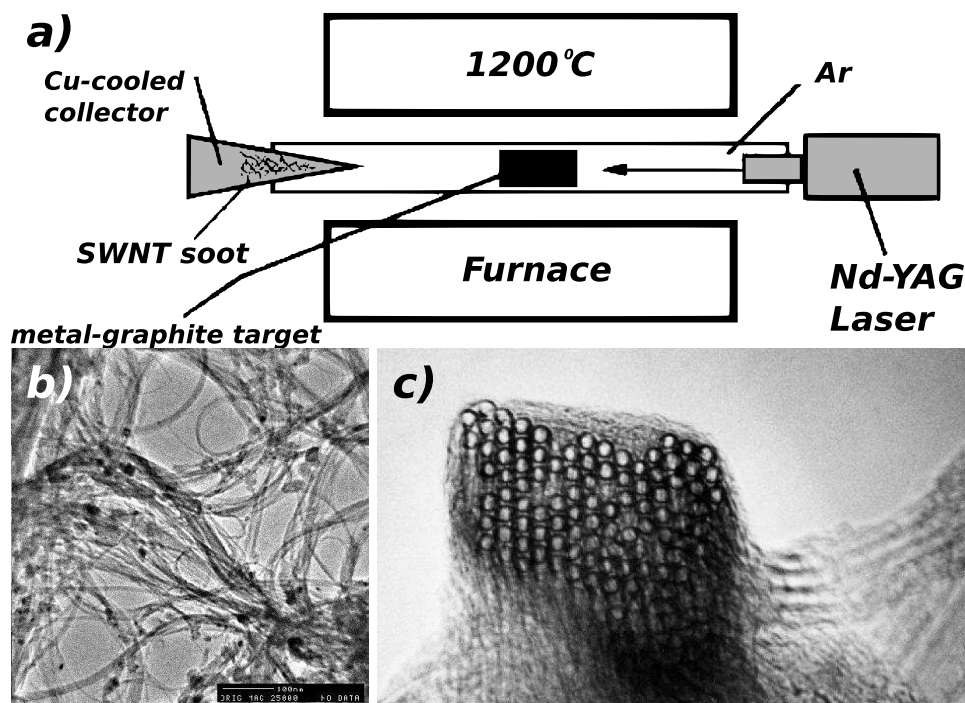


Figure 1.13: a) Schematic of the laser vaporization device employed for carbon nanotube production; b) SEM images of SWNT bundles synthesized by the laser method; and c) HRTEM image of the cross-section of a SWNTs hexagonal packed rope, with nanotubes of similar diameter. Adapted from [20].

1.3.2 Laser Ablation of graphite

The vaporization of high purity graphite by a high power laser (YAG type) inside a furnace at 1200°C under an inert atmosphere has been used for nanotube synthesis by Guo et al. [22] (figure 1.13a). The nanotube growth had been explained before arguing that the high electric field in the arc-discharge device would prevent a fullerene hemisphere or a growing nanotube from closing. In the case of laser ablation, there was no electric field to explain the growth. It was noticed that both MWNT and nested fullerenes were produced, but no SWNT were found in the sample. The proposed growth mechanism involved the stabilization of the open edges of a growing nanotube by interlayer or lip-lip interactions that prevent the structure from closing and allow the incorporation of incoming carbon species into the nanotube. Other experiments used a Nd-YAG laser targeted at powdered graphite under Ar atmosphere, contained inside a quartz tube to produce MWNTs [23].

The production of SWNTs by laser ablation requires the addition of metal catalyst to the graphite targets. In this context, Thess et al. [24] were the first to report the successful synthesis of SWNT by laser ablation of a Carbon-Nickel-Cobalt target at 1200 °C. The obtained nanotubes had a very narrow diameter distribution, and were arranged into bundles with hexagonal packing (see figure 1.13b).

1.3.3 Electrolysis

This method was developed by Hsu et al. [25] in 1995. A graphite crucible filled with lithium chloride (LiCl) is heated to 600°C, which is above the melting point of the salt, inside a furnace under an Ar atmosphere. A graphite rod (cathode) is immersed into the molten salts, and a direct current is then applied (see figure 1.14). After cooling to room temperature, the salts are removed from the crucible by dissolving them with distilled water. The carbonaceous material mixed in the salts is suspended in the solution. The aqueous suspension is mixed with a similar volume of toluene, which dissolves carbon materials, and then separated by decantation. After evaporation, a carbonaceous deposit is obtained.

The optimum conditions for nanotube growth (20–30 %) were low currents (3–7 A) and shallow electrode immersions (3–7 mm). The carbonaceous product also contains amorphous carbon (30–40 %), encapsulated metal particles (2–30 %), and some onion-like carbon structures (figure 1.14b). The obtained nanotubes are similar to those made by condensation processes like arc-discharge or laser ablation (figure 1.14c). The only downside is that SWNT have not been produced yet with this method.

1.3.4 Hydrocarbon Pyrolysis

Thermal decomposition of hydrocarbons in presence of metal catalysts is one of the most versatile methods for production of carbon nanostructures. Also known as chemical vapor deposition (CVD), its growth process involves the diffusion of carbon species on metal catalysts, depicted in figure 1.15 with three main growth mechanisms:

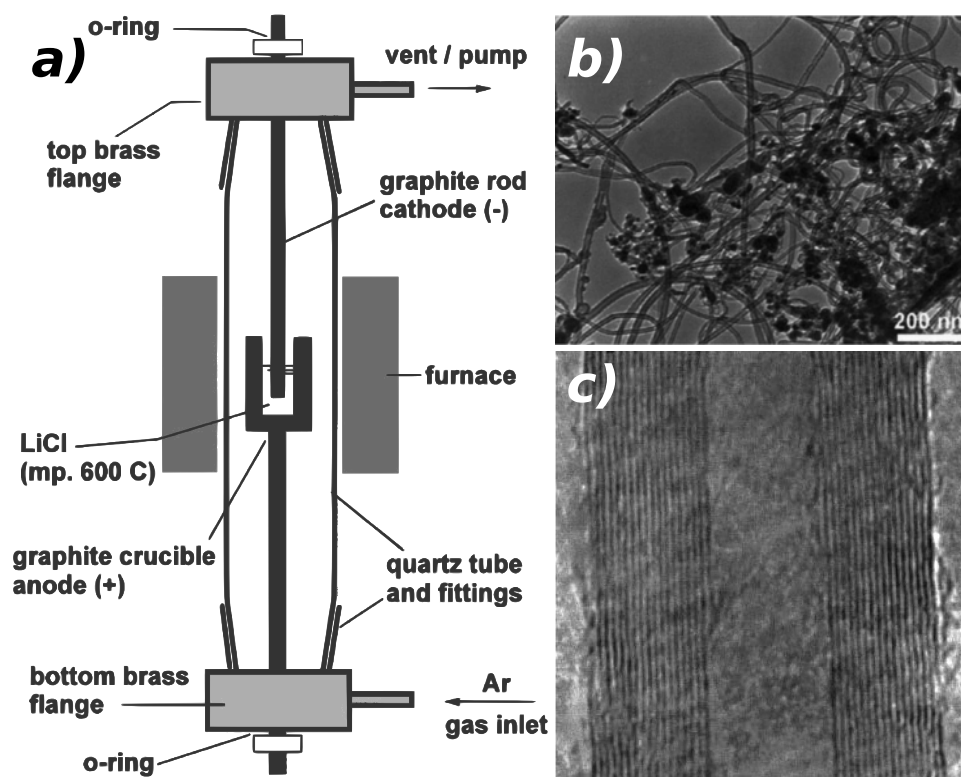


Figure 1.14: a) Schematic of the electrolysis device used for production of carbon nanotubes. b) TEM image of the entanglement of carbon nanotubes. Encapsulated metal particles and amorphous carbon are also present. c) High resolution image of a nanotube synthesized by this method. Adapted from [20].

- a) *Top carbon diffusion through catalytic particles.* Proposed by Baker et al. [26] when studying the decomposition of acetylene over metal catalysts. The carbon fragments diffuse through the metal catalyst and precipitate at the colder end of the particle, allowing the filament to grow.
- b) *Top carbon diffusion on catalytic particles.* Proposed by Baird et al. [27] and Oberlin et al. [1], stating that carbon filaments grow by the precipitation of carbon that diffused over the catalyst surface.
- c) *Bottom carbon diffusion through catalytic particles.* Filament growth occurs due to the rapid movement of carbon species through the metal catalyst, thus segregating a filament. In this model, the catalyst remains attached to the substrate, and filaments grow from their bases rather than their tips.

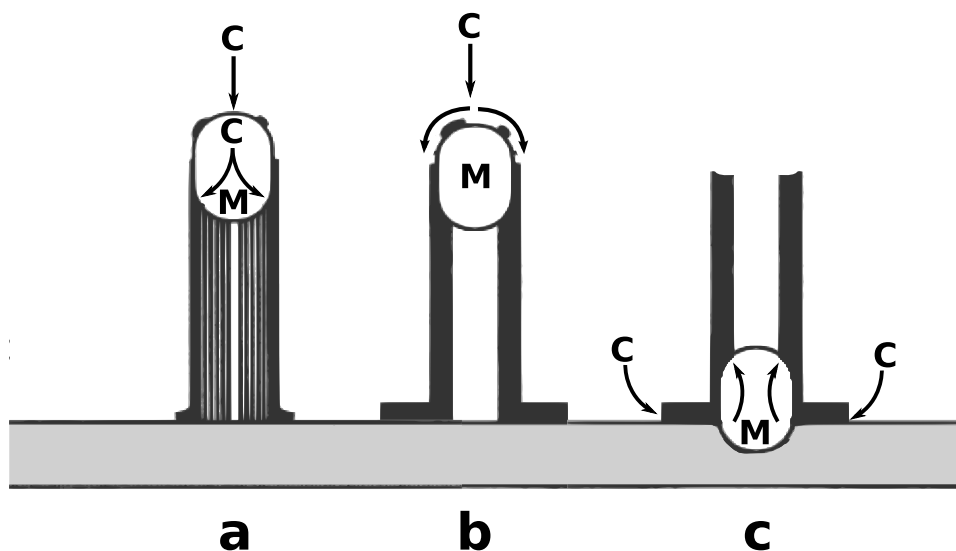


Figure 1.15: Different growth models of carbon fibers proposed for the CVD method

This method was employed by Oberlin et al. when they first observed carbon nanotubes in the center of carbon fibers [1]. In most of the cases, the experimental setup involves the thermolysis of hydrocarbons (gaseous, liquid or solids) at high temperatures under a controlled inert atmosphere, and its deposition on metal catalyst that could be formed in situ (using organometallic compounds mixed with the hydrocarbon) or previously deposited on substrates. It is possible to produce SWNTs using this method. Dai et al. [28] reported the generation of SWNTs via thermolytic CO disproportionation at 1200° using Molybdenum particles as catalyst. This results confirmed the early experiments of Oberlin et al. [1], where SWNTs were produced using benzene / ferrocene mixtures.

1.4 Doping of carbon nanotubes

Shortly after the finding that carbon nanotubes could be either metallic or semi-conductive [10–12], Yi and Bernholc proposed that nitrogen or boron could be used for doping carbon nanotubes [29]. The authors found that carbon nanotubes could be doped as *n* or *p* type semiconductors depending whether nitrogen or boron was used as dopant.

By 1994, Miyamoto et al. [30] proposed that hexagonal BC₂N layers could be

rolled to form nanotubes. This compound has two isomeric forms, which confer different electronic properties to the nanotubes based on them. The authors found that type-II layer caused semiconducting nanotubes for a (2,2) arrangement, and that n or p type semiconductive nanotubes could be obtained by substituting N or B atoms with C. The authors also proposed the formation of tubes from hexagonal BC_3 [31], finding that these nanotubes should be stable.

Doped multiwalled carbon nanotubes were first synthesized by Stephan et al. [32] in 1994 using a Krätschmere-Huffman electric arc-discharge device [4], where the anode was filled with a mixture of elemental boron and graphite powder in a 1:2 weight ratio, and the reaction was carried out under a nitrogen atmosphere (≈ 200 mbar) at 25 V and 100 A. The sample consisted of thin graphitic sheets (5–100 nm); mixed with thick tubes of 100–500 nm diameter with low B and N concentration (less than 2%); and with thinner nanotubes of 50–100 nm diameter with B and N content typically ranging from 0–10%. EELS spectra from nanotubes and graphitic sheets confirmed the presence of the three elements simultaneously. In the next years, other groups succeeded in doping of nanotubes following this method [33, 34],

In 1997, Zhang et al. [35] were able to produce BCN nanotubes by laser ablation of a composite BN-graphite target inside a furnace at 1000–1200°C, under nitrogen atmosphere and using metal catalysts. Later that year, Terrones et al. [36] reported the synthesis of aligned nanotube bundles grown over laser-etched cobalt films heated at 950°C, by the decomposition of 2-amino-4,6-dichloro-s-triazine. In subsequent publications, the authors reported the production of CN_x nanotubes by pyrolysis of ferrocene/melamine mixtures [37, 38], and ferrocene under NH_3 atmosphere [39].

References

- [1] A. Oberlin, M. Endo, and T. Koyama. Filamentous growth of carbon through benzene decomposition. *Journal of Crystal Growth*, 32:335–339, 1976.
- [2] L.V. Radushkevich and V.M. Lukyanovich. O strukture ugleroda, obrazujucesja pri termiceskom razlozenii okisi ugleroda na zeleznom kontakte. *Zurn. Fisic. Chim.*, 26:88–95, 1952.
- [3] H. W. Kroto, J. R. Heath, S. C. O'Brien, R. F. Curl, and R. E. Smalley. C₆₀: Buckminsterfullerene. *Nature*, 318:162–163, November 1985.
- [4] W. Kratschmer, L.D. Lamb, K. Fostiropoulos, and D.R. Huffman. Solid C₆₀: a new form of carbon. *Nature*, 347:354–358, 1990.
- [5] S. Iijima. Helical microtubules of graphitic carbon. *Nature*, 354:56–58, 1991.
- [6] T.W. Ebbesen and P.M. Ajayan. Large-scale synthesis of carbon nanotubes. *Nature*, 358:220–222, 1992.
- [7] S. Iijima and T. Ichihashi. Single-shell carbon nanotubes of 1-nm diameter. *Nature*, 363:603–605, 1993.
- [8] D.S. Bethune, C.H. Klang, M.S. de Vries, G. Gorman, R. Savoy, J. Vazquez, and R. Beyers. Cobalt-catalysed growth of carbon nanotubes with single-atomic-layer walls. *Nature*, 363:605–607, 1993.
- [9] R. Saito, G. Dresselhaus, and M.S. Dresselhaus. *Physical properties of carbon nanotubes*. Imperial College Press, 1998.
- [10] J. W. Mintmire, B. I. Dunlap, and C. T. White. Are fullerene tubules metallic? *Physical Review Letters*, 68:631–634, 1992.
- [11] N. Hamada, S. Sawada, and A. Oshiyama. New one-dimensional conductors: Graphitic microtubules. *Physical Review Letters*, 68(10):1579–1581, March 1992.

- [12] R. Saito, M. Fujita, G. Dresselhaus, and M. S. Dresselhaus. Electronic structure of graphene tubules based on c60. *Physical Review B*, 46:1804–1811, July 1992.
- [13] J.W.G. Wildöer, L.C. Venema, A.G. Rinzler, R.E. Smalley, and C. Dekker. Electronic structure of atomically resolved carbon nanotubes. *Nature*, 391:59–62, 1998.
- [14] T.W. Odom, J.-L. Huang, P. Kim, and C.M. Lieber. Atomic structure and electronic properties of single-walled carbon nanotubes. *Nature*, 391:62–64, 1998.
- [15] D.H. Robertson, D.W. Brenner, and J.W. Mintmire. Energetics of nanoscale graphitic tubules. *Physical Review B*, 45:12592–12595, 1992.
- [16] J. Tersoff. Empirical interatomic potential for carbon, with applications to amorphous carbon. *Physical Review Letters*, 61:2879–2882, 1988.
- [17] Donald W. Brenner. Empirical potential for hydrocarbons for use in simulating the chemical vapor deposition of diamond films. *Physical Review B*, 42:9458–9471, 1990.
- [18] M.M.J. Treacy, T.W. Ebbesen, and J.M. Gibson. Exceptionally high young’s modulus observed for individual carbon nanotubes. *Nature*, 381:678–680, 1996.
- [19] M.R. Falvo, G.J. Clary, R.M. Taylor, V. Chi, F.P. Brooks, S. Washburn, and R. Superfine. Bending and buckling of carbon nanotubes under large strain. *Nature*, 389:582–584, 1997.
- [20] M. Terrones. Science and technology of the twenty-first century: Synthesis, properties, and applications of carbon nanotubes. *Annual Review of Materials Research*, 33:419–501, 2003.
- [21] C. Journet, W.K. Maser, P. Bernier, A. Loiseau, M.L. de la Chapelle, S. Lefrant, P. Deniard, R. Lee, and J.E. Fischer. Large-scale production of single-walled carbon nanotubes by the electric-arc technique. *Nature*, 388:756–758, 1997.

- [22] T. Guo, P. Nikolaev, A.G. Rinzler, D. Tomanek, D.T. Colbert, and R.E. Smalley. Self-assembly of tubular fullerenes. *Journal of Physical Chemistry*, 99: 10694–10697, 1995.
- [23] M. Terrones. *Production and characterization of novel fullerene-related materials: nanotubes, nanofibers and giant fullerenes*. PhD thesis, University of Sussex, 1997.
- [24] A. Thess, R. Lee, P. Nikolaev, H. Dai, P. Petit, J. Robert, C. Xu, Y.H. Lee, S.G. Kim, A.G. Rinzler, D.T. Colbert, G.E. Scuseria, D. Tomanek, J.E. Fischer, and R.E. Smalley. Crystalline Ropes of Metallic Carbon Nanotubes. *Science*, 273: 483–487, 1996.
- [25] W.K. Hsu, J.P. Hare, M. Terrones, H.W. Kroto, D.R.M. Walton, and P.J.F. Harris. Condensed-phase nanotubes. *Nature*, 377:687–687, 1995.
- [26] R.T.K. Baker, M.A. Barber, P.S. Harris, F.S. Feates, and R.J. Waite. Nucleation and growth of carbon deposits from the nickel catalyzed decomposition of acetylene. *Journal of Catalysis*, 26:51–62, 1972.
- [27] T. Baird, J.R. Fryer, and B. Grant. Carbon formation on iron and nickel foils by hydrocarbon pyrolysis reactions at 700°C. *Carbon*, 12:591–602, 1974.
- [28] Hongjie Dai, Andrew G. Rinzler, Pasha Nikolaev, Andreas Thess, Daniel T. Colbert, and Richard E. Smalley. Single-wall nanotubes produced by metal-catalyzed disproportionation of carbon monoxide. *Chemical Physics Letters*, 260:471–475, 1996.
- [29] J.-Y. Yi and J. Bernholc. Atomic structure and doping of microtubules. *Physical Review B*, 47:1708–1711, 1993.
- [30] Yoshiyuki Miyamoto, Angel Rubio, Marvin L. Cohen, and Steven G. Louie. Chiral tubules of hexagonal bc_2n . *Physical Review B*, 50:4976–4979, 1994.
- [31] Yoshiyuki Miyamoto, Angel Rubio, Steven G. Louie, and Marvin L. Cohen. Electronic properties of tubule forms of hexagonal bc_3 . *Physical Review B*, 50: 18360–18366, 1994.

- [32] O. Stephan, P. M. Ajayan, C. Colliex, Ph. Redlich, J. M. Lambert, P. Bernier, and P. Lefin. Doping Graphitic and Carbon Nanotube Structures with Boron and Nitrogen. *Science*, 266:1683–1685, 1994.
- [33] Z. Weng-Sieh, K. Cherrey, N.G. Chopra, X. Blase, Y. Miyamoto, A. Rubio, M.L. Cohen, S.G. Louie, A. Zettl, and R. Gronsky. Synthesis of $B_xC_yN_z$ nanotubules. *Phys. Rev. B*, 51:11229–11232, 1995.
- [34] Ph. Redlich, J. Loeffler, P.M. Ajayan, J. Bill, F. Aldinger, and M. Rühle. B—c—n nanotubes and boron doping of carbon nanotubes. *Chemical Physics Letters*, 260:465–470, 1996.
- [35] Y. Zhang, H. Gu, K. Suenaga, and S. Iijima. Heterogeneous growth of b—c—n nanotubes by laser ablation. *Chemical Physics Letters*, 279:264–269, 1997.
- [36] M. Terrones, N. Grobert, J. Olivares, J.P. Zhang, H. Terrones, K. Kordatos, W.K. Hsu, J. P. Hare, P.D. Townsend, K. Prassides, A.K. Cheetham, H.W. Kroto, and D.R.M. Walton. Controlled production of aligned-nanotube bundles. *Nature*, 388:52–55, 1997.
- [37] M. Terrones, P. Redlich, N. Grobert, S. Trasobares, W.-K. Hsu, H. Terrones, Y.-Q. Zhu, J.P. Hare, C.L. Reeves, A.K. Cheetham, M. Rühle, H.W. Kroto, and D.R.M. Walton. Carbon nitride nanocomposites: Formation of aligned C_xN_y nanofibers. *Advanced Materials*, 11:655–658, 1999.
- [38] M. Terrones, H. Terrones, N. Grobert, W. K. Hsu, Y. Q. Zhu, J. P. Hare, H. W. Kroto, D. R. M. Walton, Ph. Kohler-Redlich, M. Rühle, J. P. Zhang, and A. K. Cheetham. Efficient route to large arrays of CN_x nanofibers by pyrolysis of ferrocene/melamine mixtures. *Applied Physics Letters*, 75:3932–3934, 1999.
- [39] W.-Q. Han, P. Kohler-Redlich, T. Seeger, F. Ernst, M. Rühle, N. Grobert, W.-K. Hsu, B.-H. Chang, Y.-Q. Zhu, H.W. Kroto, D.R.M. Walton, M. Terrones, and H. Terrones. Aligned CN_x nanotubes by pyrolysis of ferrocene/ C_{60} under NH_3 atmosphere. *Applied Physics Letters*, 77:1807–1809, 2000.

Chapter 2

Synthesis and Characterization of Phosphorus-Nitrogen Doped Multiwalled Carbon Nanotubes

In this chapter, the synthesis of multiwalled carbon nanotube (MWNT) arrays using solutions of ferrocene and triphenyl-phosphine in benzylamine in conjunction with an aerosol pyrolysis experiment is presented. During MWNT growth, iron phosphide (Fe_3P) nanoparticles act as a catalyst, thus leading to the formation of PN-doped multiwalled carbon nanotubes. The samples produced were carefully examined by SEM, HRTEM and STEM, as well as high resolution elemental analyses using EELS and EDX spectroscopy.

2.1 Importance of doping in carbon nanotubes

Curvature changes the chemically inert graphite surface and makes it easier to incorporate atoms on the tube surface. In this context, nitrogen, which is known to have low levels of doping in bulk graphite [1], can be easily incorporated in carbon nanotubes by substitution. Inclusion of non-carbon atoms into the hexagonal network of carbon nanotubes is known to modify the electronic and chemical properties due to variations in their electronic structure.

Nitrogen, for example, acts as an electron donor in a carbon nanotube since it has

5 electrons in the valence shell, causing a shift in the Fermi level to the valence bands, and hence making all nitrogen doped tubes metallic, regardless of their geometry [2]. Nitrogen can also be incorporated within nanotubes in a pyridine-like coordination. It is noteworthy that the doped sites within carbon nanotubes significantly modify their chemical reactivity, thereby broadening the spectrum of possible applications [2].

Although proposed since 1993 by Yi and Bernholc [3], the first doped CNTs were successfully synthesized by 1994 in 1994, by the arc-discharge technique using boron-graphite electrodes under nitrogen atmosphere [4]. Years later, doped CNTs were reported by the laser ablation of graphite-BN targets under nitrogen atmosphere [5].

In 1997, nitrogen doped CNTs were obtained by the thermal decomposition of N-containing hydrocarbons over metal particles [6, 7], the most common technique to produce them upto date. It was until 2004 that single walled CNTs (SWNTs) were doped by nitrogen with the arc discharge technique [8]. The next couple of years N-doped SWNTs were obtained by thermal decomposition of xylene-acetonitrile mixtures or ethanol-benylamine solutions using Fe as catalyst respectively [9, 10].

2.2 Phosphorus as an impurity in carbon systems

Phosphorus has been used as an impurity in carbon systems due to their similar valence electronic structure (phosphorus has one more electron than carbon in the valence shell), being limited only by the difference in the ion size.

2.2.1 Phosphorus and diamond-like thin films

In the case of synthetic diamond thin films, the most popular synthesis method has been plasma-assisted chemical vapor deposition (CVD) of hydrocarbons over either oriented silicon surfaces or crystalline diamond particles used as seeds for growth. Boron impurities were readily observed to behave as acceptors, hence turning diamond into a *p*-type semiconductor [11]. Then, the synthesis of *n*-type semiconducting diamond was highly desirable in order to create bipolar semiconducting devices like *pn* junctions, in which the wide band-gap (5.47eV) makes diamond a perfect

candidate for ultraviolet emitting optoelectronic devices.

In 1990, Okano et al. [12] successfully synthesized phosphorus-doped polycrystalline diamond thin films using a microwave plasma-enhanced chemical vapor deposition device (MWPE-CVD) using diphosphorus pentoxide (P_2O_5) as a doping source, in a solution of methanol and acetone as carbon feedstock. The deposition took place over a $\{100\}$ *n*-type silicon surface at 850 °C using H_2 as carrier. By Hall effect measurements, it was determined that the doped film was an *n*-type semiconductor with a resistivity of 100Ωcm. The Raman spectra showed a sharp peak at 1332cm^{-1} , indicating good crystallinity, but also a wide feature located at 1550cm^{-1} indicated a high amount of defective sp^2 hybridized carbons due to pressure of the grain boundaries.

It was also reported by Akaishi et al. [13] that phosphorus could be used as catalyst for diamond synthesis in high pressure–high temperature (HPHT) reactions. The authors used red phosphorus to transform graphite into diamond in a HPHT experiment at 7.7GPa and 2200 °C for 10 min. Unfortunately, the obtained crystals were not large enough to verify their electrical properties.

The real breakthrough came in 1997 when Koizumi et al. [14] successfully synthesized homoepitaxial phosphorus-doped diamond thin films using a polished $\{111\}$ HP-HT diamond surface as substrate in a MWPE-CVD experiment. The carrier gas was H_2 , while the carbon feedstock was methane (CH_4), and phosphine (PH_3) was used as doping source. The synthesis temperature was 950 °C and the growth time was 2 h. Crystallinity was evaluated by Raman spectroscopy and reflection high-energy electron diffraction (RHEED). It was observed that the crystalline order was diminished by increasing the $(PH_3)/(CH_4)$ ratio, as well as by lowering the reaction temperature or by increasing the overall methane concentration. The temperature dependence of the conductivity and negative Hall voltage measurements using a 0.5T magnetic field confirmed that the produced film was indeed an *n*-type semiconductor.

Phosphorus-doped diamond thin films obtained by this method have been used to fabricate optoelectronic devices [15–17]. Ultraviolet emission in diamond *pn* junctions was reported by Koizumi et al. [15] using a boron-doped diamond film as

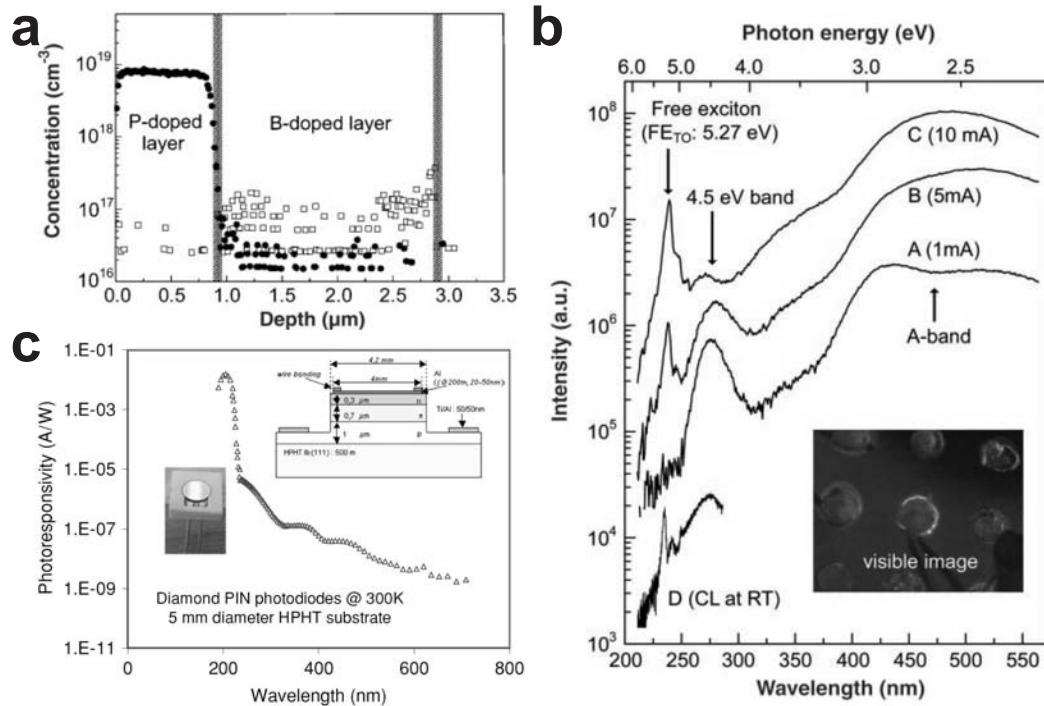


Figure 2.1: Plots showing the performance of P-doped diamond thin films obtained by Epitaxial deposition over $\{1\ 1\ 1\}$ diamond surfaces. a) Doping profile showing the B-doped and P-doped interface, b) Emission Spectra of a pn -junction. c) Photoresistive device using a pin -junction and its response spectrum to solar light. Adapted from Koizumi et al. [15](a,b) and Nesladek [16](c).

substrate and depositing a P-doped thin film on top. The resulting device had a very distinctive I-V curve, similar to that of a rectifying diode. For currents above 5mA, a sharp emission peak of 235nm (5.27eV) was detected. Schottky barrier diodes have been fabricated by Suzuki et al. [17] by depositing Au/Ni contacts over a 1.5μm thick homoepitaxial P-doped diamond thin film. In addition, Nesladek [16] have developed photodiodes with a high activity in the ultraviolet region and a low response in the visible light region.

2.2.2 Phosphorus and vapor-grown carbon fibers

Although phosphorus-doped diamond films are a very attractive subject of research, the literature is scarce when it comes to the use of phosphorus in vapor-grown carbon fibers (VGCFs). The most relevant work is from Seiji Motojima's group

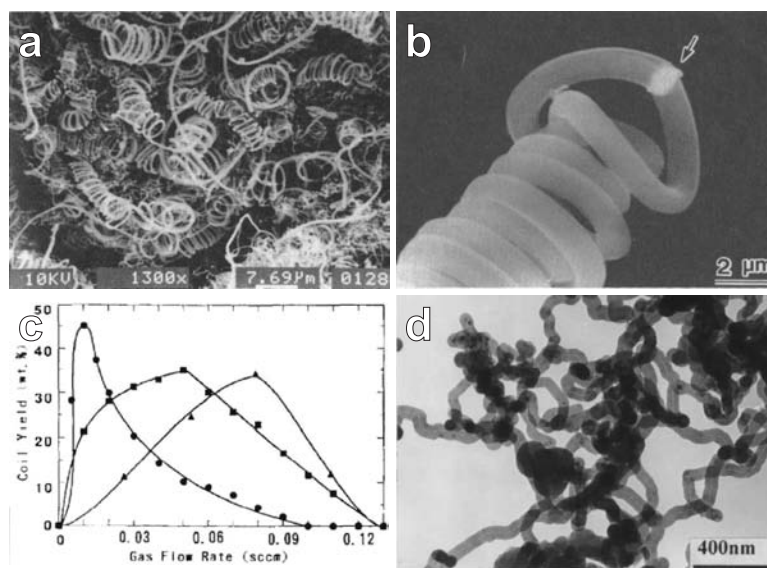


Figure 2.2: a), b) Morphology of the helical carbon fibers obtained using Phosphorus as impurity for Nickel catalytic particles; c) coiled fibers yield response to variations in the impurity sources and flow rates, and d) TEM image showing nano-fibers obtained by pyrolysis of benzene, ferrocene and triphenylphosphine. Adapted from Motojima et al. [18] (a,b,c) and Ci et al. [20] (d).

in Japan, regarding the use of phosphorus to catalyze the growth of helical carbon fibers [18, 19].

In 1993, Motojima et al. [18] found that helical carbon fibers could be synthesized by pyrolysis of acetylene over a graphite substrate using nickel powders as catalyst, and phosphorus trichloride (PCl_3) as source of phosphorus impurities. The authors found that the optimum temperature range for the synthesis of the fibers was a very narrow window around 650 °C. It was also noticed that the amount of the impurity played a key role, since no coiled fibers were obtained when PCl_3 was not present, but neither when it was added in excess. It was found that the content of phosphorus in the metal particles was about 3.1 at%. The authors also tried to synthesize carbon fibers from Ni_2P metal particles, but they were not successful.

Subsequently, in 1999, Ci et al. [20] used phosphorus as a promoter of carbon fiber growth, using a floating catalyst method. In this experiment, benzene (C_6H_6) was used as a carbon feedstock, while ferrocene ($\text{Fe}(\text{C}_5\text{H}_5)_2$) and triphenyl phosphine ($\text{P}(\text{C}_6\text{H}_5)_3$, TPP) were used as iron and phosphorus sources; hydrogen was used as

carrier gas. The mentioned fibers were synthesized at a reaction temperature of 1100 – 1200 °C. Optimal growth was obtained using 1.0 g of ferrocene and 0.5 g of TPP per 100ml of benzene. Similarly to Motojima et al. [18], it was observed that an excess of phosphorus beyond the optimum level resulted in the frustration of the carbon fiber growth, and that without any phosphorus addition, the iron particles were coated by graphitic carbon and no fibers were obtained.

More recently, Benissad-Aissani et al. [21] studied the growth of carbon fibers synthesized by the decomposition of methane (CH_4) and hydrogen mixtures using iron catalyst particles obtained from tri-iron dodeca-carbonyl ($\text{Fe}_3(\text{CO})_{12}$) and supported in commercial substrates labeled Papyex® and Grafoil® (A and P). These authors observed that there was no fiber growth on Papyex® supports, while in Grafoil® substrates they observed long and dense fibers up to 6cm long, By studying the impurities present in the substrates, Benissad-Aissani et al. found that the presence of phosphorus was promoting the growth on the Grafoil®-P substrate, while it was inhibiting fiber growth in Papyex® substrate. In order to verify their conclusions, the authors impregnated Grafoil®-A substrates (which had the lower amount of phosphorus impurities) with a solution of phosphoric acid (H_3PO_4) before the growth of the fibers. They found that for a P/Fe atomic ratio below 0.225, phosphorus had a promoting effect, with an optimum ratio of 0.18. It was also found that for very large amounts of phosphorus, the metal particles were mainly Fe_2P , as determined by selected area diffraction studies, and no fibers grew from these particles.

2.2.3 Phosphorus and Carbon Nanotubes

Similar to carbon fibers, the use of phosphorus during nanotube growth has not been widely explored. The first report is that of Wen and Shen [22], where they propose a growth mechanism for coiled carbon nanotubes obtained by pyrolysis of acetylene with phosphorus trichloride (PCl_3) used as an impurity over nickel particles; similar to the works of Motojima on carbon fibers[18, 19]. Later, Ding et al. [23] synthesized carbon nanostructures using Ni– Ni_3P catalytic particles supported on Silicon carbide (SiC) whiskers, and obtained straight and coiled nanotubes, as well as nanoribbon

structures.

The most extensive study of the effect of phosphorus in the growth of carbon nanotubes to date is that of Jourdain et al. [24, 25, 26, 27]. They first reported the growth of repeated units of carbon nanostructures composed by a “head” consisting of a metal particle, and a “tail” formed by a carbon nanotube segment[24]. They proposed a growth mechanism to explain the segmentation of the catalytic particle during the nanotube growth.

After studying the particle chemical composition, Jourdain et al. [25] realized that this particular growth was induced by the presence of phosphorus, which was included as impurity in the anodic alumina substrates used to support the catalyst particles. A systematic study was carried out to understand the roles of the synthesis temperature, catalyst composition, carbon feedstock rate, and the nature of the supporting substrate [26]. The authors found that sequential catalytic growth was observed whenever phosphorus was present, but the yield of nanotubes was higher when nickel/iron particles were used as catalyst at a temperature near 1080 °C. Finally, by means of magnetic force microscopy (MFM) and electron holography, they demonstrated that iron/cobalt phosphide nanoparticles were ferromagnetic at room temperature, thus broadening the range of possible applications for these kind of nanotubes. However, the authors never discussed whether the phosphorus was included in the nanotube hexagonal lattice nor the role of aluminum in the sequential growth observed.

2.3 Synthesis of PN-doped multiwalled Carbon nanotubes by pyrolysis of hydrocarbons

In the present work, the synthesis and characterization of phosphorus-nitrogen doped carbon nanotubes by thermolysis of hydrocarbons and a floating catalyst is presented. The growth of these nanotubes is catalyzed by iron phosphide particles which aggregate while the reaction takes place. The Chemical Vapor Deposition (CVD) technique was selected due to its relative low cost when compared to other synthesis techniques, such as arc discharge or laser ablation.

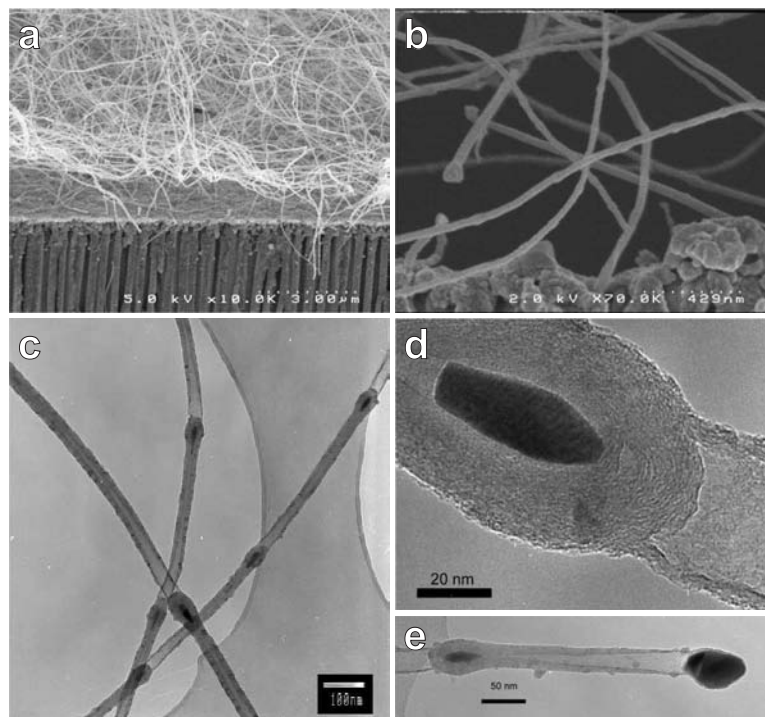


Figure 2.3: (a,b) SEM images of matchstick-like nanotubes grown over anodic alumina substrates using Ni/Fe catalyst. (c,d,e) TEM images of “matchstick-like” carbon nanotubes, where the head-tail structure can be appreciated. Adapted from Jourdain et al. [24].

In this case, an experimental setup was adapted from those used by Reyes-Reyes et al. [28] and Pinault et al. [29], as displayed in figure 2.4. An ultrasonic aerosol generator is filled with a hydrocarbon solution containing the precursor (ferrocene, $\text{Fe}(\text{C}_5\text{H}_5)_2$), the dopant (triphenyl phosphine, TPP, $\text{P}(\text{C}_6\text{H}_5)_3$) and the carbon and nitrogen source (benzylamine, $\text{C}_6\text{H}_5\text{-CH}_2\text{-NH}_2$). This device is activated when an alternate current circulates through a piezoelectric transducer located at the bottom of the vessel, causing the liquid to vibrate. Since the mechanical energy provided by the piezoelectric device could cause an increase in the solution temperature, a water circulator is used to reduce the temperature variation in the vessel. When the vibration frequency is close to the resonant condition, the liquid starts to atomize, thus creating a mist composed of small droplets of the buffer solution. This mist is then carried by an inert gas (Argon) into a quartz tube with an inner diameter of 24mm, whose middle section is located inside a two-furnace heating stage, as

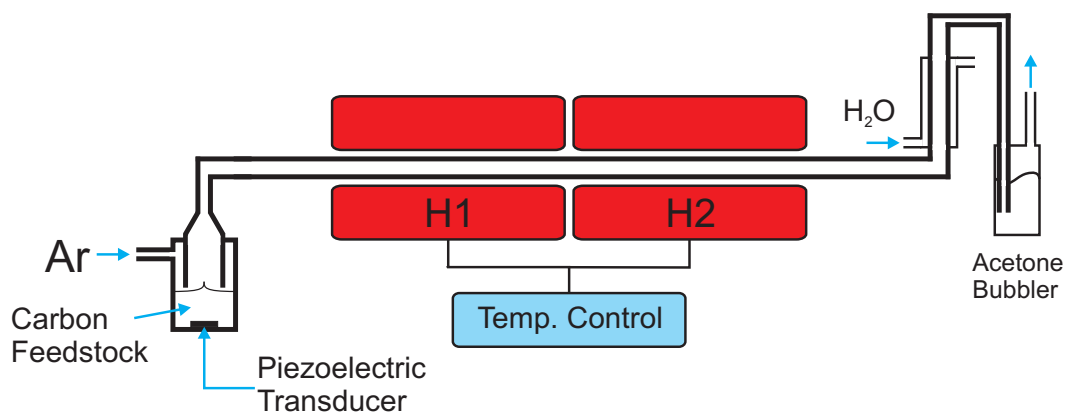


Figure 2.4: Schematic diagram of the pyrolysis setup employed in the synthesis of PN-doped multiwalled carbon nanotubes. Argon is used as carrier gas.

depicted in figure 2.4.

The quartz tube was previously purged of any oxygen traces and the furnaces were heated to the desired synthesis temperature. Since the catalyst particle is formed in the argon inside the quartz tube while the reaction takes place, this method is also referred as the “floating catalyst” method, opposed to the “supported catalyst” method, in which metallic particles are first deposited on a substrate, and then used for carbon nanotube growth. After the gases pass through the furnaces, they are carried into a water cooler to reduce their temperature, and then through an acetone bubbler in order to trap as many hydrocarbon sub-products as possible.

The synthesis time is usually around 20 minutes. After the synthesis takes place, the reactor is allowed to cool down to ambient temperature, while keeping a moderate argon flow (usually 0.3 L/min) to avoid the entrance of oxygen. Carbon nanotubes are grown in the walls of the quartz tube, and are easily scratched off from the tube surface.

In order to find the optimal synthesis conditions, two sets of experiments were performed. In the first one, a solution with 2.5wt% of TPP and 7.5% of ferrocene was pyrolyzed inside a furnace operated at a fixed temperature, ranging from 720°C to 840°C by increments of 40°C, and the Ar flow varied from 0.8 to 1.6 L/min. It was found that the only suitable conditions capable of producing nanotube materials occurred at 760°C and 800°C with an Ar flow of 0.8 L/min. In the second set of experiments, the concentration of the phosphorus dopant (TPP) was varied,

Table 2.1: Synthesis conditions of the samples selected for characterization.

Sample	Temperature	Argon flow	TPP content
A	760°C	0.8 Lt/min	2.5 wt%
B	760°C	0.8 Lt/min	3.3 wt%
C	760°C	0.8 Lt/min	0.0 wt%

using 0.0wt%, 2.5wt%, and 3.3wt%; a fixed concentration of 7.5wt% of ferrocene was dissolved in benzylamine; and the temperature and argon flow were set to the optimal synthesis conditions of 760°C and 0.8 L/min, respectively. In this case, it was observed that the amount of nanotubes collected decreased strongly with the concentration of the phosphorus dopant, almost vanishing when the solution with 3.3wt% of TPP was used. At the end of these experiments, three samples were selected to be further characterized, and their synthesis conditions are summarized in Table 2.1.

2.4 Characterization of PN-doped multiwalled Carbon nanotubes

In order to analyze the samples from different experiments, different microscopy and microanalysis techniques were employed, as well as X-ray powder diffraction and thermogravimetric analysis. For scanning electron microscopy (SEM), samples were analyzed as produced, mounted on standard aluminum pins using carbon tape, and analyzed using a field emission SEM (Phillips FEG-XL30 30kV) equipped with an energy dispersive x-ray (EDX) spectrometer. For thermogravimetric analysis (TGA, ThermoCorp Cahn Versatherm HS, 1.5g/0.1μg) samples were placed on a quartz holder under dry air flow, with a heating rate of 10°C/min from room temperature up to 800°C, and then allowed to cool down to room temperature. To further analyze the bulk sample, X-ray powder diffraction (Bruker Advance D8) was performed on as-produced samples mounted on silicon substrates. For high resolution transmission electron microscopy (JEOL 4000EX HRTEM, operated at 400 kV) and scanning transmission electron microscopy (Philips CM200-FEG equipped

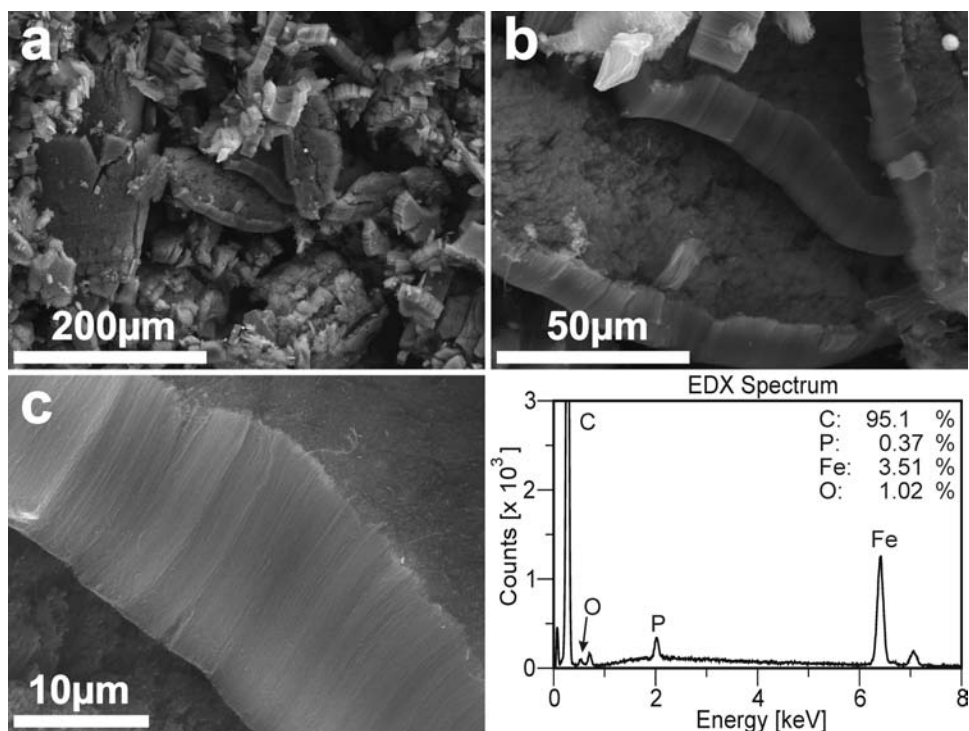


Figure 2.5: Scanning electron microscope (SEM) images of PN-doped multiwalled carbon nanotubes (MWCNTs) from sample A. a) General overview of the sample; b) view of two nanotube mats, where the long range order can be appreciated; c) side view of a nanotube mat, the nanotube length (ca. $18\mu\text{m}$) is considerably shorter when compared to N-doped MWCNT, usually around $70\mu\text{m}$ in length. EDX spectrum of the central region of nanotubes shown in image (c). The Carbon peak was cut off to show the detail, its height is ca. 7000 counts.

with EDX spectrometer, FEI Tecnai F20 with a postcolumn Gatan Imaging Filter, and JEOL 2010 F with a Gatan Enfina energy loss spectrometer, all operated at 200kV), the samples were mounted into copper grids with formvar coating.

The soot collected from the walls of the quartz tube was analyzed by scanning electron microscopy (SEM), as can be seen in figures 2.5 and 2.6. The overview of sample A (see fig. 2.5a) shows mainly multiwalled carbon nanotubes mats, with a low content of amorphous carbon. Further studies confirmed that the sample is notably absent of amorphous carbon (fig. 2.5b), and that the nanotube length is ca. $18\mu\text{m}$ (fig. 2.5c), which is notably lower when compared to N-doped MWCNT whose typical length is in the order of $70\mu\text{m}$. The graph shown in fig. 2.5d depicts the EDX spectrum obtained from the nanotube mat shown in fig. 2.5c, and it can be

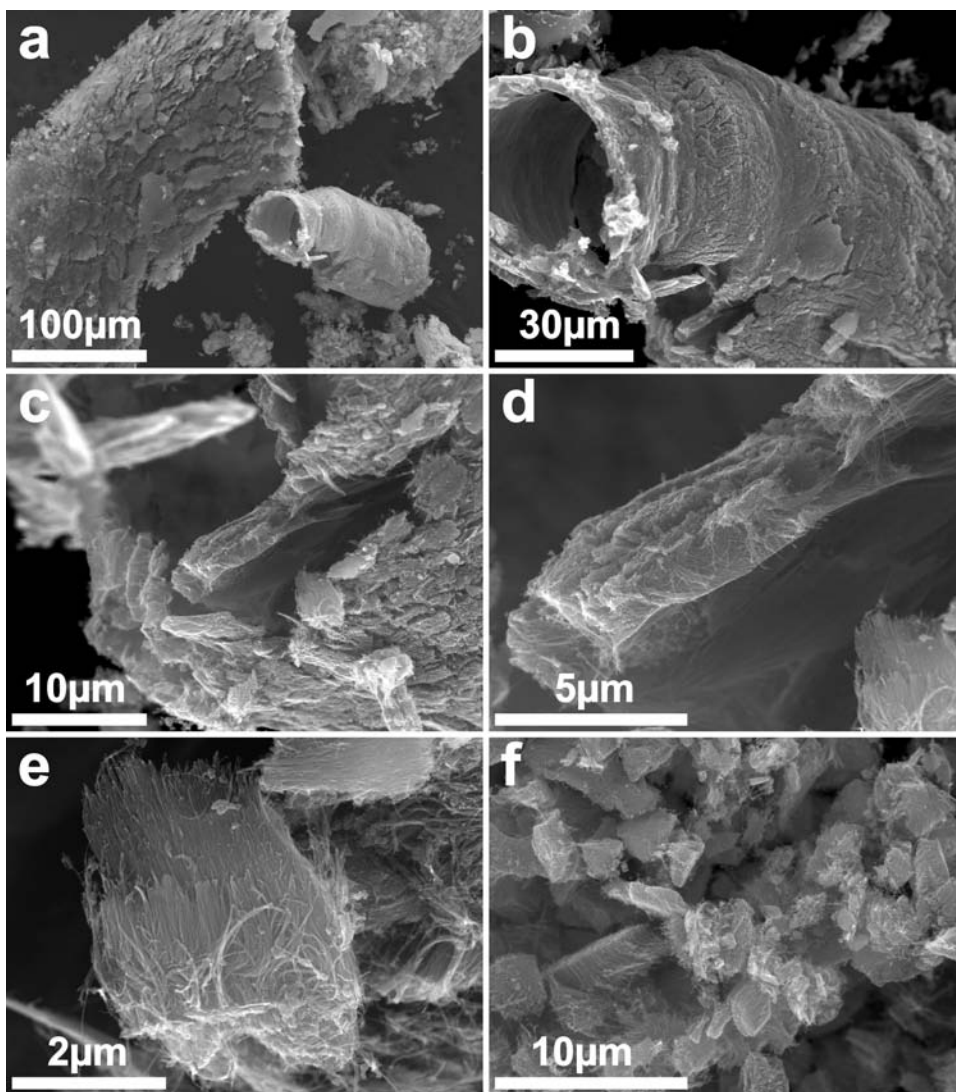


Figure 2.6: SEM images of PN-doped MWCNTs from sample B. a,b) Overview of the sample; c,d) further details of the sample confirm that it is composed of nanotube mats, whose height is only a few micrometer long; e) full detail of a nanotube mat. The nanotube length is only $3.5 \mu m$, and is highly disordered. f) overview of a different zone, confirming that the sample is composed mainly by MWCNT.

clearly seen that a phosphorus peak is present ca. 2 keV. EDX quantification reveals that the phosphorus content is very low (0.37 at%), and it is not clear whether it comes from the nanotubes or from metallic particles embedded in the sample, since iron phosphides are present in the material (see below).

While analyzing sample B, it was thought that the sample was composed of amorphous carbon, since no nanotube mats were evident (figures 2.6a,b). When

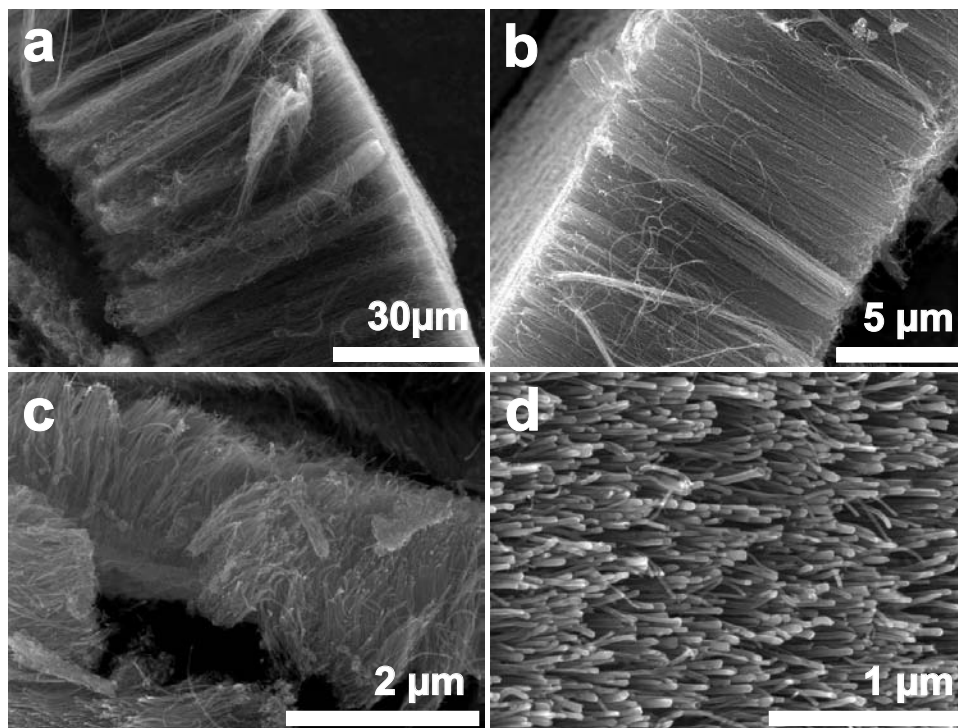


Figure 2.7: Comparison of the length of PN doped MWCNT with different TPP content in the hydrocarbon solution. a) Sample c, 0.0 wt% TPP, ca. $70\mu\text{m}$ long. b) Sample a, 2.5 wt% TPP, ca. $12\mu\text{m}$ long. c) Sample b, 3.3 wt% TPP, ca. $3\mu\text{m}$ long.

increasing the magnification, it was found that the sample was indeed composed of very short carbon nanotube mats, whose length was below $5\mu\text{m}$ and had the appearance of small flakes of amorphous-like carbon. Further detail of these nanotube mats (fig. 2.6e) shows that nanotubes are ca. $3.5\mu\text{m}$ long, and highly disordered. Images from other zones of the sample confirm that the material consists of very short nanotube mats (see fig. 2.6f).

As we increase the phosphorus doping of the nanotubes, their length is reduced from ca. $70\mu\text{m}$ long in the absence of phosphorous (sample c, Fig. 2.7a); to ca. $18\mu\text{m}$ when a 2.5wt% of TPP is added to the spray solution (sample a, Fig. 2.7b); and finally to ca. $3\text{--}4\mu\text{m}$ for the experiment containing 3.3 wt % of TPP (sample b, Fig. 2.7c). This result is consistent with the reduction in the yield of carbonaceous material obtained from the synthesis process when the concentration of TPP was increased from 0.0 wt% to 3.3 wt%.

It was also found that carbon nanotubes grow by a root-growth process, as can be

seen in figure 2.8. Three images from a nanotube mat viewed from the top (fig. 2.8, left column) are compared with images from another nanotube mat viewed from the bottom, or substrate side (fig. 2.8, right column). It can be seen that while on the top side there is a disperse coating of amorphous carbon and very few nanotube tips can be seen, on the bottom side of the nanotube mat there is no amorphous carbon layer, and nanotube tips are evident displaying either a metallic nanoparticle or a hollow tip indicating a missing nanoparticle. This is consistent with the report from Reyes-Reyes et al. [28], where they found a similar feature on N-doped MWCNT, using the same synthesis method.

In order to verify the presence of phosphorus and nitrogen in the whole nanotube mats and also to understand the relation of phosphorus and iron, elemental mappings were obtained by EDX spectroscopy in the SEM. In this case, an extra sample of pristine undoped MWCNT was used as a control sample, while the interest relies on samples A and C. Samples were mounted over standard aluminum SEM pins and maps were taken from regions that were not directly located over the carbon tape in order to have contrast for carbon maps. For each sample, maps for carbon, nitrogen, and phosphorus were taken. Aluminum maps were obtained also as control for the position of the nanotube mat. It can be seen that for the pristine case, only carbon has a clear map, while nitrogen and phosphorus maps are noisy, meaning that these elements are not present. For the N-doped MWCNT maps, nitrogen shows a map that clearly corresponds to the carbon map, while phosphorus remains noisy (i.e. not present). EDX spectrum quantification for N-doped MWCNT shows a nitrogen content of 5.6 at%. Finally, for the PN-doped case, a weak nitrogen map and a clear phosphorus map correspond directly to the carbon map, thus confirming that the phosphorus is present all over the nanotube mat, and not only confined to the metallic particles. EDX quantification showed a phosphorus content of 0.5 at%, while the detected nitrogen content was 1.5 at%.

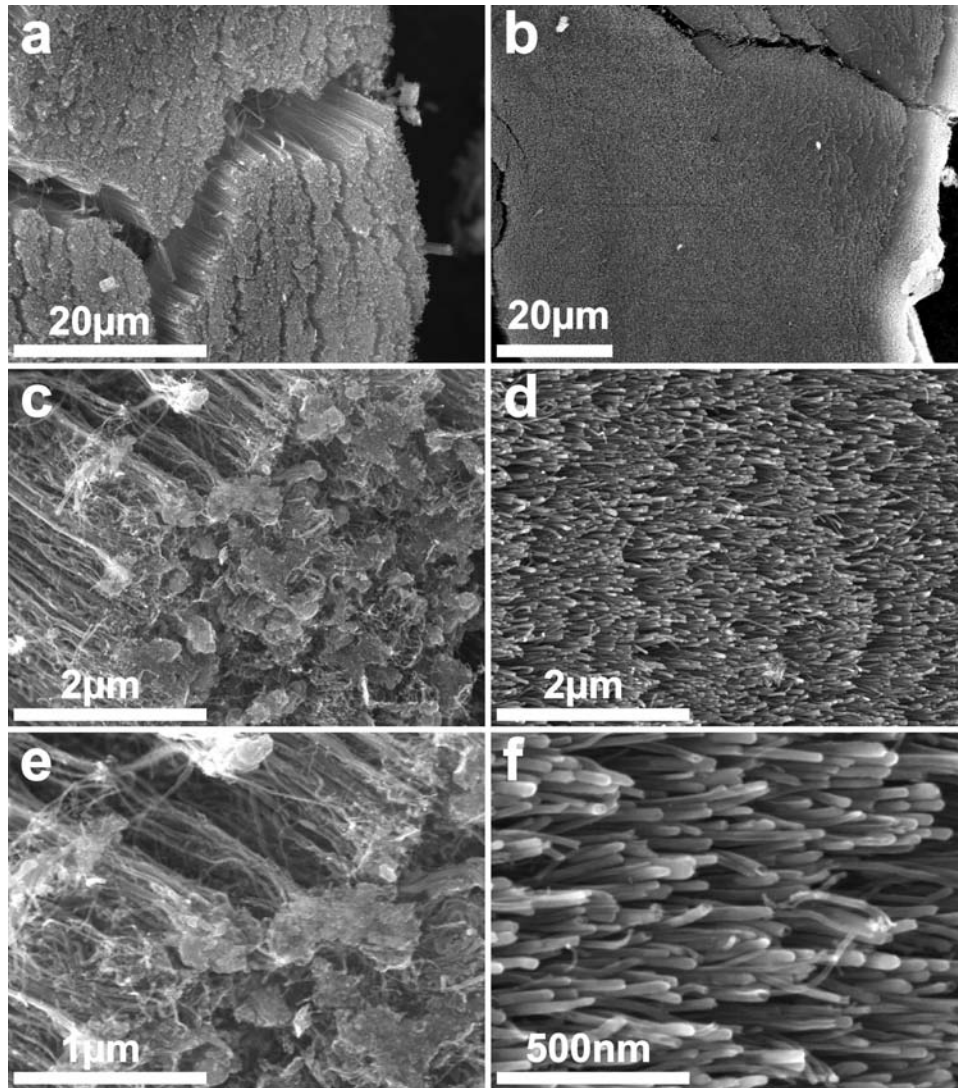


Figure 2.8: SEM images of PN-doped MWCNT mats indicating a root-growth process. a) A nanotube mat viewed from the top; and b) another mat viewed from the bottom; c,d) higher magnification of images a and b; e) detailed image of a nanotube mat viewed from the top. It is seen a disperse coating of amorphous carbon over the nanotube mat; and f) image of a nanotube mat viewed from the bottom, where the location of metal nanoparticles is evident, indicating a root-growth process.

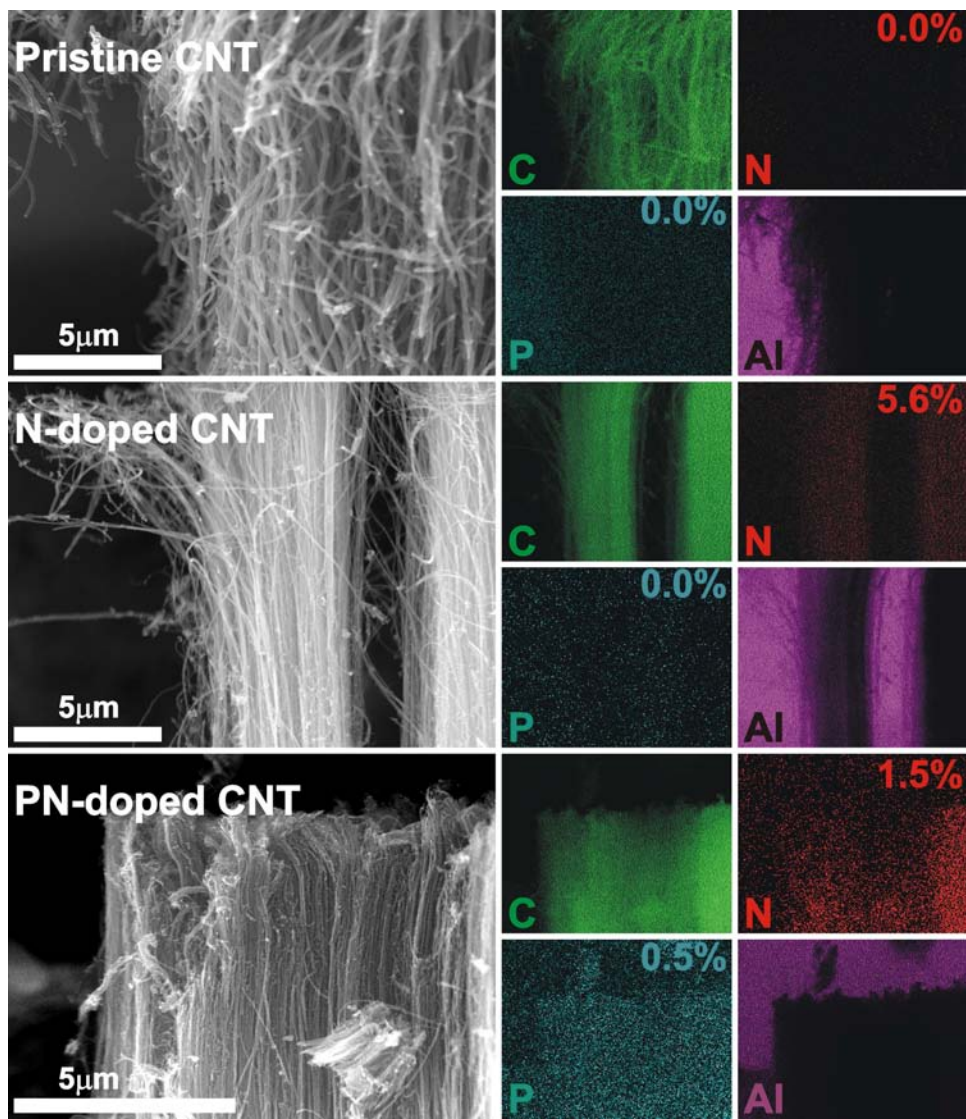


Figure 2.9: Elemental maps of pure carbon (pristine), N- and PN-doped MWCNT by EDX spectroscopy. Pure carbon MWCNT map is used as control signal and is displayed on the top frame, N-doped MWCNT map is on the center frame and PN-doped MWCNT map is on the lower frame. It is observed that while nitrogen signal can be observed both in N- and PN-doped nanotubes, its signal is lost for pure carbon nanotubes. In addition, phosphorus signal is only present in PN-doped nanotubes.

The doping of carbon nanotubes changes not only their morphology, but also their chemical properties, since the presence of foreign atoms into the hexagonal carbon lattice modifies the electronic density and its reactivity. TGA studies (see figure 2.10) provide information suggesting that the presence of phosphorus reduces the oxidation temperature (i.e. the tubes appear to be more reactive). In this case, the oxidation of PN-doped nanotubes grown under optimum conditions was compared to N-doped nanotubes grown under the same conditions, as well as to N-doped MWCNT grown at 850°C, which is their optimum growth temperature.

It was first noted that samples synthesized at lower temperatures (e.g. 760°C) have higher amounts of metal oxide byproducts after oxidation because the mass of material that did not burn corresponded to ca. 17-20%. This is because a higher proportion of metal to carbon was found due to much shorter nanotubes. The inset of Figure 2.10 shows the derivative of the normalized weight vs. temperature. When comparing the TGA data for N-doped samples only, a 20°C shift in the oxidation onset temperature can be attributed to the higher amounts of N within the tubes produced at lower temperature, and to their higher amount of defects due to their

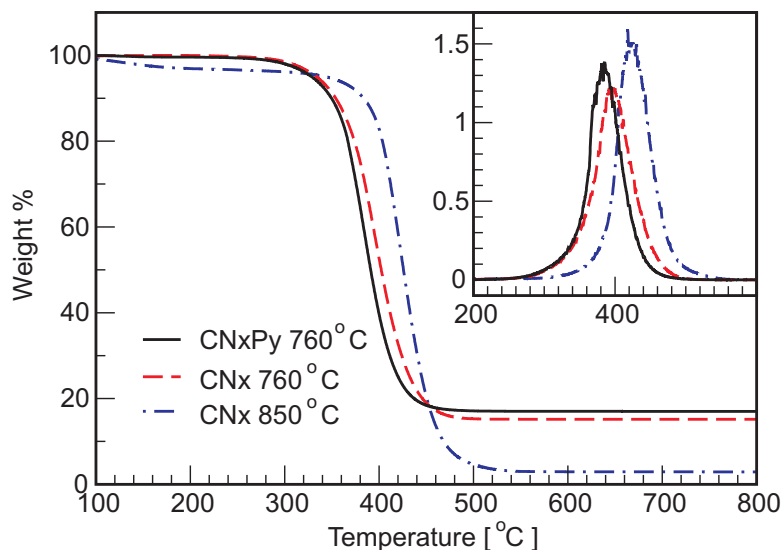


Figure 2.10: Thermogravimetric scan of samples A and C, compared to a control sample of N-doped MWCNT synthesized at 850°C. The reduction in the synthesis temperature causes a shift of ca. 20°C to lower oxidation temperatures, and the inclusion of phosphorus causes a further shift of ca. 15°C.

poorer crystallinity, thus making the tubes more reactive. However, addition of phosphorus makes a further shift of 15°C towards lower temperatures. Given the remarkably low content of amorphous carbon and the cleanliness of the sample, this shift confirms the higher chemical reactivity for the heteroatomic PN-doped carbon nanotubes when compared to the N-doped nanotube sample produced under the same experimental conditions.

In order to understand the role of phosphorus and its relation to iron during growth, X-ray powder diffraction studies were performed on a sample synthesized with 2.5 wt% of TPP (see Fig. 2.11). The bulk diffraction pattern shows a combination of two phases of iron phosphide (Fe_2P and Fe_3P) in addition to iron carbide (Fe_3C , bainite). The main peak in the diffraction pattern is due to the (0 0 2) reflection of graphite, which is characteristic of multiwalled carbon nanotubes. The peaks located between 40 and 50 degrees (see inset of Fig. 2.11) are due to a combination of reflections arising from Fe_2P , Fe_3P and Fe_3C , as indicated on the figure. The major peak in this region is the sum of the reflections (1 1 1) from Fe_3C , (4 2 0) from Fe_3P and (2 0 1) from Fe_2P .

When analyzing non-overlapping peaks from the XRD spectra, it was found that the mean particle size for Fe_3P was close to 17nm [calculated using Scherrer's

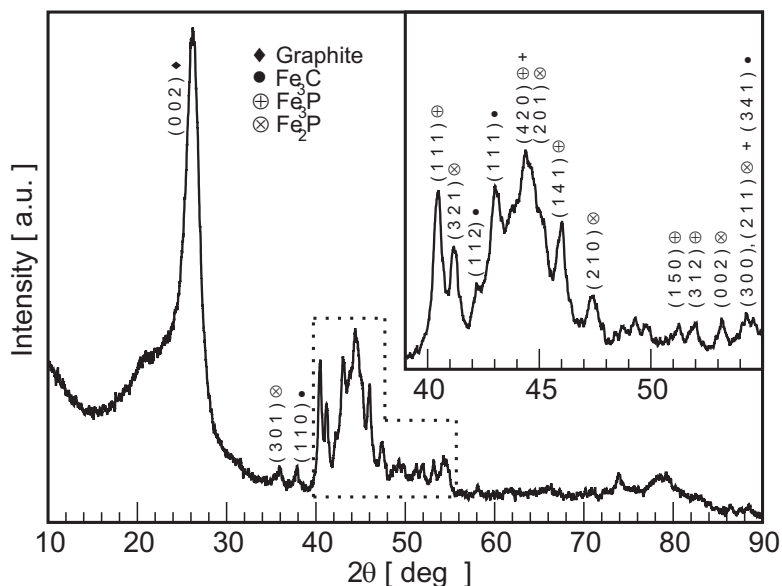


Figure 2.11: X-ray diffractogram of PN-doped MWCNT from sample A. Two phases of iron phosphide (Fe_2P and Fe_3P) and one of iron carbide (Fe_3C , bainite) are present.

equation with the full width at half maximum (FWHM) of peaks (1 1 1) and (1 4 1) of Fe_3P]. Note that these values are in agreement with the Fe_3P particle sizes observed by TEM (see fig. 2.12). For the (3 0 1) and (2 1 0) reflections of Fe_2P , the mean particle size was found to be close to 13nm, and for the Fe_3C (1 1 1) and (1 1 2) reflections, the mean size was estimated as 10–12 nm.

In order to develop a better understanding of the composition and growth process, nanotubes and their catalytic metal particles were analyzed by high resolution transmission electron microscopy (HRTEM). It is noteworthy that PN-doped nanotubes are less stable under the electron beam than their N-doped counterparts, visibly degenerating after shorter exposure times. This confirms once more the higher reactivity of PN-doped nanotubes.

In figure 2.12a and b, the detail of a nanotube tip and its catalytic metal particle is displayed. Most of the metal particles were single crystals, although some twinned crystals were observed. The fringes observed in figure 2.12b have an interplanar distance of 1.97Å, which corresponds to the (1 4 1) family of planes for Fe_3P . Their strong periodicity is confirmed by the Fourier transform of the crystal image, as displayed in figure 2.12c, where the arrow indicates the clear peak that represents the fringes of the referred crystal.

The microanalysis of a PN-doped MWCNT tip was performed by scanning transmission electron microscopy (STEM) and a high angle annular dark field (HAADF) detector. The image on figure 2.12d displays the nanotube tip, while the red line indicates the path of the STEM probe for the EDX elemental microanalysis on the tip. The elemental profile clearly shows a homogeneous composition of Fe and P. EDX quantification reveals a composition of 24 at.% of phosphorus and 76 at.% of iron, very close to the stoichiometry of Fe_3P . All the catalytic particles analyzed by EDX spectroscopy consisted of iron phosphide.

In figure 2.13a, a low resolution image shows the morphology of a nanotube mat, confirming that most of the catalytic particles are aligned on one side of the mat, as was described on the SEM images shown in figure 2.8. This is indicative of a root-growth process.

Figure 2.13b displays a closer look exhibiting the general morphology of the

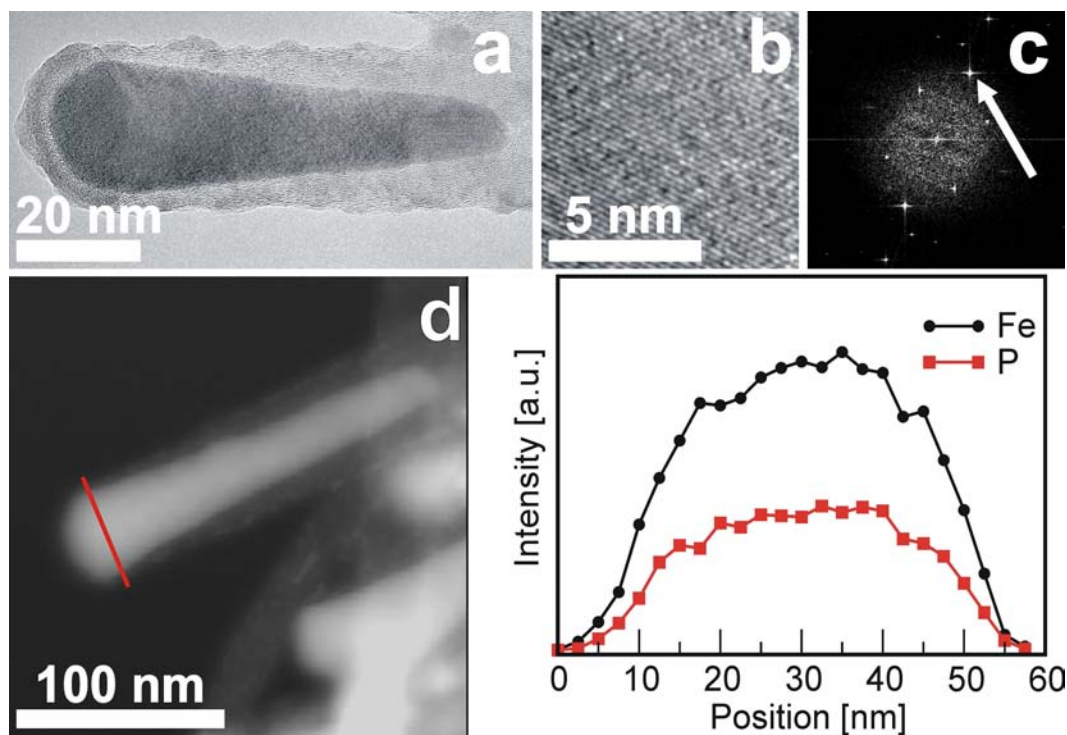


Figure 2.12: Structure and chemical composition of a PN-doped MWCNT tip. a) High resolution image of a nanotube tip displaying the conical shape of the metal particle; b) detail of the metal particle structure. Lattice fringes are clearly seen; c) Fourier transform of the image from (b), where the bright spot indicated by the arrow represents the family of lattice planes seen on the fringes of image (b); d) high angle annular dark field (HAADF) STEM image of a nanotube tip. The EDX elemental line profile is displayed, showing an homogeneous composition of Fe and P within the catalytic particle.

nanotubes, confirming that most of them consist of bamboo shaped nanotubes, typical of nitrogen doped MWCNT. A high resolution image of a nanotube shown in figure 2.13c displays the high degree of graphitization in the nanotube walls, and even in the compartments of the bamboo structure. Figure 2.13d and e display the structure of a typical nanotube tip, as well as the interface between the metal particle and the nanotube walls, where the graphitization is poorer than along the nanotube walls (figure 2.13c), which could be due to the strain in the lattice caused by a lower mobility of carbon due to the presence of the metal phosphide.

Energy filtered images constitute a great tool to understand the composition of heterogeneous materials. In this case, images were obtained from sample A, and it can be observed that most of the catalytic particles are primarily composed of

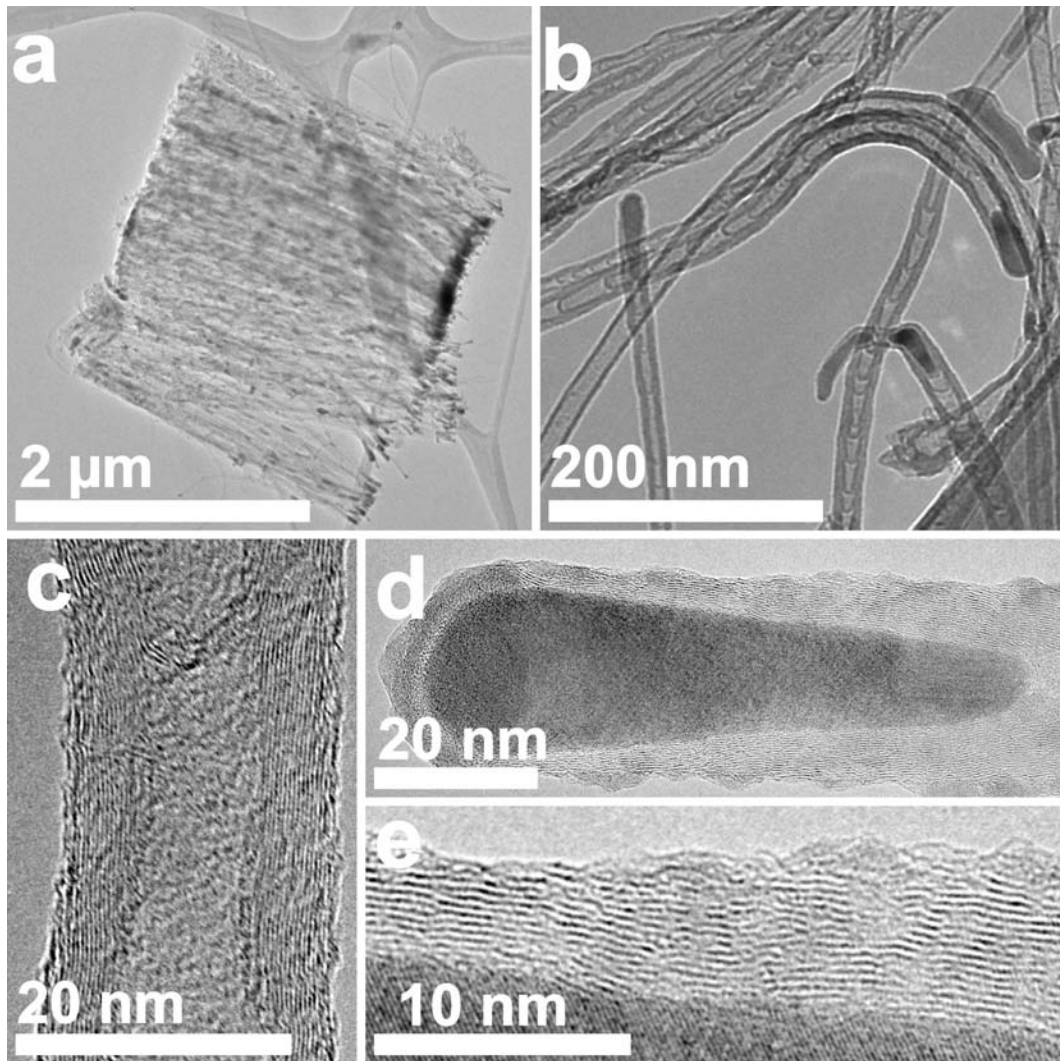


Figure 2.13: High resolution transmission electron microscope (HRTEM) images of sample A. a) Low magnification image displaying the general overview of a nanotube mat; b) image displaying the bamboo structure of nanotubes; c) high resolution image of a nanotube wall, displaying a high graphitization degree; d) image of a typical nanotube tip revealing a conical catalytic particle; and e) high resolution image of the interface of the metal particle and the carbon nanotube from d).

iron and phosphorus (see fig. 2.14). The bright field image shows the bamboo-like structure of the nanotubes, but also some straight nanotubes can be seen in the same image. In figure 2.15, metal particles exhibit a small amount of oxygen at the far end of the tip, which is either due to oxidation or obtained from the silicon oxide (quartz) substrate during growth.

The electron energy loss spectrum (EELS) from a nanotube shown in figure 2.16

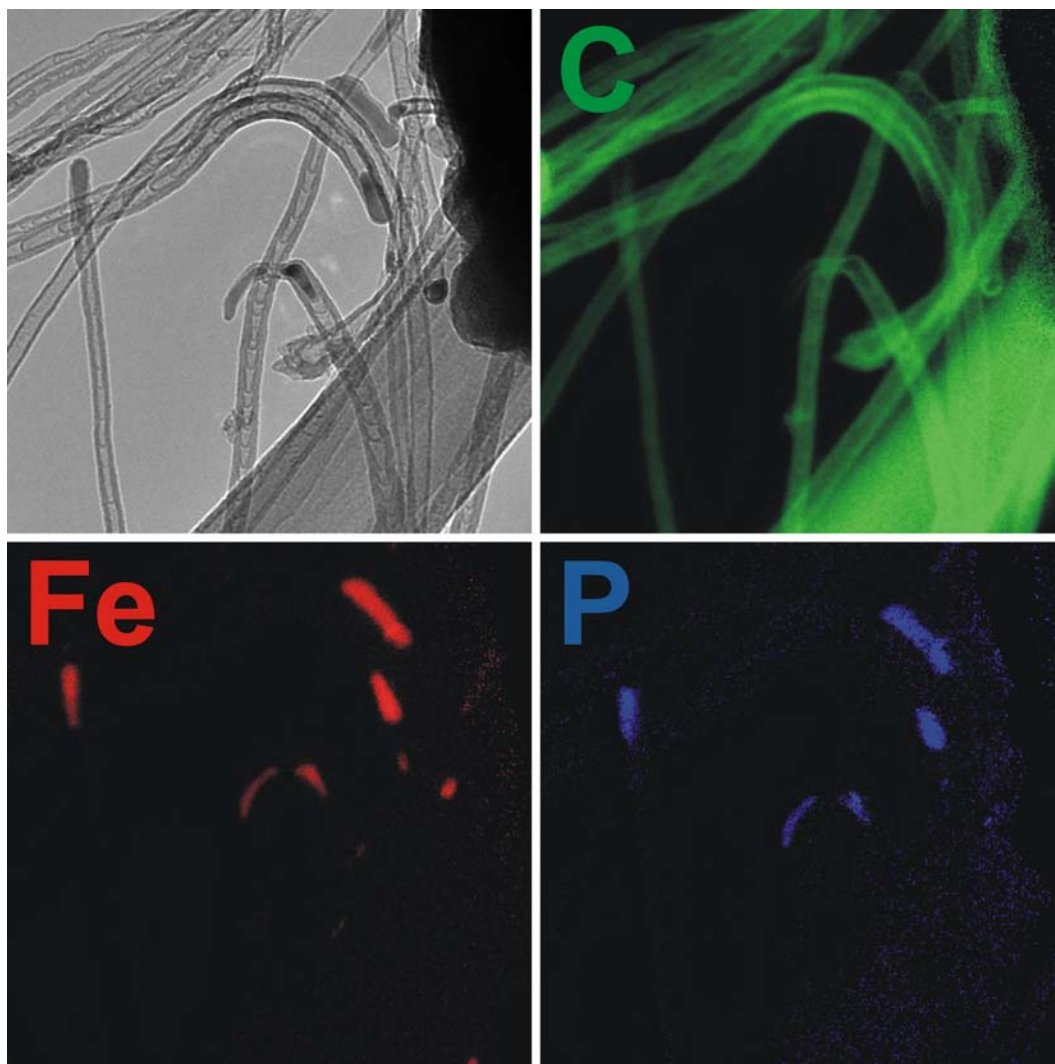


Figure 2.14: Energy filtered elemental maps of PN-doped MWCNTs, with maps for carbon (C), iron (Fe), and phosphorus (P). It can be observed that the metallic particles are composed of an iron phosphide phase, while the signal of phosphorus is not strong enough to appear on the nanotube lattice.

reveals the presence of carbon, nitrogen, and phosphorus; although nitrogen signal is masked by the tail of the carbon edge and phosphorus signal is masked by the inelastic scattering peak. Although this spectrum shows the three elements, it can not be concluded that phosphorus and nitrogen are effectively incorporated into the nanotube lattice.

Therefore, elemental profiles are needed to effectively confirm that PN-doped nanotubes were indeed synthesized, but first, signal to noise ratio had to be improved in order to obtain reliable profiles. In order to overcome this inconvenient, the dwell

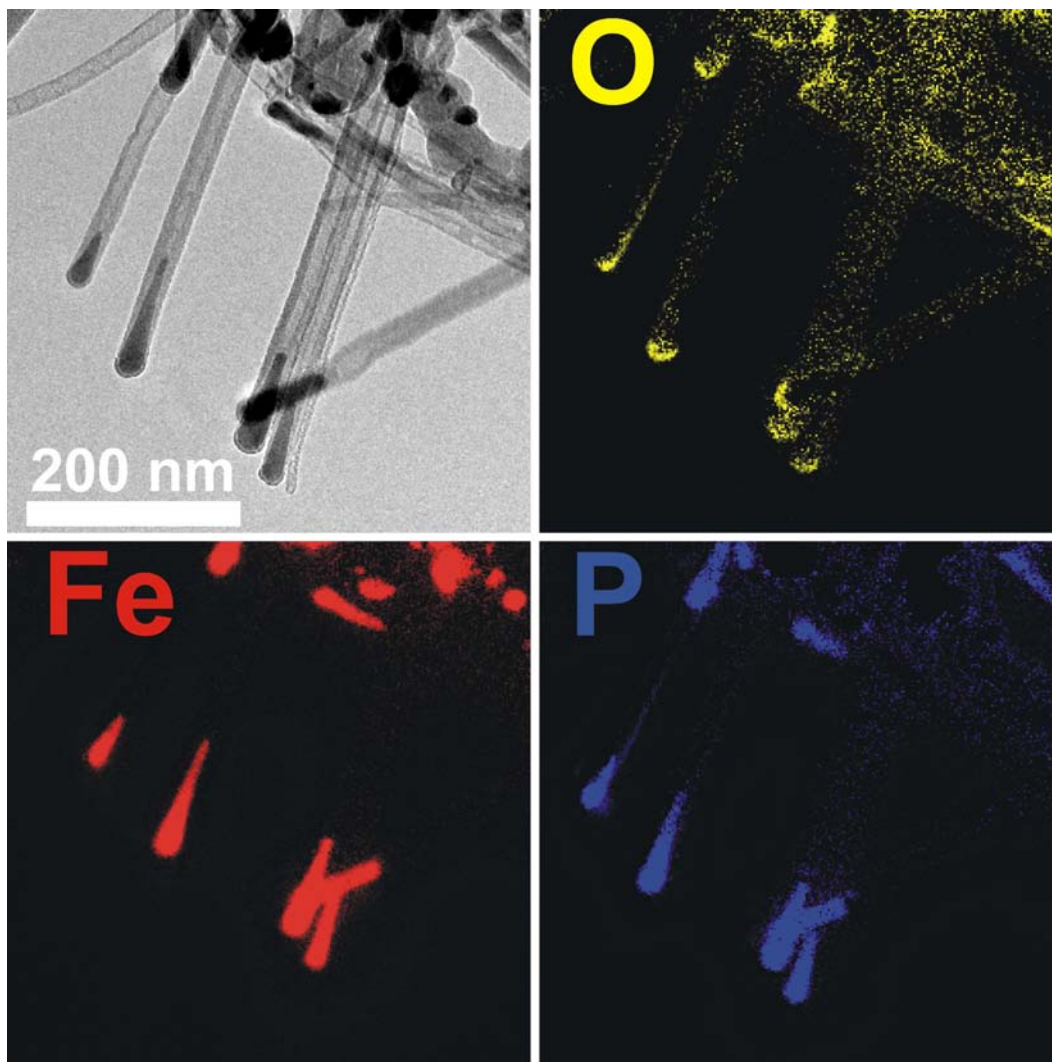


Figure 2.15: Energy filtered elemental maps of the metallic catalytic particles of PN-doped MWCNT, with maps for oxygen (O), iron (Fe), and phosphorus (P). The presence of oxygen in the far end of the nanotube tip could be due to air-oxidation or acquired from the quartz substrate during growth.

time was increased up to 3 seconds per spot, while the energy resolution of the collected spectra was increased. As a result, only binary profiles such as the C-P and C-N were obtained due to heavy damage caused to nanotubes by the electron beam while the consecutive EELS spectra were collected.

EELS line scans along the nanotubes close to the catalytic particle indicated that the carbon nanotubes have a homogeneous distribution of phosphorus, which has a weak signal that follows the profile of carbon (see 2.17a). In order to rule out a possible noise effect originating from the overlapping of the inelastic scattering peak

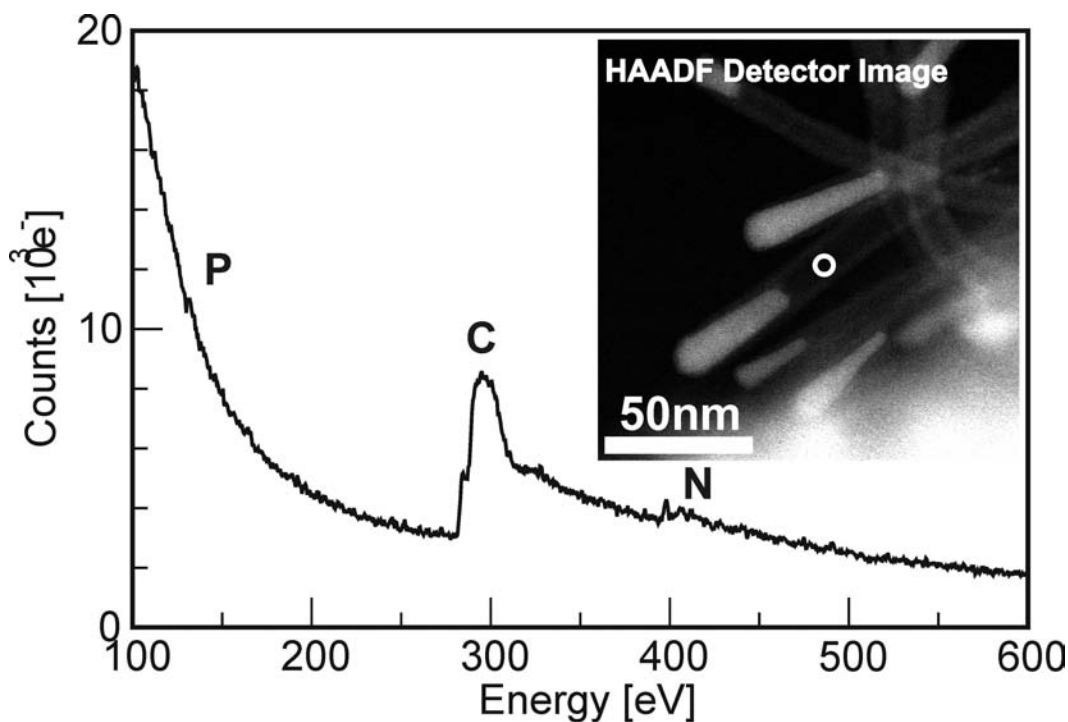


Figure 2.16: Electron energy loss spectrum of a PN-doped MWCNT from sample A, obtained from the spot marked in the high angle annular dark field (HAADF) image. The position of the carbon edge is clear, while small signals from nitrogen and phosphorus are masked by the tail of the carbon edge and the inelastic scattering peak, respectively.

with the phosphorus signal, the silicon signal (ca. 30 eV lower than phosphorus) was also integrated.

It can be seen that while the integrated silicon signal (green) remains with a value close to zero, the integrated phosphorus signal (red) increases and decreases together with the carbon signal (black). This indicates a homogeneous doping of phosphorus within the carbon nanotube. TEM images show bamboo-shaped nanotubes, which are characteristic of nitrogen-doped nanotubes [2, 28, 30], and EELS detected nitrogen traces within the nanotube walls. In addition, nitrogen gas was clearly detected in the gaseous phase within the bamboo compartments (see figure 2.17b), a feature observed only in N-doped nanotubes [28]. The presence of both phosphorus and nitrogen within the nanotube walls confirms that these nanotubes have been heteroatomically doped.

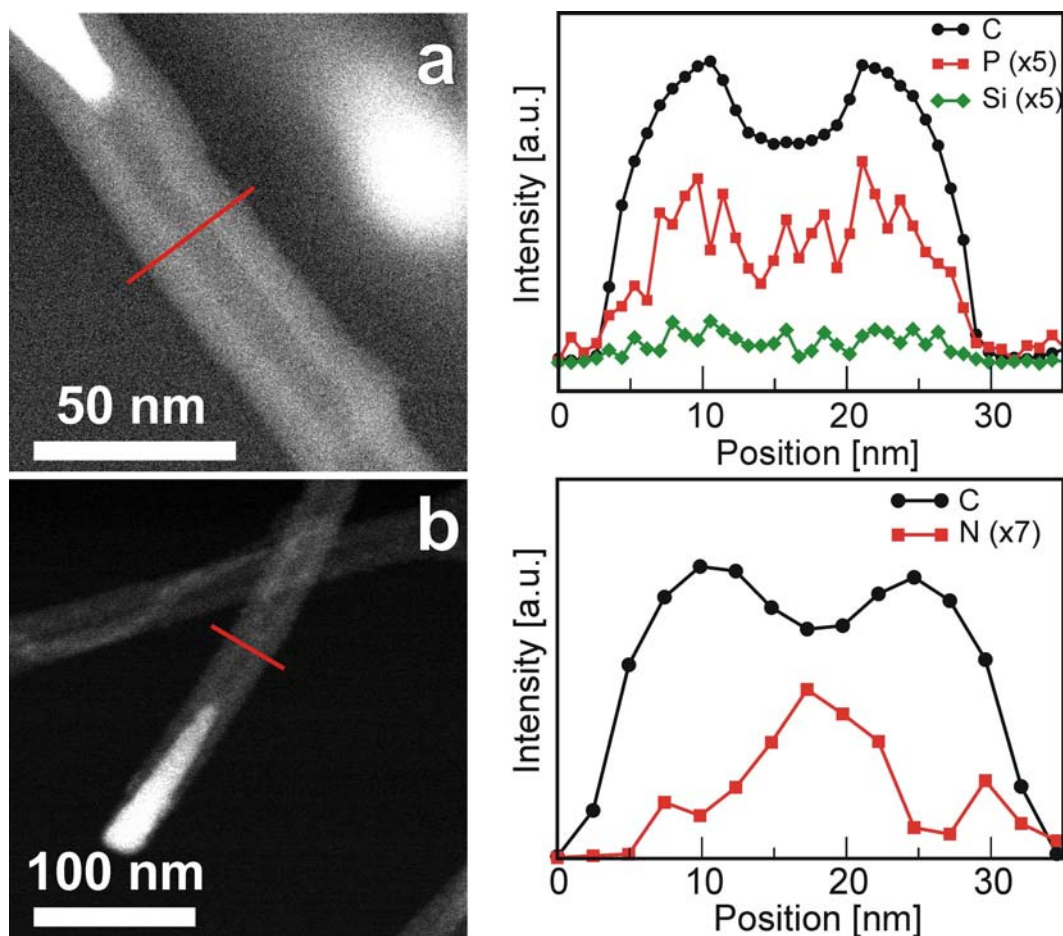


Figure 2.17: Elemental line profiles of PN-doped MWCNT. a) Phosphorus (P), silicon (Si) and carbon (C) profiles, displaying a phosphorus profile that corresponds to carbon signal; b) Nitrogen (N) and carbon (C) profiles, displaying a clear content of gaseous nitrogen in the nanotube core, while also displaying traces of nitrogen within nanotube walls.

2.5 Growth of PN-doped Carbon Nanotubes

The ternary bulk phase diagram of carbon-iron-phosphorus [31] shows a metastable boundary between Fe_3C and Fe_3P at 700 °C, with an eutectic point close to 966°C for 12.8 at% of carbon in Fe_3P . Also, from this phase diagram it can be concluded that Fe_2P cannot coexist as a solid solution with Fe_3C at the synthesis temperature range used in this study. Based mainly on experimental observations from these samples, the first hypothesis on the growth mechanism of PN-heteroped CNTs can be proposed.

The growth of these nanotubes is found to be catalyzed by iron phosphide par-

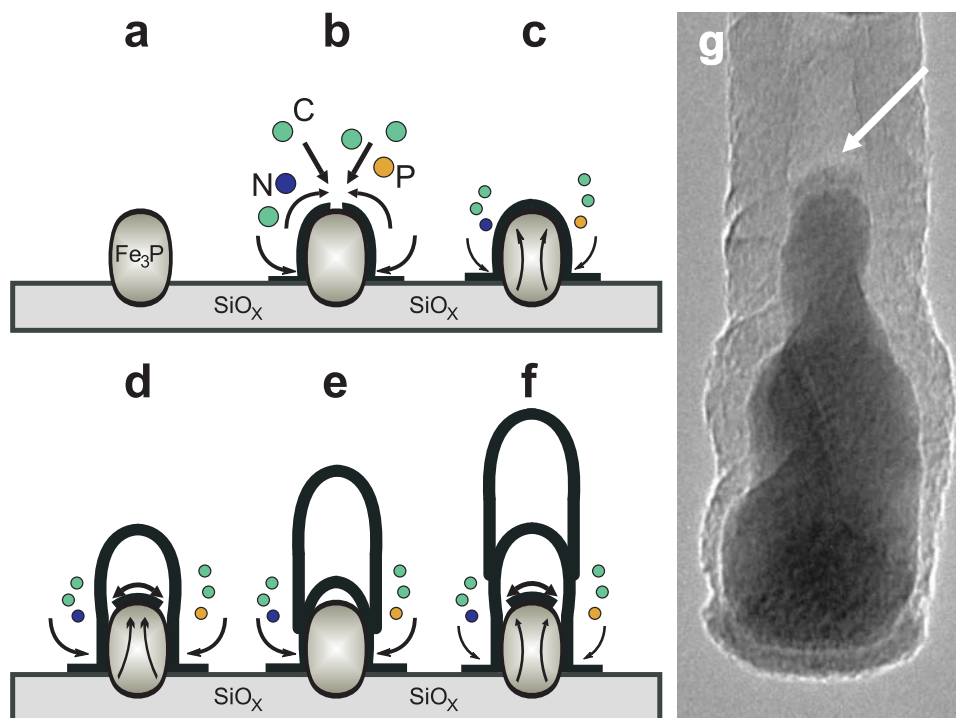


Figure 2.18: Root growth model proposed for the PN doped nanotubes. A metal particle attached to the substrate (a) nucleates a graphitic layer (b,c), which also includes P and N present in the environment. The stress induced by curvature and a high surface diffusion rate causes the nanotube to start growing from this particle (d). The diffusion through the catalyst of C, P, and N causes the formation of a graphite layer in the interior of the nanotube, which in turn displaces the growing nanotube (e) and crates a bamboo compartment (f). the repetition of this process leads to a bamboo-like PN doped nanotube.

ticles, and proceeds via a root growth mechanism, as concluded from SEM and HRTEM observations. As it was shown in a recent publication [30], nitrogen substitution has a lower energetic cost when located in positions close to the edges, promoting the closure of nanotube and creating positive curvature. It will be also shown (see chapter 3) that the inclusion of phosphorus into the graphene layer creates large corrugation and local positive curvature due to tetragonal bonding angles. Carbon nanotubes grow from a supersaturated Fe_3C [32], and this compound could be formed at the surface of Fe_3P while it is dissolving carbon, but not in Fe_2P . This would explain why the yield of carbon nanotubes is reduced with increased phosphorus content in the feedstock solution.

Based on these observations, we propose a growth model for PN hetero-doped

multiwalled CNT. This model takes into account both the diffusion over the surface of the catalyst [33] and the diffusion through the metal catalyst [34] models as described by Oberlin et al. [35], and depicted in Figure 2.18.

In the first stages, Iron phosphide nanoparticles that are attached to the substrate (fig. 2.18a) promote the condensation of gaseous carbon, nitrogen and phosphorus atoms over a liquid-like metal particle. Surface diffusion plays a key role in the migration of these condensed species, creating a graphitic layer that diffuses to the colder side of the metal particle (fig. 2.18b), although diffusion through metal particle at this stage cannot be discarded. In this process, the inclusion of nitrogen atoms in open edges during the formation of the graphite layer seems feasible.

The condensation of carbon, phosphorus and nitrogen atoms keeps taking place at the contact angle of the particle and the substrate, building up several doped graphitic layers (fig. 2.18c). The stress caused by the curvature induced by the doping atoms [30], in conjunction with the lateral surface diffusion causes the graphitic shell to separate from the catalyst in its top side, and the growth of the nanotube begins (fig. 2.18d).

Diffusion through the metal particle causes carbon and doping atoms to buildup at the catalyst surface located inside the nanotube. Figure 2.18g shows a TEM image where this deposit is indicated by the arrow. Once this graphite layer grows beyond its available surface, it exerts stress in the nanotube wall, which in turn could be separated from the catalyst, and replaced by the new graphite layer that grows underneath (fig. 2.18e). This new graphitic shell over the metal particle is subject again to stress in its top side, separating again from the metal particle, and a new bamboo compartment is formed (fig. 2.18e). The process is repeated and the bamboo-like nanotube is formed (fig. 2.18f). The high mobility of atoms at the typical synthesis temperatures makes possible that the stress induced by the curved graphitic shells on the metal catalyst is likely to change its shape to a conical section, which is typically observed by TEM.

2.6 Conclusions

In summary, the successful synthesis of phosphorus- and nitrogen-doped carbon nanotubes by a CVD method using benzylamine and triphenylphosphine as nitrogen and phosphorus sources was successful.

EDX and EELS spectroscopy, as well as EELS elemental line profiles confirmed the presence of both nitrogen and phosphorus within carbon nanotubes. From X-ray diffraction studies it was concluded that small nanoparticles of two iron phosphide phases (Fe_3P and Fe_2P) and iron carbide (Fe_3C) were present, with mean particle sizes in the range of 10–20nm. Although some iron particles can be seen in the elemental mappings, EDX and EELS spectroscopy indicate that most of the catalytic particles are composed of iron phosphide (Fe_3P).

A reduction in the yield of carbon nanotubes was observed as the content of phosphorus in the hydrocarbon solution was increased, denoting a possible reduction in the catalytic activity of iron phosphide when compared to pure iron. The obtained nanotubes grew aligned, arranging themselves into mats, and there is evidence that points towards a root-grow process, which is consistent with previous reports [28].

The inclusion of phosphorus atoms disrupts the inert graphene surface, and as it was shown by TGA analysis, it modifies the carbon nanotube chemical properties, displaying a lower oxidation temperature when compared to N-doped nanotubes. This could be used for new applications based on the different chemical reactivity of the obtained nanotubes, such as new gas detectors or in new composite materials.

References

- [1] T. Nozaki and K. Yazawa. The radioactivation analysis of graphite for nitrogen by the $^{14}\text{N}(p,\alpha)^{11}\text{C}$ reaction. *Bulletin of the Chemical Society of Japan*, 37: 1891–1892, 1964.
- [2] M. Terrones, A. Jorio, M. Endo, A. M. Rao, Y. A. Kim, T. Hayashi, H. Terrones, Jean-Cristophe Charlier, G. Dresselhaus, and M. S. Dresselhaus. New direction in nanotube science. *Materials Today*, 7(10):30–45, October 2004.
- [3] J.-Y. Yi and J. Bernholc. Atomic structure and doping of microtubules. *Physical Review B*, 47:1708–1711, 1993.
- [4] O. Stephan, P. M. Ajayan, C. Colliex, Ph. Redlich, J. M. Lambert, P. Bernier, and P. Lefin. Doping Graphitic and Carbon Nanotube Structures with Boron and Nitrogen. *Science*, 266:1683–1685, 1994.
- [5] Y. Zhang, H. Gu, K. Suenaga, and S. Iijima. Heterogeneous growth of b—c—n nanotubes by laser ablation. *Chemical Physics Letters*, 279:264–269, 1997.
- [6] M. Terrones, N. Grobert, J. Olivares, J.P. Zhang, H. Terrones, K. Kordatos, W.K. Hsu, J. P. Hare, P.D. Townsend, K. Prassides, A.K. Cheetham, H.W. Kroto, and D.R.M. Walton. Controlled production of aligned-nanotube bundles. *Nature*, 388:52–55, 1997.
- [7] M. Terrones, P. Redlich, N. Grobert, S. Trasobares, W.-K. Hsu, H. Terrones, Y.-Q. Zhu, J.P. Hare, C.L. Reeves, A.K. Cheetham, M. Rhle, H.W. Kroto, and D.R.M. Walton. Carbon nitride nanocomposites: Formation of aligned C_xN_y nanofibers. *Advanced Materials*, 11:655–658, 1999.
- [8] M. Glerup, J. Steinmetz, D. Samaille, O. Stephan, S. Enouz, A. Loiseau, S. Roth, and P. Bernier. Synthesis of n-doped swnt using the arc-discharge procedure. *Chemical Physics Letters*, 387:193–197, 2004.
- [9] G. Keskar, R. Rao, J. Luo, J. Hudson, J. Chen, and A.M. Rao. Growth, nitrogen doping and characterization of isolated single-wall carbon nanotubes using liquid precursors. *Chemical Physics Letters*, 412:269–273, 2005.

- [10] F. Villalpando-Paez, A. Zamudio, A.L. Elias, H. Son, E.B. Barros, S.G. Chou, Y.A. Kim, H. Muramatsu, T. Hayashi, J. Kong, H. Terrones, G. Dresselhaus, M. Endo, M. Terrones, and M.S. Dresselhaus. Synthesis and characterization of long strands of nitrogen-doped single-walled carbon nanotubes. *Chemical Physics Letters*, 424:345–352, 2006.
- [11] N. Fujimori, T. Imai, and A. Doi. Characterization of conducting diamond films. *Vacuum*, 36(1–3):99–102, 1986.
- [12] K. Okano, H. Kiyota, T. Iwasaki, Y. Nakamura, Y. Akiba, T. Kurosu, M. Iida, and T. Nakamura. Synthesis of n-type semiconducting diamond film using diphosphorus pentaoxide as the doping source. *Applied Physics A*, 51:344–346, 1990.
- [13] M. Akaishi, H. Kanda, and S. Yamaoka. Phosphorus: an elemental catalyst for diamond synthesis and growth. *Science*, 259:1592–1593, March 1993.
- [14] S. Koizumi, M. Kamo, Y. Sato, H. Ozaki, and T. Inuzuka. Growth and characterization of phosphorus doped {111} homoepitaxial diamond thin films. *Applied Physics Letters*, 71(8):1065–1067, August 1997.
- [15] S. Koizumi, K. Watanabe, M. Hasegawa, and H. Kanda. Ultraviolet emission from a diamond pn junction. *Science*, 292:1899–1901, June 2001.
- [16] M. Nesladek. Conventional n-type doping in diamond: state of the art and recent progress. *Semiconductor Science and Technology*, 20:R19–R27, 2005.
- [17] M. Suzuki, H. Yoshida, N. Sakuma, T. Ono, T. Sakai, and S. Koizumi. Electrical characterization of phosphorus-doped n-type homoepitaxial diamond layers by schottky barrier diodes. *Applied Physics Letters*, 84(13):2349–2351, March 2004.
- [18] S. Motojima, I. Hasegawa, S. Kagiya, M. Moriyama, M. Kawaguchi, and H. Iwanaga. Preparation of coiled carbon fibers by pyrolysis of acetylene using a ni catalyst and sulfur or phosphorus compound impurity. *Applied Physics Letters*, 62(19):2322–2323, May 1993.

- [19] S. Motojima, I. Hasegawa, S. Kagiya, K. Andoh, and H. Iwanaga. Vapor phase preparation of micro-coiled carbon fibers by metal powder catalyzed pyrolysis of acetylene containing a small amount of phosphorus impurity. *Carbon*, 33(8): 1167–1173, 1995.
- [20] L. Ci, H. Zhu, B. Wei, J. Liang, C. Xu, and D. Wu. Phosphorus – a new element for promoting growth of carbon filaments by the floating catalyst method. *Carbon*, 37(10):1652–1654, 1999.
- [21] F. Benissad-Aissani, H. Aït-Amar, M.-C. Schouler, and P. Gadelle. The role of phosphorus in the growth of vapour-grown carbon fibres obtained by catalytic decomposition of hydrocarbons. *Carbon*, 42(11):2163–2168, 2004.
- [22] Y. Wen and Z. Shen. Synthesis of regular coiled carbon nanotubes by Ni-catalyzed pyrolysis of acetylene and a growth mechanism analysis. *Carbon*, 39: 2369–2374, 2001.
- [23] D. Ding, J. Wang, Z. Cao, and J. Dai. Synthesis of carbon nanostructures on nanocrystalline Ni-Ni₃P catalyst supported by sic whiskers. *Carbon*, 41: 579–582, 2003.
- [24] V. Jourdain, H. Kanzow, M. Castignolles, A. Loiseau, and P. Bernier. Sequential catalytic growth of carbon nanotubes. *Chemical Physics Letters*, 364(1): 27–33, September 2002.
- [25] V. Jourdain, O. Stéphan, M. Castignolles, A. Loiseau, and P. Bernier. Controlling the morphology of multiwalled carbon nanotubes by sequential catalytic growth induced by phosphorus. *Advanced Materials*, 16(5):pp447–453, March 2004.
- [26] V. Jourdain, M. Paillet, R. Almairac, A. Loiseau, and P. Bernier. Relevant synthesis parameters for the sequential catalytic growth of carbon nanotubes. *Journal of Physical Chemistry B*, 109:1380–1386, 2005.
- [27] V. Jourdain, E. T. Simpson, M. Paillet, T. Kasama, R. E. Dunin-Borkowski, P. Poncharal, A. Zahab, A. Loiseau, J. Robertson, and P. Bernier. Periodic

- inclusion of room-temperature-ferromagnetic metal phosphide nanoparticles in carbon nanotubes. *Journal of Physical Chemistry B*, 110(20):9759–9763, 2006.
- [28] M. Reyes-Reyes, N. Grobert, R. Kamalakaran, T. Seeger, D. Golberg, M. Rühle, Y. Bando, H. Terrones, and M. Terrones. Efficient encapsulation of gaseous nitrogen inside carbon nanotubes with bamboo-like structure using aerosol thermolysis. *Chemical Physics Letters*, 396:167–173, 2004.
- [29] M. Pinault, M. Mayne-L’Hermite, C. Reynaud, V. Pichot, P. Launois, and D. Ballutaud. Growth of multiwalled carbon nanotubes during the initial stages of aerosol-assisted CCVD. *Carbon*, 43:2968–2976, 2005.
- [30] B. G. Sumpter, V. Meunier, J. M. Romo-Herrera, E. Cruz-Silva, D. A. Cullen, H. Terrones, D. J. Smith, and M. Terrones. Nitrogen-mediated carbon nanotube growth: Diameter reduction, metallicity, bundle dispersability, and bamboo formation. *ACS Nano*, 1(3):xx–yy, 2007.
- [31] P. Villars, A. Prince, and H. Okamoto, editors. *Handbook of Ternary Alloy Phase Diagrams*, chapter C-Fe-P Phase Diagram, pages 6786–6793. ASM International, 1995.
- [32] J.A. Rodriguez-Manzo, M. Terrones, H. Terrones, H.W. Kroto, L. Sun, and F. Banhart. In situ nucleation of carbon nanotubes by the injection of carbon atoms into metal particles. *Nature Nanotechnology*, 2:307–311, 2007.
- [33] T. Baird, J.R. Fryer, and B. Grant. Carbon formation on iron and nickel foils by hydrocarbon pyrolysis reactions at 700°C. *Carbon*, 12:591–602, 1974.
- [34] R.T.K. Baker, M.A. Barber, P.S. Harris, F.S. Feates, and R.J. Waite. Nucleation and growth of carbon deposits from the nickel catalyzed decomposition of acetylene. *Journal of Catalysis*, 26:51–62, 1972.
- [35] A. Oberlin, M. Endo, and T. Koyama. Filamentous growth of carbon through benzene decomposition. *Journal of Crystal Growth*, 32:335–339, 1976.

Chapter 3

PN Heteroatomic doping of carbon nanotubes: a theoretical study

In this chapter, a study of the electronic structure of heteroatomically doped carbon nanotubes is presented. Previous studies of nitrogen and phosphorus doping of sp^2 carbon structures are reviewed, while a model for PN doped carbon nanotubes is proposed. The structural, transport and chemical properties are evaluated using first principles electronic structure calculations and molecular dynamics.

3.1 Methods

When it comes to *ab initio* first principles calculations, there are two main approaches that are used, one is the use of atomic-centered basis described by Gaussian type orbitals (GTO), which provides a reduced basis for finite systems. The other approach is the use of a delocalized basis using plane waves, which is very useful for periodic systems, but the basis size increases rapidly with the number of atoms present in the repeating unit.

In this work, the electronic structure of phosphorus- and nitrogen- doped carbon nanotubes was calculated using the code SIESTA [1]. This code was chosen in order to reduce the computational cost due to the large size of the systems under study

(around 200 atoms), while still retaining the accuracy provided by *ab initio* first principles methods. The SIESTA code implements the Kohn-Sham self consistent Density Functional method [2, 3] on periodic systems using a linear combination of numerical pseudo-atomic orbitals described by Junquera et al. [4]. The basis size selected was a double-zeta singly polarized basis, that balances accuracy with computational cost.

For most of the present work, the local spin density approximation (LSDA) was chosen for the exchange and correlation potential, in the Ceperley-Alder parametrization of the Perdew and Zunger implementation [5, 6]. Norm conserving Troullier-Martins pseudopotentials in the Kleinman-Bylander non-local form were used to represent the core electrons [7, 8]. The electronic transport properties were calculated using the Landauer formalism and the surface Green functions matching method, as described by Nardelli [9].

In the study of the properties of doped carbon nanotubes, three different systems were explored: Graphene, understood as the limit for large diameter Nanotubes; a (10, 0) semiconducting Zigzag nanotube; and a (6, 6) Armchair metallic nanotube, as shown in figure 3.1. In all cases, supercells of adequate size were considered to assure that the doping impurities do not interact with their periodic images. This was achieved with 5 unit cells in the case of zigzag nanotube, 8 unit cells in the armchair case and a 7x7 supercell for the graphene case. All the models were relaxed using a Conjugate Gradient minimization until the maximum force was lower than 0.2 eV/Ang.

3.2 Graphene as a large nanotube model

Graphene constitutes a reasonable model when studying large diameter nanotubes, since curvature is not playing a major role in the surface physics and chemistry. Therefore, we selected the graphene model to study the plausibility of doped nanotubes with phosphorus, as well as phosphorus-nitrogen systems, which could describe the experimental results described in chapter 2.

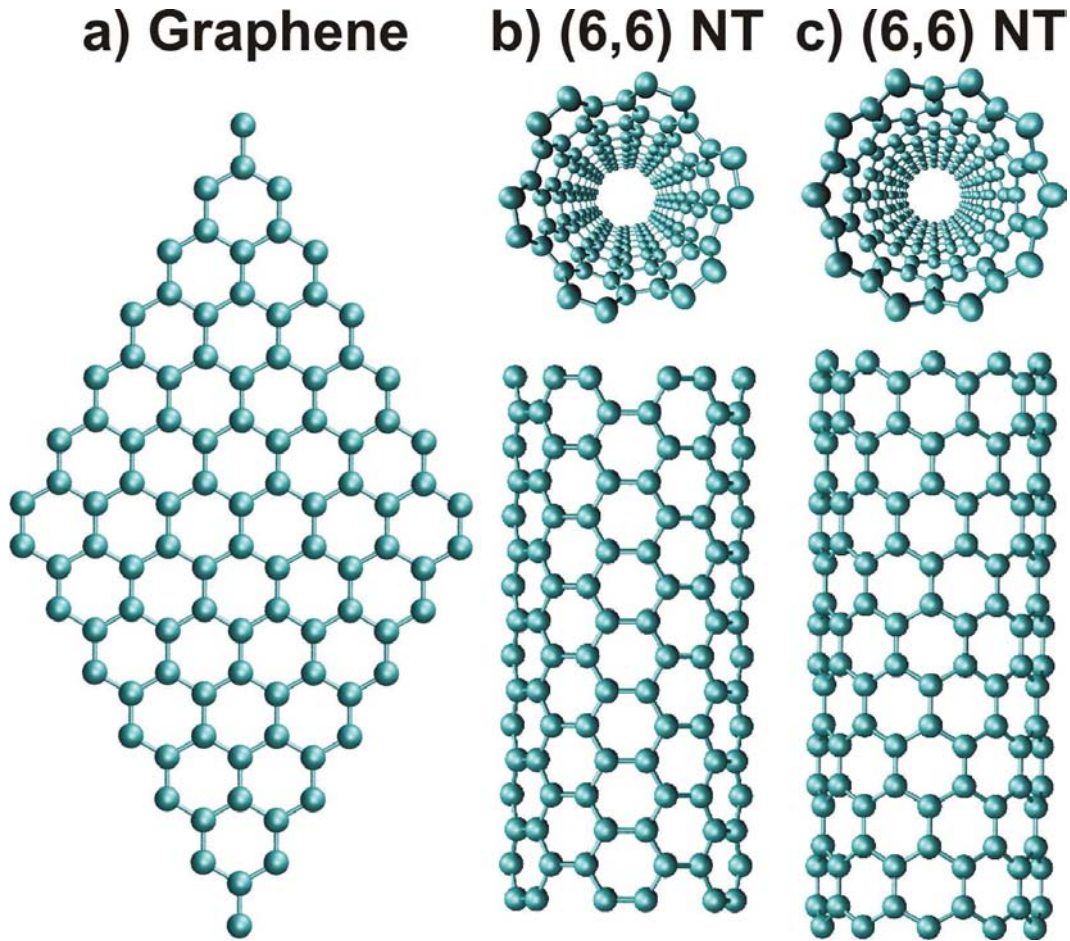


Figure 3.1: Molecular models of the studied systems, displaying their full supercell size. a) 7x7 graphene supercell. b) 5 cells of a (10,0) zigzag nanotube. c) 8 cells of a (6,6) armchair nanotube.

3.2.1 Structural characteristics of doped graphene

In order to compare the structural changes of the doped graphene with the pristine layer, the doped systems are depicted superposed to a hexagonal network that represents the pristine system. It can be observed in figure 3.2 that nitrogen doping does not cause major distortion into the carbon lattice as the image perfectly overlaps the pristine hexagonal network. The C-N bond length is slightly shorter (1.393 Å *versus* 1.420 Å, -1.86%). This shortening is compensated with small displacements of the first and second neighbors to positions closer to the nitrogen atom, but these are less than 0.7%.

In a similar situation is the N₃-vacancy system, which also overlaps the red

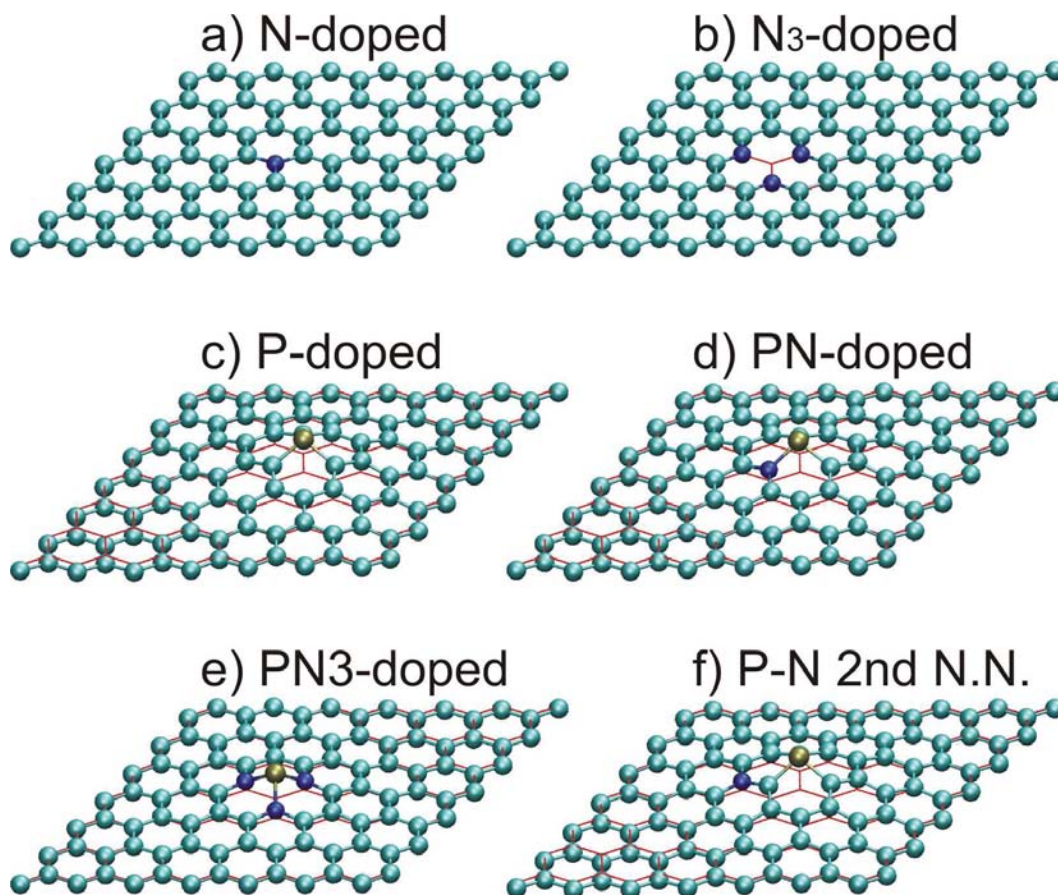


Figure 3.2: Molecular models of the doped graphene structures after relaxation. The hexagonal red line indicates the position of the undoped graphene network.

hexagonal network, except the vacancy site (figure 3.2b). In this case, the C-N bond is considerably shorter, 1.33 \AA , *versus* 1.42 \AA for a regular C-C bond; a total reduction of 6.33%. Both the nitrogen atoms and its two first neighbors are slightly off the positions of the pristine system in order to compensate the bond shortening.

The insertion of phosphorus in the hexagonal framework caused a large distortion, independently of the presence of nitrogen, (figure 3.2c to f). Phosphorus preserved its sp^3 character similar to the triphenylphosphine molecule, which makes the phosphorus to prefer a tetrahedral coordination. This is reflected in the bond angles that phosphorus has with its nearest neighbors, which are very close to 99° , the same as in triphenylphosphine. The P-C bond length is 1.79 \AA , compared to 1.42 \AA of C-C bonds. This increase of 26% in the bond length, together with the bond angles, causes phosphorus to leave the graphene layer plane, thus displacing

the positions of the first, second and third neighbors out of the plane, while other positions are less displaced, as can be seen in figure 3.2c. This could be interpreted as a corrugation induced by the presence of phosphorus.

In the PN-doped case, the presence of nitrogen helps to reduce the displacements caused by the inclusion of phosphorus, having a damping effect on the structural strain, specially within the first and second neighbors, although it is not easily seen from figure 3.2d. This effect is reflected in the total energy calculations, as will be described in the following section.

3.2.2 Total energy calculations for doped graphene systems

In order to evaluate the feasibility of doping carbon nanotubes with phosphorus and nitrogen, total energy calculations were performed in the systems described in the previous subsection. The defect formation energy was calculated from these energies in the following way: first, the binding energy of the complete supercell was calculated as shown in the following equation:

$$E_{B-SC} = E_{Total} - (N_C E_C + N_N E_N + N_P E_P) \quad (3.1)$$

Where E_{B-SC} is the binding energy of the supercell, E_{Total} is the total energy of the supercell, N_X is the number of atoms of the element X and E_X is the total energy of an isolated atom of the element X.

The defect energy is calculated by the difference of the supercell binding energy for each doped system with the undoped graphene. The N₃-vacancy system is special, because an atom is missing. In this case, the binding energy of the graphene supercell is scaled to reflect the difference in the number of atoms.

$$E_{defect} = E_{B-doped} - E_{B-Graphene} \quad (3.2)$$

Table 3.1 summarizes the results for the studied systems. It can be observed that even though the phosphorus doped system has a high defect formation energy, it is comparable to the N₃-vacancy formation energy. It is also seen that the PN defect has a lower formation energy (by ca. 0.45 eV) than the single P defect. This means that the heteroatomic PN defect is more stable than the P defect. It is also seen

that other PN-doped systems exhibit a higher formation energy when compared to P or neighboring PN system.

Table 3.1: Total and binding energies for different doped graphene systems, as well as the energy cost associated with the particular defect. All energies are in eV.

System	Total Energy	Binding Energy	Defect Energy
Pristine	-15129.730258	-1027.131790	—
N-doped	-15245.367786	-1026.399814	0.7319760
N ₃ -Vacancy	-15320.030376	-1012.227462 [†]	4.4233914
P-doped	-15152.119902	-1020.494715	6.6370750
PN-doped	-15268.946032	-1020.951341	6.180449
PN ₃ -doped	-15500.969851	-1020.236152	6.895638
PN-2NN	-15268.223483	-1020.228792	6.902998

[†] Graphene binding energy scaled to match the number of atoms.

3.3 P and PN doped Nanotubes

In this section, nanotubes doped with the lowest energy defects, that is, P and PN defects, will be compared to pristine and N-doped nanotubes.

3.3.1 Structural changes of doped Nanotubes

In the nanotube cases, the curved structure helps to reduce the strain needed to accommodate the phosphorus atoms. Here we repeat the representation of a pristine nanotube with a red hexagonal lattice, while the doped nanotube is shown in the ball & stick model. In the zigzag tube of figure 3.3a, the nitrogen doped case is displayed, and it can be seen that similar to the N-doped graphene, the bond lengths around the nitrogen atom are slightly shorter than for a pristine carbon nanotube, being 1.39 Å and 1.41 Å for the axial and diagonal directions, respectively, compared to 1.43 Å and 1.44 Å for the pure carbon case. The nanotube does not have major distortion, as can be concluded from the figure, and there is a small reduction in the nanotube diameter at the defect site (7.97 Å in the defect site *versus* 8.06 Å in

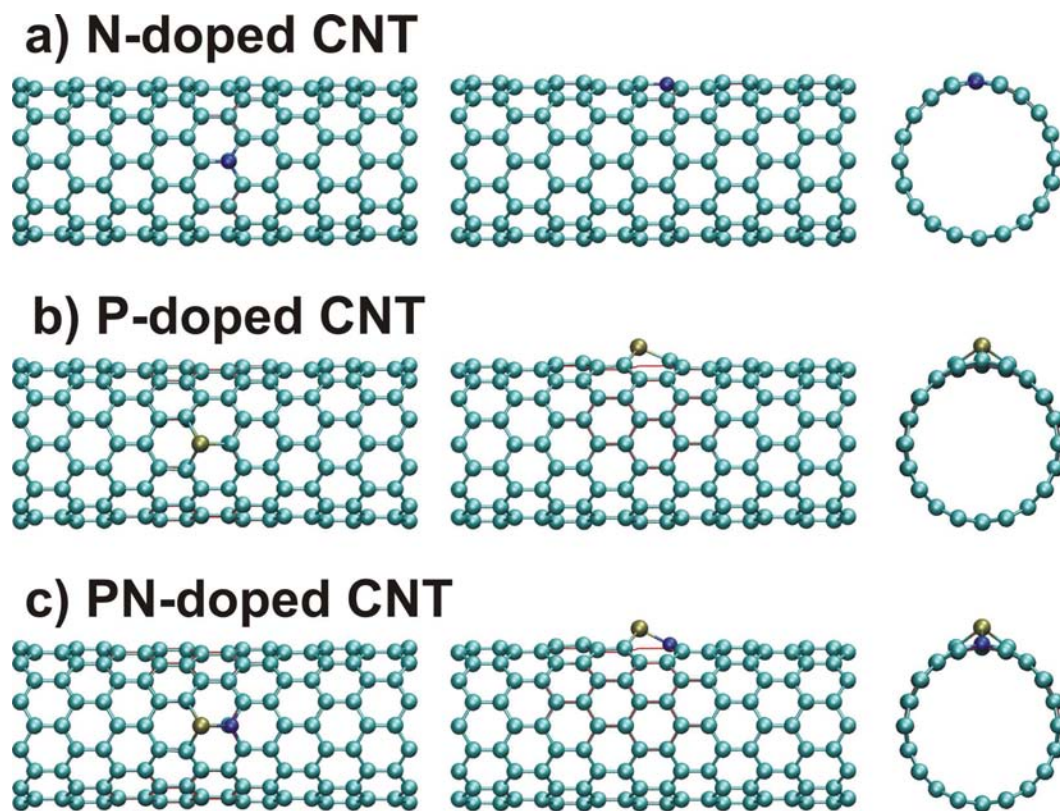


Figure 3.3: Molecular model for zigzag doped carbon nanotubes. a) Substitutional nitrogen; b) substitutional phosphorus; and c) heteroatomic P-N doped nanotube.

the supercell boundary).

For a phosphorus doped (10,0) zigzag nanotube, the defect effects are somewhat different that in a P-doped graphene. The two nonequivalent lengths for a P-C bond are 1.76 Å (axial) and 1.81 Å (diagonal), and it is clear that the phosphorus atom still prefers the sp^3 bonding and that it still uses tetrahedral coordination, but in this case the already curved nanotube structure helps to reduce the strain induced in the hexagonal network to accommodate the phosphorus impurity. It can be observed in figure 3.3 that the distortion of the hexagonal network is almost limited to the first neighbors, with a small displacement for the second neighbors, while the third neighbors are practically unaffected. Also, there is change in the cross-section shape of the nanotube, from circular to slightly oval, with diameters of 7.8 Å (minor) and 8.28 Å (major, measured at the first neighbors of defect). The diameter at the defect site is 8.99 Å, and the phosphorus atom pops out from the nanotube wall.

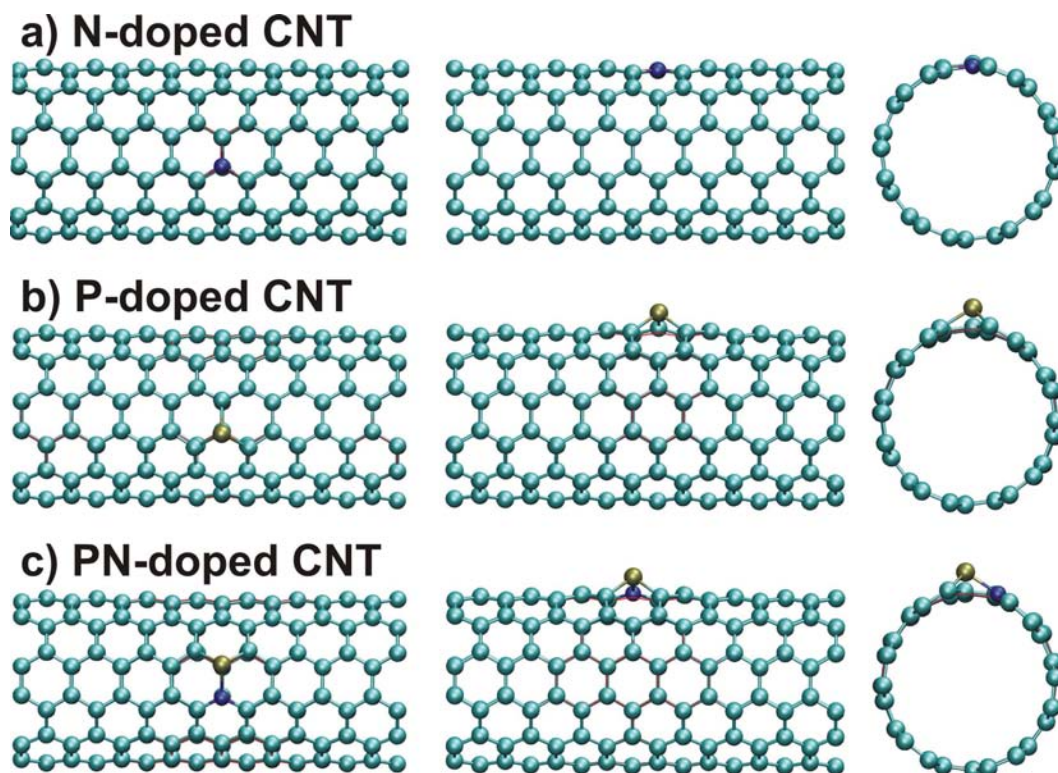


Figure 3.4: Molecular model for armchair doped carbon nanotubes. a) Substitutional nitrogen; b) substitutional phosphorus; and c) heteroatomic P-N doped nanotube.

The PN-doped (10,0) nanotube has very similar features that the P-doped counterpart. The phosphorus also prefers the sp^3 bonding, but the nitrogen helps to reduce the strain in the carbon network. It was observed that while the P atom displacement from its ideal position in the network is increased, the displacement of the surrounding atoms is reduced.

For the metallic armchair (6,6) nanotube shown in figure 3.4a, the structural effects of doping are very similar to that of a zigzag nanotube. In this nanotube, the C-N bonds are again shorter than the C-C bond displayed in pristine nanotubes, being 1.40 Å in both diagonal and tangential directions, compared to 1.43 Å in the pristine nanotube. In this case, the nitrogen atom position is slightly inwards to the nanotube surface, the nanotube diameter in the nitrogen site is 8.20 Å, compared to 8.30 Å in the boundary of the supercell.

For the P-doped (6,6) nanotube from figure 3.4b, the bond lengths are 1.78 Å for the diagonal and 1.82 Å for the tangential bonds, while the angles are still very close

to the 98° that phosphorus has in triphenylphosphine. In the PN case from figure 3.4c, it can be seen that the structure of a PN defect is also very similar to that of the zigzag nanotube; the nitrogen atom helps to reduce the structural strain caused by the phosphorus impurity.

3.3.2 Total Energy calculations for Doped Nanotubes

Total energy and electronic structure calculations were performed for these nanotubes, and the defect formation energies were calculated using equations 3.1 and 3.2, and are summarized in table 3.2. It is noteworthy that the formation energy for P and PN defects is 1 eV and 0.7 eV lower for nanotubes than it is for graphene, respectively. This indicates that curvature helped to reduce the strain in the nanotubes after the phosphorus insertion. It is also important to notice that the difference in energy of P and PN defects was reduced from 0.45 eV in graphene to about 0.15 eV in nanotubes, reflecting also that curvature reduces the strain, and therefore the damping effect of nitrogen on it.

Table 3.2: Total and binding energies for (10,0) and (6,6) nanotube doped systems, as well as the energy cost associated with the particular defect. All energies are in eV.

System	Total Energy	Binding Energy	Defect Energy
Pristine (10,0)	-30853.339593	-2072.526393	—
N-doped (10,0)	-30968.776028	-2071.593324	0.933069
P-doped (10,0)	-30876.813275	-2066.973356	5.553037
PN-doped (10,0)	-30993.323327	-2067.113904	5.412489
Pristine (6,6)	-29620.749096	-1991.168424	—
N-doped (6,6)	-29736.381346	-1990.431170	0.737254
P-doped (6,6)	-29644.197550	-1985.590159	5.578265
PN-doped (6,6)	-29760.735203	-1985.758308	5.410116

3.3.3 Electronic structure

Depending on their particular geometry, pure carbon nanotubes can behave as metals or semiconductors [10, 11], but the presence of dopants creates new states in the electronic structure that modify this behavior. The origin of these states is the different electronic configurations of the doping atoms, that affect their bonding capabilities. For substitutional nitrogen doping, N bonds with an sp^2 hybridization, the same as carbon, with three coplanar bonds. However, nitrogen has five electrons in its valence shell, three of which are used to bond to the carbon network, while the other two electrons are kept in the π -electron system and create a new electronic state that can be seen in figure 3.5 for a zigzag semiconductive nanotube, and figure 3.6 for a metallic armchair nanotube. The state created in semiconductive nanotubes lies beneath the conduction bands, and has one electron (the extra electron from nitrogen), and therefore it shifts the Fermi energy in the nanotube to the conduction bands, causing all N-doped semiconductive nanotubes to be metallic. In the case of metallic nanotubes, the state related to the presence of N appears in the conduction bands, and the extra electron from nitrogen is injected to the conduction bands. As part of the effects, degeneracy is lost and unfolding of the bands can be observed for doped nanotubes.

In the case of phosphorus, it also has five electrons in its valence shell, but it bonds with an sp^3 hybridization, that is, it prefers a tetrahedral coordination, thus creating a localized state in its fourth orbital when bonded to a graphitic network. This localized state appears as a dispersionless state, i.e. a flat band, in the band structure, as seen in figures 3.5 and 3.6. Due to their localized nature, these phosphorus-related states do not contribute with electrons to the conduction bands, and therefore they do not affect the semiconductive or metallic character of the nanotubes. These states are also projected as a sharp peak in the electronic density of states at the Fermi level, as seen in figure 3.7. The splitting in two peaks observed for the P-doped zigzag system correspond to the spin up and spin down configurations.

For PN-doped systems, two states are created symmetrically around the Fermi energy. In semiconducting zigzag nanotubes, these states have a low dispersion and

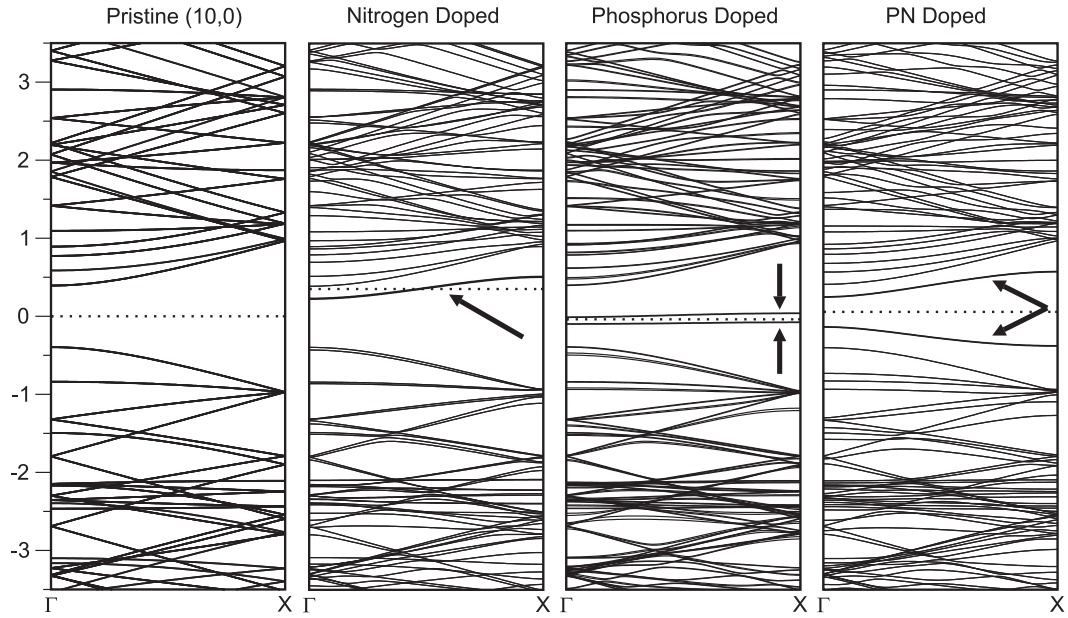


Figure 3.5: Bands structure for zigzag carbon nanotubes. From left to right: pristine (10,0) nanotube, nitrogen doped (10,0), phosphorus doped (10,0) and PN-doped (10,0). The presence of new states is indicated by arrows. The energies are relative to the pure carbon nanotube Fermi level, and the dotted lines are the Fermi level on each system.

reduce the bandgap to half, from ca. 0.8 eV for pristine (10,0) nanotube to ca. 0.38 eV for PN-doped nanotube (figure 3.7). The breaking of symmetries in the nanotube due to the presence of dopants is observed in all cases as band unfolding, and the Van-Hove singularities present in pure carbon nanotubes are lost.

In figure 3.8 we can see a comparison of the wave functions of both nitrogen and phosphorus induced states. The plots correspond to the isosurface with a value of $0.05\text{bohr}^{-3/2}$ evaluated at the Γ k-point. The nitrogen-doped case, corresponds to the wavefunction of the bottom conduction band, which shows a high hybridization with the nitrogen orbitals. For the phosphorus case, the plot corresponds to the half-filled flat band localized at the Fermi Energy. It can be seen by the degree of localization and the flat band state that this electron is strongly bounded to the phosphorus atom. For the PN-doped case, we have two states arising from the doping atoms, the top valence and the bottom conduction bands. The first state has a strong localization (although not as much as the phosphorus doped case), while the second state has a better mixing with the π -electron system of the carbon

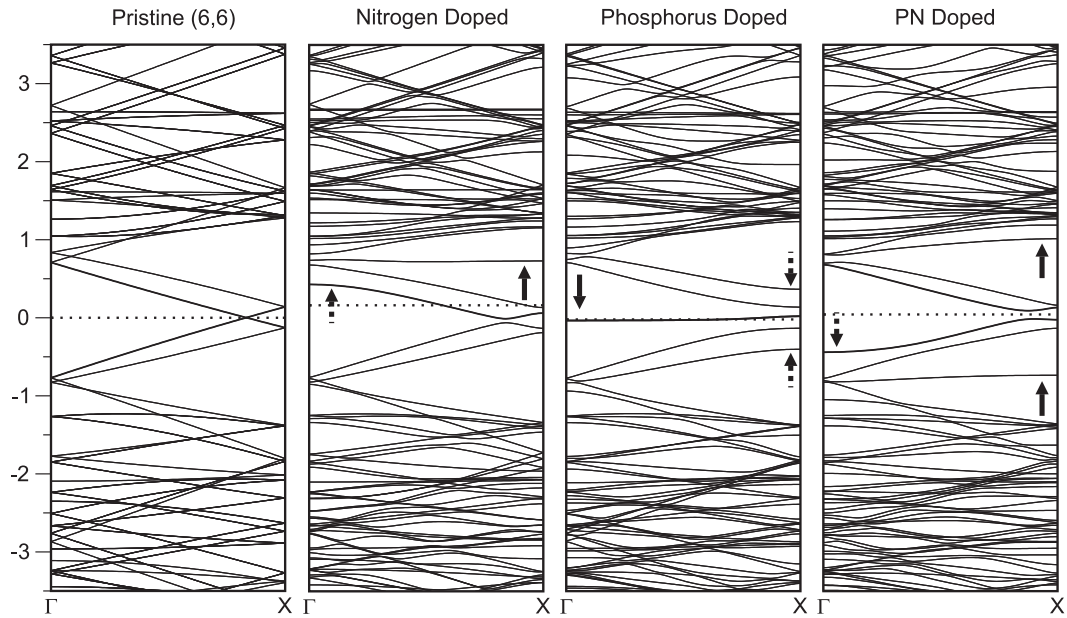


Figure 3.6: Bands structure for armchair carbon nanotubes. From left to right: pristine (6,6) nanotube, nitrogen doped (6,6), phosphorus doped (6,6) and PN-doped (6,6). The presence of new states is shown by arrows. The energies are relative to the pure carbon nanotube Fermi level, and the dotted lines are the Fermi level on each system.

network.

3.4 Transport Properties

The use of the Surface Green function matching (SGFM) method allows to treat the doping problem in a more realistic way: instead of having a defect in a large periodic supercell, it enables us to have a single doping site in an infinite nanotube, by connecting a doped finite nanotube with semi-infinite leads that are otherwise perfect pristine nanotubes. By using this method described by Nardelli [9], we studied the effects in the transport properties of a single doping atom in a carbon nanotube.

The effects of the nitrogen atoms in the electron transport properties were consistent with previous reports [12], that is, there is a reduction of the conductance for energies close to those of the quasibound states associated with the nitrogen atom, slightly above the Fermi Energy, at 0.69 eV, and a second one right before the first

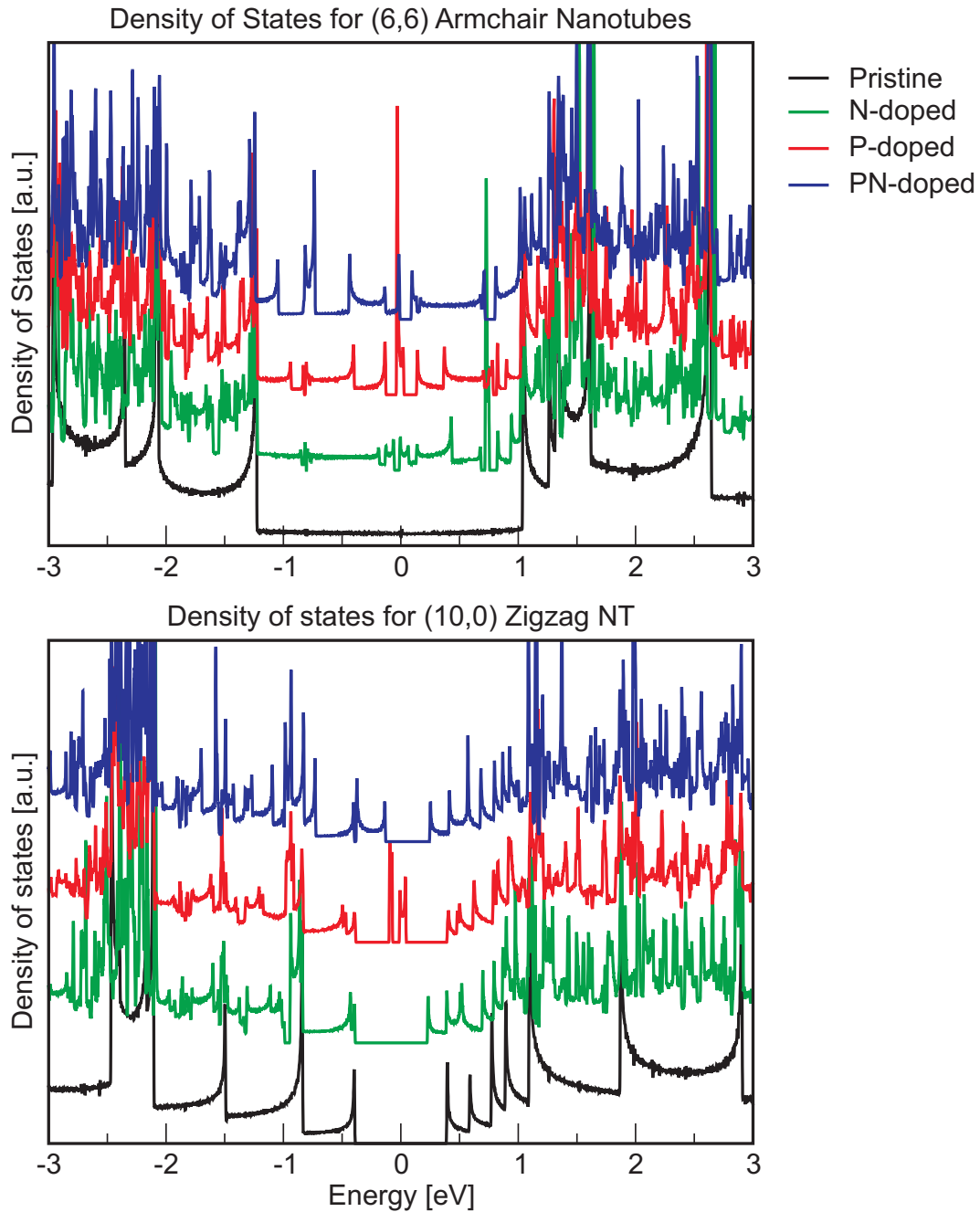


Figure 3.7: Density of states for (6,6) armchair nanotubes (top) and (10,0) zigzag nanotubes (bottom). The reference Energy is the Fermi level for pristine nanotubes.

Van Hove singularity, at 1.03 eV, as seen in figure 3.9. This is explained by the difference in scattering for the incoming wave function components when the nanotube symmetry is broken by the nitrogen atom. For the zigzag nitrogen doped nanotube, the shift in the Fermi energy to the bottom of the conduction bands caused that the nanotubes behave as a *n*-type semiconductor, with a non-zero conductance for very

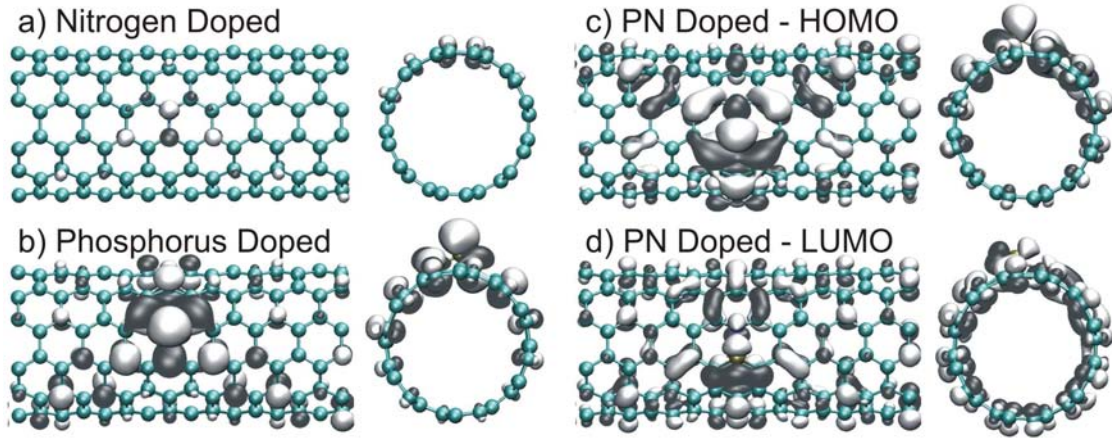


Figure 3.8: Plots of the wavefunctions for localized states around the defect sites for nitrogen, phosphorus and phosphorus-nitrogen doped (6,6) nanotubes. It can be seen that in the phosphorus-doped case, the state is highly localized around the phosphorus atom, while in the PN-doped case, the localization is higher for the top valence band, although in the bottom conduction band there is still some localization around PN defect.

small positive energies and no conductance for negative energies.

For the armchair phosphorus doped nanotube (figure 3.10, the highly localized state in the Fermi energy behaves as a scatterer, and the conductance of the nanotube is reduced from 2 to 1 G_0 , similar to the case of nitrogen quasibound states. In this case, the symmetry is also lost after the insertion of the phosphorus atom.

The PN-doped nanotube has two states that arise from the phosphorus and nitrogen atom bonding to the nanotube, one on each side of the Fermi level. These states are also reflected as valleys in the conductance, as shown in figure 3.11, located at -0.7 eV and 0.98 eV.

The conductance for the phosphorus- and phosphorus nitrogen-doped zigzag nanotubes was not affected by the localized states in the vicinity of the Fermi level, as seen on figures 3.10 and 3.11. In other words, the zigzag semiconductive nanotubes remain as such, with some changes for energies higher than 1.2 eV, probably due to the loss of symmetry in higher energy bands.

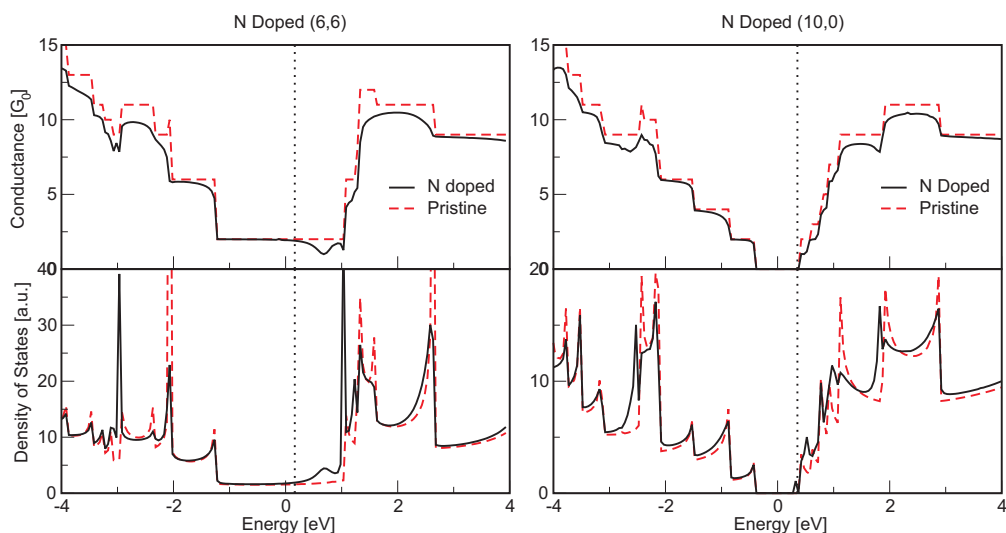


Figure 3.9: Calculated conductance of nitrogen-doped (6,6) (left) and (10,0) (right) carbon nanotubes, compared to the pristine nanotube conductance, in dashed red line (top). Electronic density of states (DOS) for the above mentioned nanotubes, compared to the pristine nanotube DOS, shown in dashed red line (bottom). It can be observed that for the armchair nanotube, the states created by the extra nitrogen electron (shown as peaks in the DOS) cause two reductions in the nanotube conductance when compared to pristine nanotubes, similar to the results of Choi et al. [12].

3.5 Oxidation of phosphorus doped carbon nanotubes

Carbon nanotube surface, similar to graphene, is highly inert due to a saturated π -electron network. In order to be chemically active, carbon nanotubes have to undergo a functionalization process that inserts defects and chemical radicals in carbon nanotube surface, such as dangling bonds, carboxyl and carbonyl radicals, among others. Doped carbon nanotubes, instead, have chemically active sites in those sites affected by the doping atoms. These can be due to a disruption of the π -electron network or to the presence of localized states around the doping atoms, as seen on section 3.3.3. These active sites can be used to anchor molecules and chemical radicals into the nanotube surface.

The use of nitrogen doped nanotubes has been previously reported to anchor metal particles [13, 14], and proteins [15], among others. As it was shown on section

3.3.3, the localized states in phosphorus and phosphorus-nitrogen doped nanotubes are very similar to the highest occupied molecular orbital (HOMO) level in triphenylphosphine.

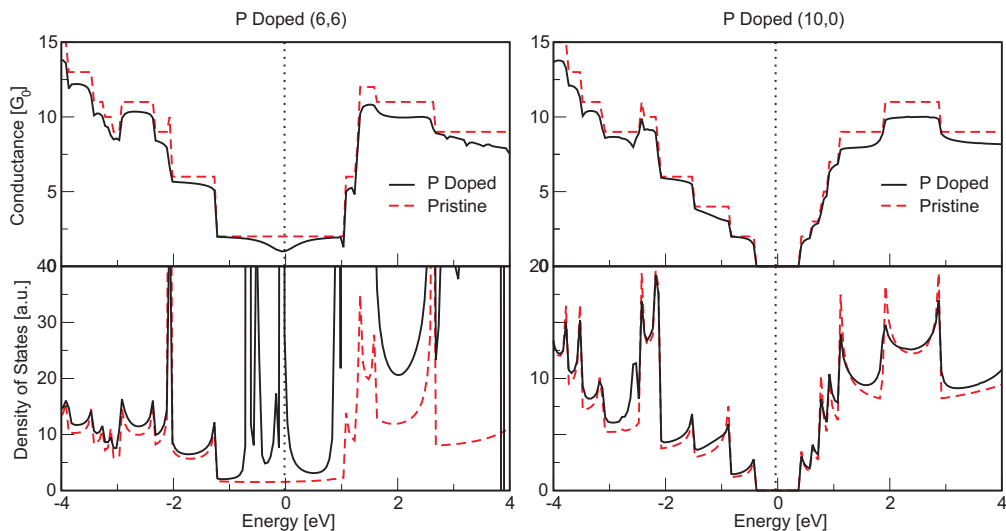


Figure 3.10: Calculated conductance of phosphorus doped (6,6) (left) and (10,0) (right) carbon nanotubes, compared to the pristine nanotube conductance, in dashed red line (top). Calculated density of states (DOS) for the above mentioned nanotubes, compared to the pristine nanotube DOS, shown in dashed red line (bottom).

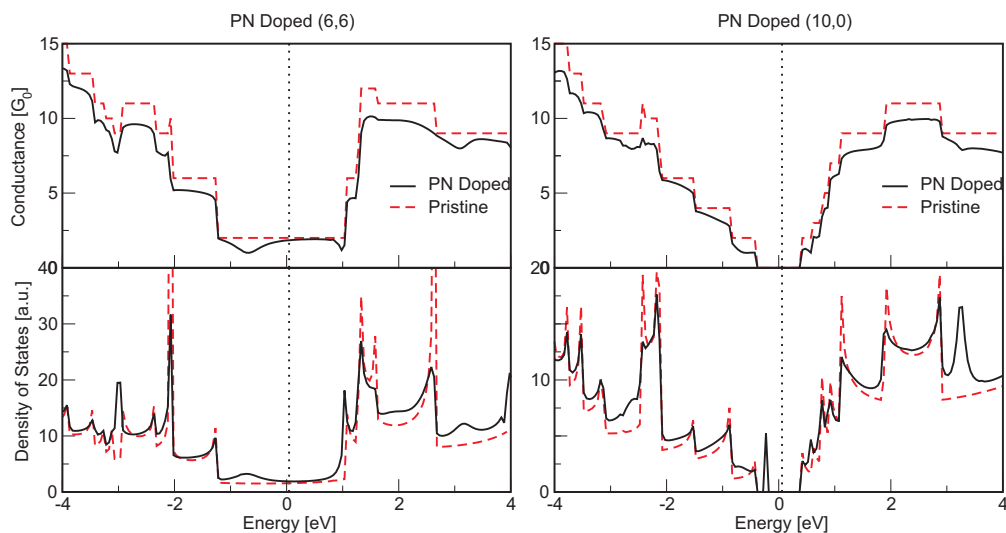


Figure 3.11: Calculated conductance of phosphorus-nitrogen doped (6,6) (left) and (10,0) (right) carbon nanotubes, compared to the pristine nanotube conductance, in dashed red line (top). Calculated density of states (DOS) for the above mentioned nanotubes, compared to the pristine nanotube DOS, shown in dashed red line (bottom).

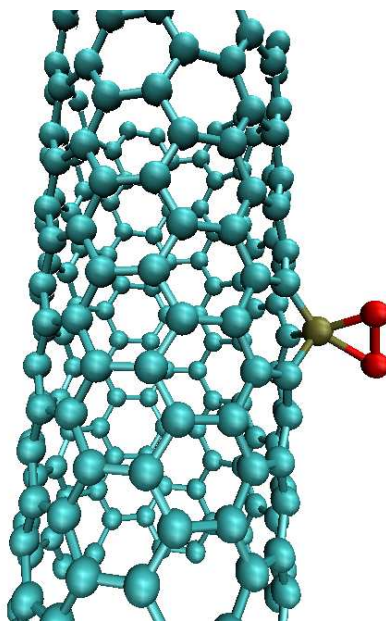


Figure 3.12: Oxidation of a (6,6) P-doped carbon nanotube. It is observed that oxygen atoms bond to the fourth orbital of the phosphorus atom.

Based on the triphenylphosphine known reactions, the oxidation process for P and PN doped nanotubes was explored by means of *ab initio* molecular dynamics using the Vienna *ab initio* simulation package (VASP) version 4.6.6 [16–19], which implements the density functional theory [2, 3] using the augmented plane wave approach [20, 21]. The generalized gradient approximation (GGA) exchange correlation functional of Perdew, Burke and Ernzhof (PBE) was used [22]. The system was restricted to 5 unit cells of a (6,6) doped nanotube and a single oxygen molecule (O_2) located about 2 Å away from the defect site, for a total of 122 atoms. The effects of temperature in the oxidation is analyzed using a Nosé-Hoover thermostat [23], for a 1 ps period with an integration step of 1 fs, and the ions are thermalized to 800 K. Finally, the effects of the oxidation of P and PN doped nanotubes in the electron transport properties was also explored.

Figure 3.12 displays a phosphorus doped nanotube subject to oxidation by a O_2 molecule after 1 ps of simulation. The two oxygen atoms are now bonded to the phosphorus atom, with bond lengths of 1.63 and 1.74 Å, and a O-O bond of 1.55 Å. These atoms migrate to the phosphorus vicinity right after the beginning of the simulation and do not leave this position for the rest of the time. The bonding of the

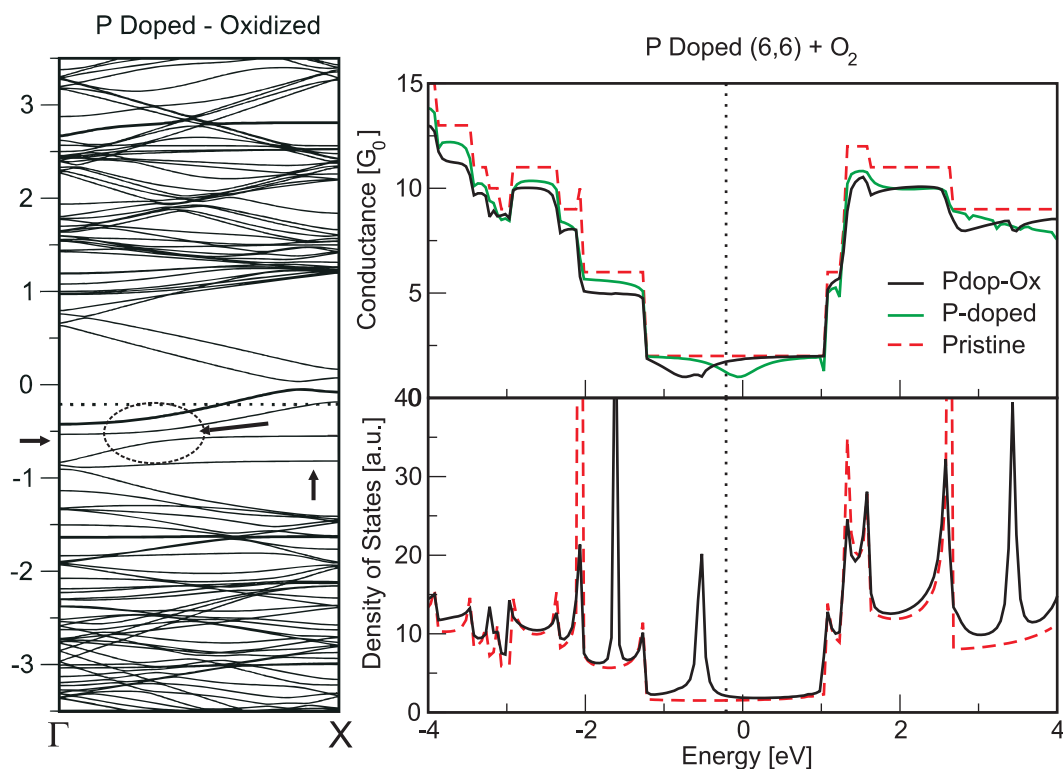


Figure 3.13: Band structure of an oxidized (6,6) P-doped nanotube and calculated conductance of the same nanotube, compared to an unoxidized P-doped nanotube and a pristine nanotube

oxygen atoms to the nanotube is reflected in the band structure, and the localized state located at the Fermi energy shifts to lower energies. Also, the appearance of several flat-band states in the energy bands diagram seem to be related with molecular-like orbitals in the oxygen atoms. One of the most visible effects of the oxidation of the P-doped nanotube is the change in the quantum conductance, as seen in figure 3.13. The shift in the energy of the localized state of the phosphorus also causes that the reduction in the conductance of the oxidized nanotube occurs at lower energies, and therefore this change in the conductance could be detected by an electric current.

The Energy shift in the valley of conductance after the oxidation of the phosphorus atom could be used in an electric circuit to monitor these changes, and new kind of molecules could be detected based on the response of the nanotube to the different chemical environments of the phosphorus atom. These would lead to new phosphorus-doped carbon nanotube based sensors.

3.6 Conclusions

In this chapter, it was shown that both phosphorus and heteroatomic phosphorus-nitrogen doped carbon nanotubes are feasible and confirmed the experimental section of this thesis, where PN-doped multiwalled carbon nanotubes were synthesized. The estimation of the defect formation energy showed that, although they have a high formation energy, ca. 5 eV for one defect in 200 atoms (0.5%), it is comparable to a pyridinic N_3 defect, and therefore it is feasible. This is consistent with the experimental hypothesis presented in chapter 2.

Analysis of the relaxed structures confirms that phosphorus keeps the sp^3 hybridization, and bonds to the carbon network with tetrahedral orbitals, inducing structural strain in the carbon network in order to accommodate the longer P-C bonds and the larger P ion. Total energy calculations confirmed that curvature helps to reduce the structural strain caused by the phosphorus, and that the P-N defect is energetically more stable than phosphorus alone.

After calculating the band structure, it was observed the presence of localized (P) and semilocalized (PN) states around dopant atoms. In contrast to nitrogen, these states do not modify the intrinsic nanotube metallicity, and therefore semiconducting nanotubes remain the same regardless of the doping.

Electronic transport calculations on pristine, nitrogen, phosphorus and P-N doped nanotubes helped to understand the different effects of the dopant in their conductance. The calculation of the quantum conductance showed that zigzag phosphorus doped nanotubes do not modify their intrinsic semiconductive behavior. It was observed that while nitrogen doping in semiconducting nanotubes effectively shifts the Fermi energy to the conduction bands and makes N-doped semiconductive nanotubes to behave as a n-type semiconductor.

Phosphorus and PN doping in a (10,0) nanotube only create bound and semi-bound states around the phosphorus atom, that are almost dispersionless (represented by a flat band in the band diagram), and that are reflected as a sharp peak in the density of states. These states do not contribute to the electronic transport, and in the case of a metallic nanotube, these states behave as scatterers that create valleys in the conductance.

Molecular dynamics simulation of the oxidation process for phosphorus doped nanotubes showed that phosphorus atom readily changed its oxidation state from 3 to 5, bonding to oxygen atoms. After being oxidized, the quasibound state shifts its energy relative to the Fermi level, and this change is observed in the quantum conductance of the oxidized nanotube when compared to the P-doped nanotube. These nanotubes can be used as sensors to monitor the chemical state of the doping atom using a probe current, and its changes in the oxidation state can be used to develop new kinds of gas and molecule detectors.

References

- [1] J. M. Soler, E. Artacho, J. D. Gale, A. García, J. Junquera, P. Ordejón, and D. Sánchez-Portal. The siesta method for ab-initio order-N materials simulation. *Journal of Physics: Condensed Matter*, 14:2745–2779, 2002.
- [2] P. Hohenber and W. Kohn. Inhomogeneous electron gas. *Physical Review*, 136: B864–B871, 1964.
- [3] W. Kohn and L. J. Sham. Self-consistent equations including exchange and correlation effects. *Physical Review*, 140:A1133–A1138, 1965.
- [4] J. Junquera, O. Paz, D. Sánchez-Portal, and E. Artacho. Numerical atomic orbitals for linear-scaling calculations. *Physical Review B*, 64(23):235111, Nov 2001. doi: 10.1103/PhysRevB.64.235111.
- [5] D. M. Ceperley and B. J. Alder. Ground state of the electron gas by a stochastic method. *Physical Review Letters*, 45:566–569, 1980.
- [6] J.P. Perdew and A. Zunger. Self-interaction correction to density-functional approximations for many-electron systems. *Physical Review B*, 23:5048, 1981.
- [7] N. Troullier and J. L. Martins. Efficient pseudopotentials for plane-wave calculations. *Physical Review B*, 43:1993–2006, 1991.
- [8] L. Kleinman and D. M. Bylander. Efficacious form for model pseudopotentials. *Physical Review Letters*, 48:1425–1428, 1982.
- [9] M.B. Nardelli. Electronic transport in extended systems: Application to carbon nanotubes. *Physical Review B*, 60:7828–7833, 1999.
- [10] R. Saito, M. Fujita, G. Dresselhaus, and M. S. Dresselhaus. Electronic structure of graphene tubules based on c60. *Physical Review B*, 46:1804–1811, July 1992.
- [11] N. Hamada, S. Sawada, and A. Oshiyama. New one-dimensional conductors: Graphitic microtubules. *Physical Review Letters*, 68(10):1579–1581, March 1992.

- [12] H.J. Choi, J Ihm, S.G. Louie, and M.L. Cohen. Defects, quasibound states, and quantum conductance in metallic carbon nanotubes. *Physical Review Letters*, 84:2917–2920, 2000.
- [13] A. Zamudio, A.L. Elias, J.A. Rodriguez-Manzo, F. López-Urías, G. Rodríguez-Gattorno, F. Lupo, M. Rühle, D.J. Smith, H. Terrones, D. Díaz, and M. Terrones. Efficient anchoring of silver nanoparticles on N-doped carbon nanotubes. *Small*, 2:346–350, 2005.
- [14] K. Jiang, A. Eitan, L.S. Schadler, P.M. Ajayan, R.W. Siegel, N. Grobert, M. Mayne, M. Reyes-Reyes, H. Terrones, and M. Terrones. Selective attachment of gold nanoparticles to nitrogen-doped carbon nanotubes. *Nano Letters*, 3:275–277, 2003.
- [15] K. Jiang, L.S. Schadler, R.W. Siegel, X. Zhang, H. Zhang, and M. Terrones. Protein immobilization on carbon nanotubes via a two-step process of diimide-activated amidation. *Journal of Materials Chemistry*, 14:37–39, 2004.
- [16] G. Kresse and J. Hafner. Ab initio molecular dynamics for liquid metals. *Physical Review B*, 47:558–561, 1993.
- [17] G. Kresse and J. Hafner. Ab initio molecular dynamics simulation of the liquid-metal-amorphous-semiconductor transition in germanium. *Physical Review B*, 49:14251–14269, 1994.
- [18] G. Kresse and J. Furthmuller. Efficiency of ab initio total energy calculations for metals and semiconductors using a plane-wave basis set. *Comput.Mater.Sci*, 6:15–50, 1996.
- [19] G. Kresse and J. Furthmuller. Efficient iterative schemes for ab initio total energy calculations using a plane-wave basis set. *Physical Review B*, 54:11169–11186, 1996.
- [20] P.E. Blochl. Projector augmented-wave method. *Physical Review B*, 50:17953–17979, 1994.

-
- [21] G. Kresse and D. Joubert. From ultrasoft pseudopotentials to projector augmented wave methods. *Physical Review B*, 59:1758–1775, 1999.
- [22] J.P. Perdew, K. Burke, and M. Ernzerhof. Generalized gradient approximation made simple. *Physical Review Letters*, 77:3865–3868, 1996.
- [23] S.A. Nosé. Unified formulation of the constant temperature molecular dynamics method. *Journal of Chemical Physics*, 81:511–519, 1994.

Chapter 4

Boron Nitride nanoribbons

In this chapter, the energetic stability of boron nitride nanostructures and their electronic structure will be reviewed, and the effect of boron nitride domains in carbon / boron nitride nanotube heterojunctions will also be studied. Recent experimental developments that suggest the existence of metallic domains in boron nitride nanostructures will be reviewed, and a model of boron nitride nanoribbons with exposed edges is proposed to explain this unusual behavior. Finally, and from the theoretical standpoint, the presence of metallic boron nitride states in zigzag nanoribbons with exposed edges will be explained.

4.1 Introduction

Boron Nitride is a wide band gap semiconductor in its bulk phases. It is a very versatile material because it shares all the structural geometries of carbon allotropes, that is, there is an analogous crystal structure of boron nitride for all the carbon allotropes. In this sense, cubic Boron Nitride (c-BN), analogue to diamond (see figure 4.1b), is also a very hard material, with the advantage of being chemically inert and resistant to oxidizing environments. In a similar way, wurtzite-like BN (w-BN) is analogue to the graphite phase called “buckled graphite”, and this phase occurs only under high pressure.

Hexagonal boron nitride (h-BN) has a very similar structure to graphite, being the only difference the stacking of the hexagonal layers, (figure 4.1a). As a layered

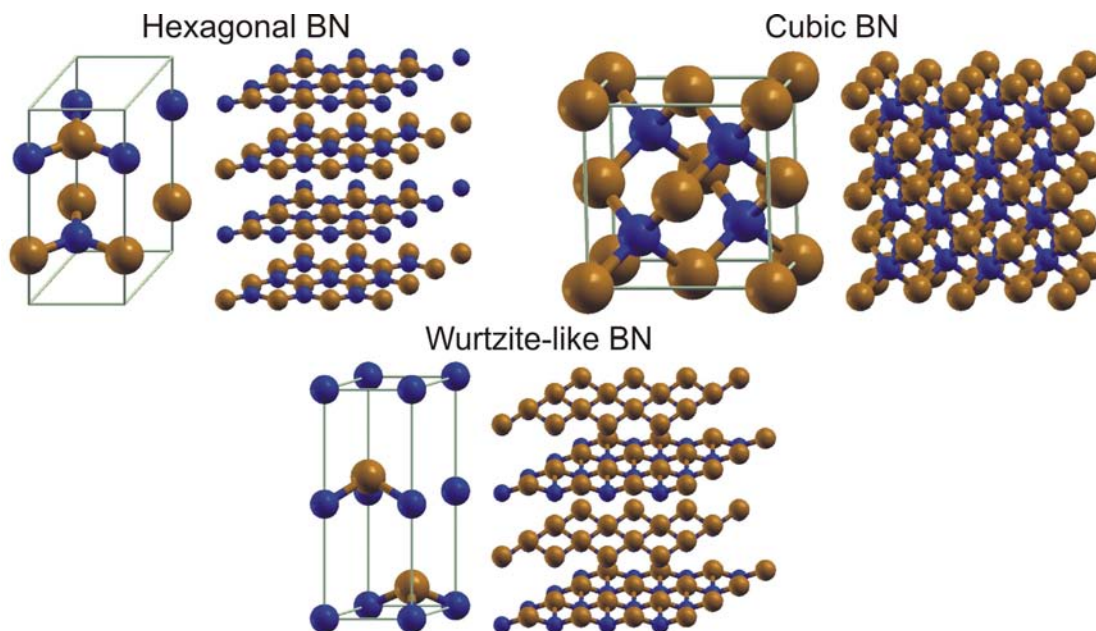


Figure 4.1: Structural models of boron nitride allotropes. The hexagonal phase (top left) is structurally similar to graphite, while the cubic phase (top right) exhibits a structure similar to diamond. The wurtzite-like structure (bottom) is a high pressure phase that corresponds to the corrugated or “buckled graphite” structure.

material with weak interlayer coupling, and similar to graphite, h-BN is an excellent solid lubricant, with the advantage of having a higher temperature resistance in oxidizing environments, and hence is sometimes called “white graphite”.

However, opposite to graphite, h-BN is a wide band gap semiconductor (5.5 eV), or in other words, an insulator. While Boron nitride is isoelectronic with graphite, the high difference in electronegativity between nitrogen and boron causes a polarization of the chemical bond, which results in a splitting of the π and π^* and a high energy for the fundamental excitation (figure 4.2).

4.2 Boron nitride nanostructures

The Boron Nitride (BN) Nanotubes were first proposed by Rubio et al. [1] in 1994, shortly after the identification of Carbon Nanotubes by Iijima [2], and based on the structural similarities between graphite and hexagonal Boron Nitride (h-BN). Since h-BN is a wide-gap semiconductor, it would be expected that the electronic

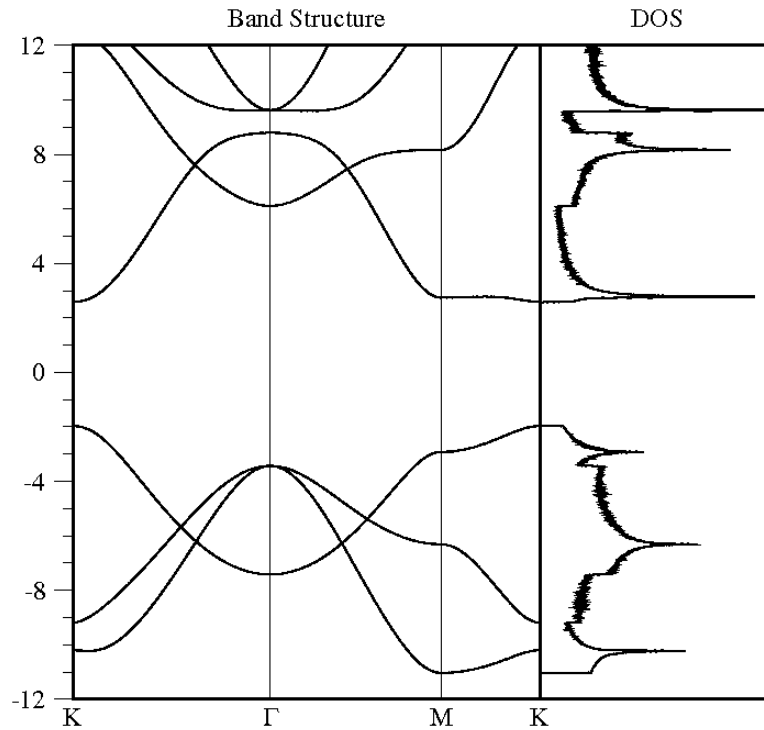


Figure 4.2: Band structure (left) and density of states (right) for a single layer of hexagonal Boron Nitride, showing that the material is an insulator with a calculated band gap of ca. 4.5 eV. Notice that this local density approximation underestimates the energy gap, and that other studies using the quasiparticle approximation reveal a band gap of 6.0 eV for this system.

properties for these tubes should be different to their carbon counterparts, i.e., they would be semiconducting regardless of chirality, while still retaining the mechanical properties that make nanotubes attractive. The authors calculated an energy gap for h-BN of 4eV, which is experimentally known to be 5.8eV, using a Slater-Koster tight binding Hamiltonian with second neighbor interactions, with parameters fitted to reproduce the band structure from density functional theory (DFT) within the local density approximation (LDA).

It was also found that for very narrow nanotubes the energy gap was dependant on the nanotube radius, around 1 eV for small nanotubes and close to the bulk value when the radii were large enough [(10,0) or (7,5)]. This was explained in terms of the hybridization caused by the strain on the narrow diameter tubes. In a later report, Blase et al. [3] used DFT quasi-particle calculations to correct the energy

gap for the BN nanotubes, and reported a value of 5.5 eV. These authors also found that the energy gap is nearly independent of the nanotube chirality and number of nanotube walls.

After a structural relaxation, it was found that the mean radius for nitrogen atoms is slightly larger than for Boron atoms, resulting in rotated bonds [3]. In addition, pentagon-heptagon defects are unstable in BN tubes due to a bond frustration effect that implies a B-B or a N-N bond, which would have a high energy cost [4].

Following the theoretical prediction, scientists started to synthesize boron nitride nanotubes and nanostructures experimentally. In 1995, Chopra et al. [5] reported the successful synthesis of multiwalled BN nanotubes by arcing a tungsten electrode filled with h-BN powder as anode, with a copper electrode as cathode. The synthesized nanotubes had an interlayer separation of 3.3 Å, which is consistent with the interplanar distance of bulk h-BN. Subsequently, in 1996, Loiseau et al. [6] reported the production of single and double walled BN nanotubes by arcing HfB₂ electrodes in a nitrogen atmosphere. The nanotubes obtained displayed closed square caps in multiwalled nanotubes and amorphous closure for single walled nanotubes. Simultaneously, Terrones et al. [7] reported the formation of boron nitride nanotubes by arcing Ta-BN electrodes under a nitrogen atmosphere. In this case the nanotube caps had both metal particles and / or square morphologies.

Besides arc discharge, boron nitride nanotubes have been successfully synthesized by several techniques, including laser ablation [8, 9], substitution reactions that use carbon nanostructures as templates [10, 11], chemical vapor deposition of boron and nitrogen containing precursors [12, 13], and mechanical milling of boron nitride powders [14–16], among others.

4.3 Heterostructured Boron Nitride/Carbon Nanotubes

It has been found experimentally that doped carbon nanotubes may experience the segregation of dopants, creating doped and undoped domains [17]. The idea of BN

/ C heterostructured nanotubes was explored early by Blase et al. [18] using DFT within the LDA approximation. The authors estimated the formation energy of the C/BN interfaces to be around 0.4eV per interface bond. They also studied the interdiffusion process in a C/BN interface, finding that it would have an energy cost close to 2.0eV per atom, making it very unlikely and favoring abrupt interfaces.

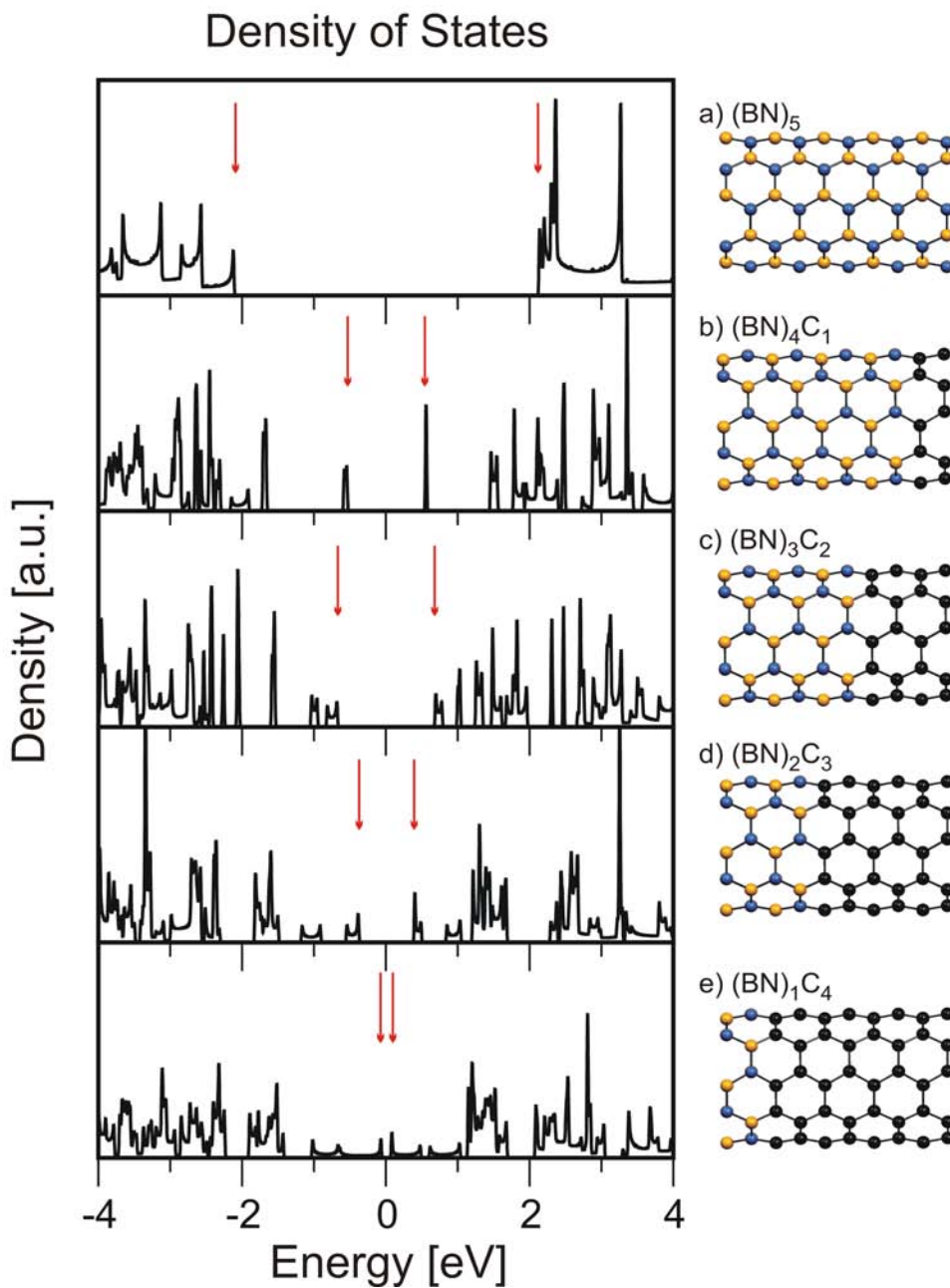


Figure 4.3: Densities of electronic states for heterostructured boron nitride / carbon (5,5) nanotubes with different compositions. It can be seen that the energy gap can be tuned depending on the composition of B, C and N within the nanotube.

Later, Meunier et al. [19] studied zigzag BN/C heterojunctions with different indices, showing that the spontaneous polarization fields could enhance the field emission properties. They found a local field enhancement factor close to 2.1, along with a work function reduction of 1.4eV that resulted into an emission current increase of about two orders of magnitude as compared to a pure carbon system.

Heterostructured nanotubes can also exhibit properties that are intermediate between those of their pure counterparts. A heterojunction between a metallic carbon nanotube and a BN nanotube have different properties depending on the relative composition of the structure. In figure 4.3, different heterojunctions for a (5,5) nanotube, from (BN) C_4 to a pure BN nanotube are depicted. The densities of states have been calculated using the local density approximation[20, 21] to density functional theory [22, 23] and norm-conserving pseudopotentials [24, 25] implemented in the SIESTA code[26, 27]. As the BN content is increased in the system, the energy gap increases from 0.15 eV to 4.2 eV. These results are consistent with previous reports on supercell geometries for C / BN nanotube heterojunctions reported by Choi et al. [28]. In a recent work, Guo et al. [29] describe the synthesis of C / BN multiwalled nanotube heterojunctions using a two-stage hot filament chemical vapor deposition (HFCVD) experiment with varying flows for the carbon, boron and nitrogen sources under a polycrystalline nickel substrate. Therefore, this kind of heterostructures could be synthesized in a controlled way in the near future.

4.4 Could boron nitride be metallic?

Recently, a new kind of boron nitride nanostructure was synthesized by a substitution reaction in nanoporous carbon structures, yielding porous boron nitride nanospheres that resemble sea-urchins [30]. While bulk Boron Nitride is a well known insulator, this new material had a very low turn-on voltage during electronic field emission (1.1 – 1.3 eV/ μm), a value that is opposite to polycrystalline BN films (ca. 8.3 eV/ μm)[31], and similar to carbon nanotube field emission values (1 – 3 eV/ μm)[32].

The synthesis of these sea-urchins involved a substitution reaction of porous

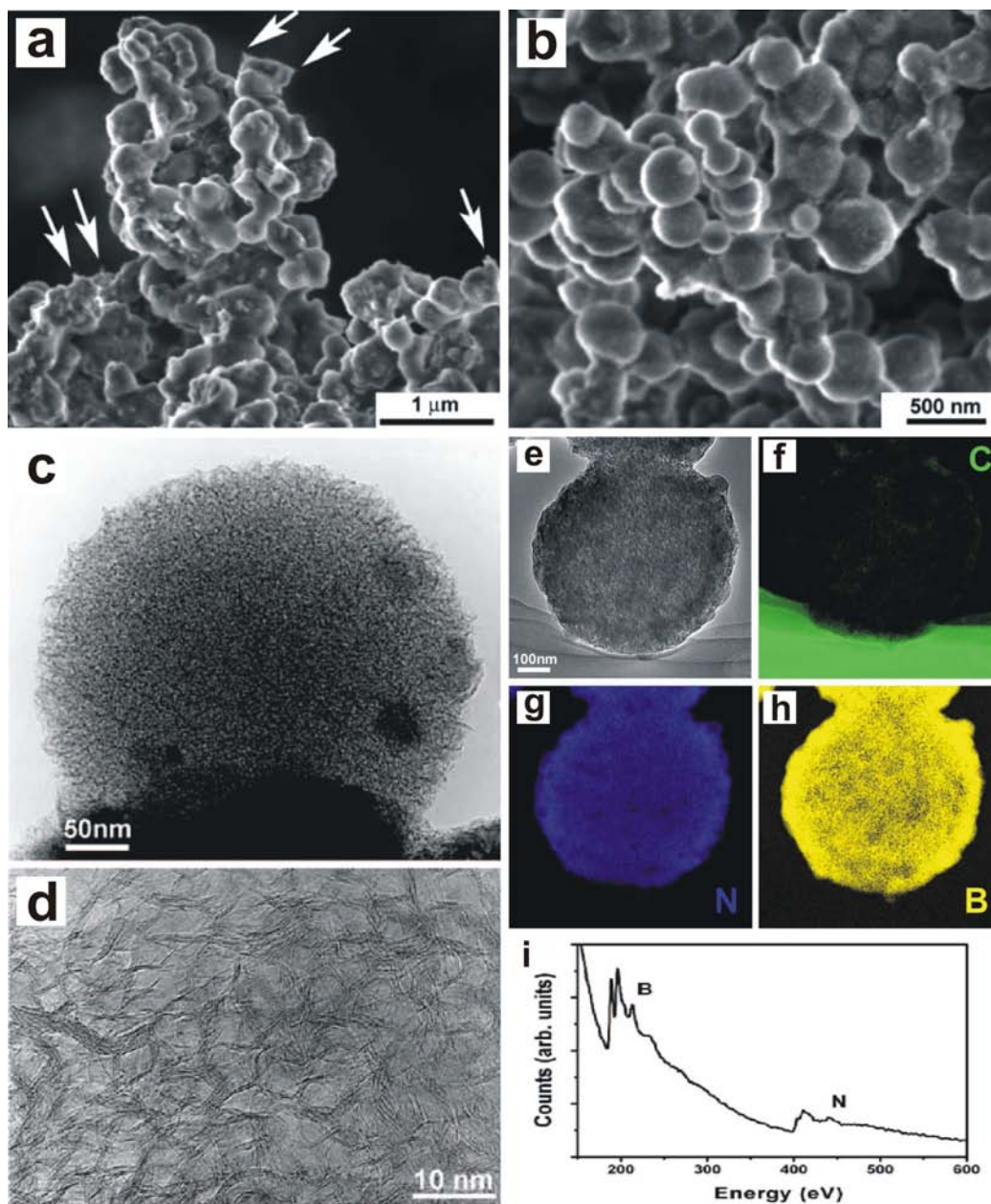


Figure 4.4: Boron Nitride nanospheres resembling sea urchin morphologies. a,b) SEM images displaying the morphology of the synthesized nanospheres. The arrows in a) show small peaks in the sphere surface. c,d) TEM images displaying the porous morphology of the nanospheres. It can be seen in d) that the spheres are composed of multiple ribbon like structures e) to h) Elemental map for a BN nanosphere, confirming that the substitution reaction was complete and the sphere is composed only of boron nitride. i) EEL spectrum clearly displaying the boron and nitrogen edges, while carbon edge is not visible.

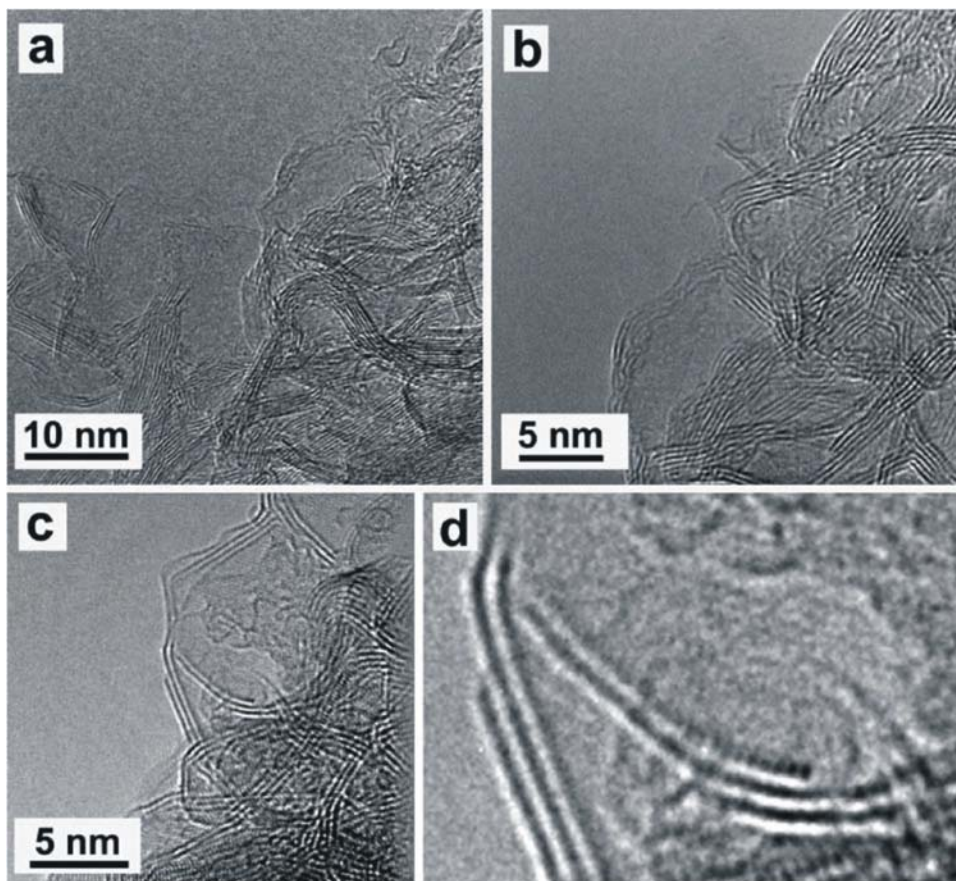


Figure 4.5: HRTEM images of the surface of a BN nanourchin. It can be seen that BN layers protrude from the surface with exposed edges. The image shown in d) has a higher magnification and displays the hexagonal pattern of BN.

carbon nanospheres with boron oxide (B_2O_3) powder under a nitrogen (N_2) flow at $1700^\circ C$ inside a high frequency induction furnace [33].

Scanning electron microscope (SEM) images of the samples reveal uniform agglomerated spherical spheres of 100 to 400 nm of diameter (figure 4.4a,b). TEM images (figure 4.4c,d) show a porous corrugated structure with protruding ribbons and edges on the sphere surface. Energy filtered images (figure 4.4e to f) display that the nanospheres are composed mainly of boron and nitrogen, with only residual traces of carbon, confirming also a high efficiency in the $C \rightarrow BN$ substitution reaction, as previously demonstrated by Golberg et al. [34]. From the EEL spectra depicted in figure 4.4i, it can be confirmed that only boron and nitrogen are present within the sample.

Further HRTEM analysis on the surface of the nanospheres, (figure 4.5) reveal

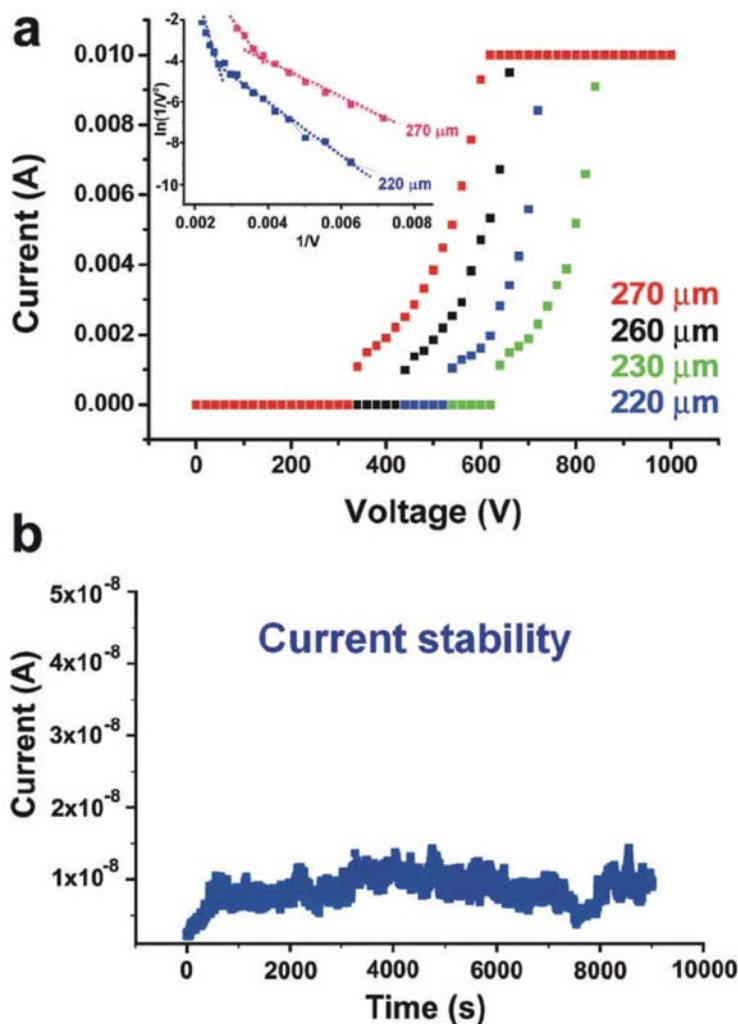


Figure 4.6: a) Field emission I-V curves for BN nanospheres films. The inset shows the Fowler-Nordheim for the I-V curves obtained at 220 μm and 270 μm . b) Current stability of the BN nanourchin films, showing a relative stability for periods over 9000 s.

the presence of stacked and open ribbons consisting of layered materials. These layered material is responsible for the corrugated structure of the nanourchins. It is possible that these exposed BN edges are hydrogen terminated. In addition to the edges, open and closed BN cones were also observed.

One of the most surprising characteristics of these new boron nitride nanospheres is their bulk field emission characteristics, measured from macroscopic films of these corrugated BN nanospheres, and shown in figure 4.6. The nanosphere film - anode distance varied between 220 and 270 μm at steps of 10 μm , while the anode was biased up to 1100V during the recording of I-V curves.

The I-V curves displayed low *turn-on* fields, ranging from 1.1 to 1.3 eV/ μm , as shown in figure 4.6a. This result is striking since being boron nitride an insulator, emission was achieved only for high voltages in the range of 8.3 – 15.2 eV/ μm [31]. The obtained results are comparable with those of carbon nanotube field emitting films (1 – 3 eV/ μm)[32]. From this data, it was proposed that field emission is occurring on open BN edges and protuberances present on the surface of the nanospheres. It is also noted that the emission current became more stable a few seconds after applying the bias voltage. This could be explained by current induced desorption in the BN edges of foreign species like hydrogen, nitrogen and oxygen, that otherwise would inhibit electron emission.

4.4.1 Ab initio calculations of Boron nitride nanoribbons

The unusual field emission of the boron nitride nanourchins at low voltages, as well as its high current stability, suggest that there might be metallic domains in this material. Based on the experimental evidence and in order to clarify the existence of metallic edges, the electronic properties of hexagonal boron nitride nanoribbons exhibiting zigzag and armchair edges with and without hydrogen termination were studied using the SIESTA code [26]. This code performs a fully self-consistent density functional theory (DFT) calculation by solving the standard Kohn-Sham (KS) equations[22, 23]. The KS orbitals are represented by a linear combination of pseudo-atomic orbitals. The core electrons were replaced by nonlocal norm-conserving pseudopotentials [24] in the Kleinman-Bylander factorized form [25]. A double-zeta singly polarized quality basis set [27] is employed in all calculations to represent the valence wave functions in the reciprocal space with an equivalent plane-wave mesh cutoff of 100 Ry. For the exchange and correlation potential, we use the local density approximation as proposed by Ceperley and Alder [20] in the parametrization form given by Perdrew and Zunger [21]. A set of six Monkhorst-Pack special k points [35] along the ribbon axis in the first Brillouin zone has been used for the momentum space integration. In order to prevent artificial inter-ribbon interactions, individual ribbons were separated by a sufficiently large vacuum region; both edge-edge distance and layer-layer distance were taken to be more than 10 Å. The atomic ge-

ometry was optimized using the Hellmann-Feynman forces, and the optimal lattice constant along the ribbon axis was determined by comparing the total energies. The forces acting on the individual atom was reduced to less than 10^{-3} eV/Å after the optimization.

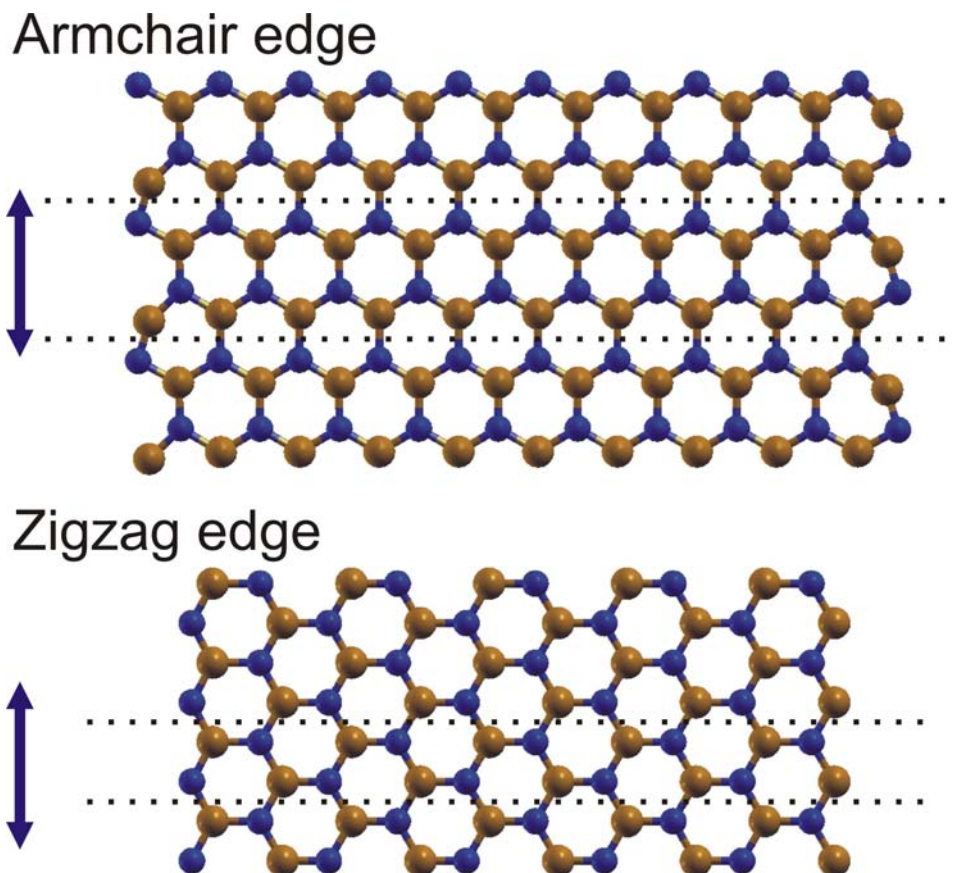


Figure 4.7: Hexagonal Boron Nitride nanoribbons with armchair (top) and zigzag (bottom) edges. It can be seen that the atoms near the edge are displaced from their ideal positions

First, an *ab-initio* calculation was performed to investigate both the structural and electronic properties of an infinite BN sheet. The optimized lattice constant is 2.51\AA , and the BN sheet exhibits a direct energy gap of 4.78 eV at the K point of the 2D Brillouin zone. These results are in good agreement with previous *ab-initio* calculations where the BN sheet band gap is estimated to be 4.3 eV [36]. However, our LDA band gap is clearly underestimated when compared to the experimental band gap of bulk hexagonal BN (ca. 5.5 eV) due to the DFT approximation, which is known to lack of accuracy in the description of the fundamental excitation gap of

semiconductors or insulators.

Subsequently, the optimized atomic structures was calculated for two infinite BN ribbons whose widths lied between 2.0 and 2.5 nm and exhibited zigzag and armchair edges respectively, as shown in figure 4.7. The optimized lattice constant along the ribbon axis does not change significantly from the planar BN sheet. However, some atomic reconstructions could be observed at the edges of the ribbons. For the zigzag ribbon, there is no significant structural change although the bond length between adjacent edge atoms reduces slightly to 1.4 Å. It was noted that the bond length in the center of the BN ribbon is preserved (1.45 Å). However, more significant structural changes for armchair edges were observed (Fig. 4.7), that resulted in a more pronounced decrease of the BN bond length (1.3 Å). The presence of dangling bonds at the edges of these ribbons is responsible for inducing such a significant edge reconstruction. Although the thermal and chemical stability of these BN ribbons free from H termination has not been accurately investigated, their existence is suspected in the surface of the sea-urchin nanospheres. The dehydrogenated edge is estimated to cost 3.5 eV/dangling atom in the zigzag geometry and 1.9 eV/dangling atom in the armchair one. The latter is found to be the most stable edge which could be explained by the formation of the stronger B-N bonding (1.3 Å) between dimer atoms on this specific edge.

The electronic properties of graphitic ribbons without H termination [37], as well as BN and BCN ribbons terminated by hydrogen atoms [38] have already been reported in the literature, illustrating the key role played by the edge states and the ribbon width on the energy gap of the system. However, no previous theoretical study investigates the electronic properties of BN ribbons without hydrogen-termination. Consequently, the aim of the present *ab-initio* calculation is aimed to clarify the electronic properties of these finite BN ribbons.

The presence of free edges induces the appearance of dangling bond states (due to the hydrogen extraction). Edge states are also present, but only for the zigzag BN ribbon, similar to those in graphitic ribbons [37]. In the zigzag case, dangling bond states appear close to the valence edge state, creating a conduction band that crosses the Fermi level and explains the metallic behavior of the zigzag ribbon. In

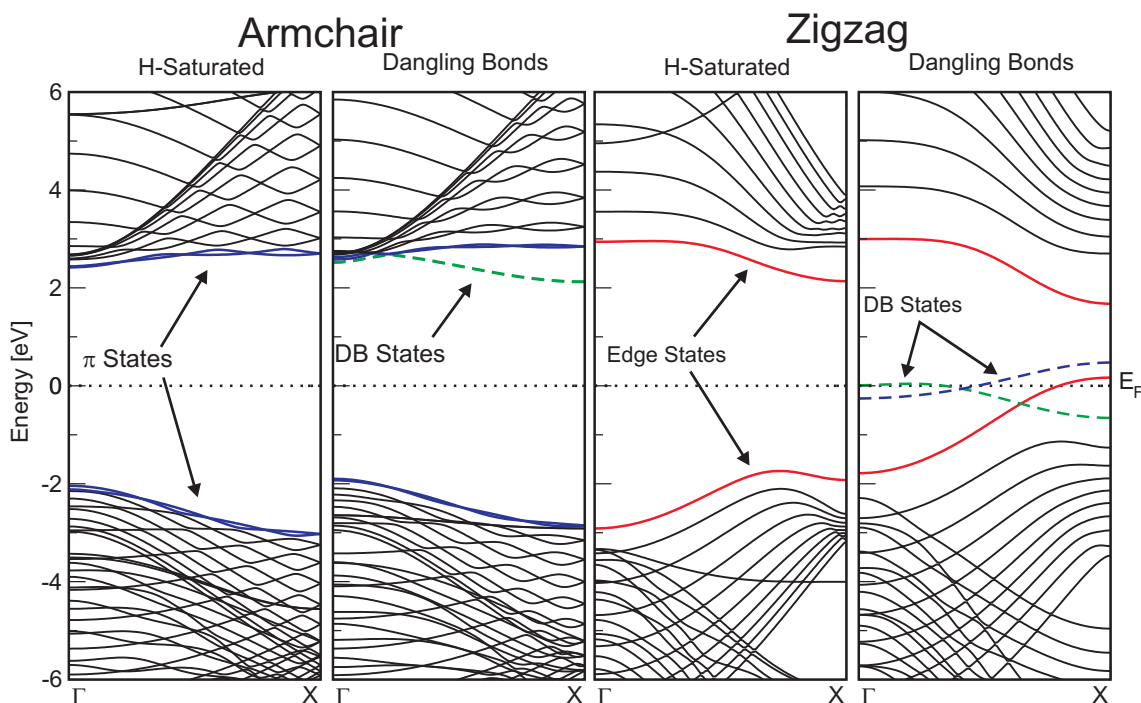


Figure 4.8: Band structure for hydrogenated and free-edge armchair and zigzag boron nitride nanoribbon. After dehydrogenation, a pair of dangling bond states, indicated with arrows, appear below the bottom conduction band for armchair ribbons and just above the valence edge state in zigzag ribbons, and cross the Fermi Level.

the presence of hydrogenated terminations, the same BN ribbon would behave as a 4 eV band gap semiconductor. Similar to graphite, the armchair ribbon does not exhibit edge states. The dangling bond states appear in the bottom of the conduction band, and do not modify the semiconducting behavior of BN armchair ribbons.

Zigzag BN ribbons exhibit a surprising metallic behavior. The position of the dangling bond states allows the presence of unoccupied states just above the Fermi energy and are responsible for explaining the metallic character of these ribbons. These dangling bond states are suspected to play a key role in the chemical reactivity of the ribbon edge.

4.5 Conclusions

Boron nitride nanostructures have great potential for technological applications where the mechanical properties of carbon nanotubes are needed without the chemical reactivity or electrical conductivity. The structural similarity of hexagonal BN (h-BN) to graphite makes it an ideal candidate to form nanostructures similar to those formed by carbon. Boron Nitride nanotubes have been successfully synthesized by a number of different techniques, such as arc discharge, chemical vapor deposition, substitutional reactions and laser ablation, among others. From these techniques, substitutional reactions have proven to be very effective to synthesize boron nitride nanostructures starting from carbon templates.

Boron nitride / carbon (5,5) nanotube heterojunctions with varying content of carbon were studied by *ab initio* first principles methods. It was found that the energy gap of the resulting system could be tuned depending on the composition of

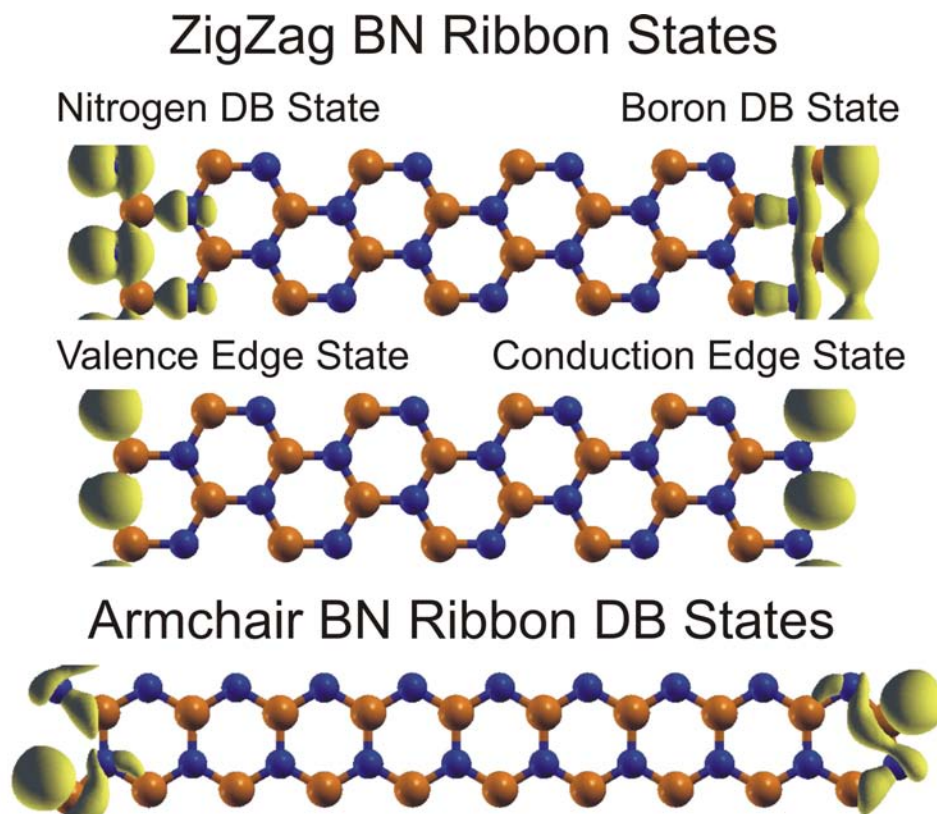


Figure 4.9: Charge density plots of the wavefunctions associated with the dangling bond states (top) and the edge states (bottom)

the BN/carbon nanotube, which was consistent with previous reports[28].

Boron nitride porous nanospheres with exposed BN edges display low *turn-on* voltages for field emission, comparable to carbon nanotubes value, and a very high current stability over time. High resolution TEM observations displayed protuberances in the surface of these nanospheres, that were identified as small exposed ribbons of hexagonal boron nitride with few stacking layers (between 2 and 6 layers). EELS spectroscopy and energy filtered images confirmed that these layers are composed of boron nitride, with no carbon present in the sample. The proposed nanoribbon model revealed that dehydrogenated BN nanoribbons with zigzag edges have unoccupied states at the Fermi level, originating from the dangling bonds of the open edges. For armchair nanoribbons, no edge or dangling bond states are present close to the Fermi level, and thus they remain semiconductive. Further studies of these nanoribbons confirmed that the workfunction for field emission is lowered by about 1.3 eV with respect to bulk h-BN[30].

References

- [1] A. Rubio, J.L. Corkill, and M.L. Cohen. Theory of graphitic boron nitride nanotubes. *Physical Review B*, 49:5081–5084, 1994.
- [2] S. Iijima. Helical microtubules of graphitic carbon. *Nature*, 354:56–58, 1991.
- [3] X. Blase, A. Rubio, S.G. Louie, and M.L. Cohen. Stability and band gap constancy of boron-nitride nanotubes. *Europhysics Letters*, 28:335–340, 1994.
- [4] X. Blase, A. De Vita, J.-C. Charlier, and R. Car. Frustration effects and microscopic growth mechanisms for bn nanotubes. *Physical Review Letters*, 80:1666–1669, 1998.
- [5] N.G. Chopra, R.J. Luyken, K. Cherrey, V.H. Crespi, M.L. Cohen, S.G. Louie, and A. Zettl. Boron nitride nanotubes. *Science*, 296:966–967, 1995.
- [6] A. Loiseau, F. Willaime, N. Demoncy, G. Hug, and H. Pascard. Boron nitride nanotubes with reduced numbers of layers synthesized by arc discharge. *Physical Review Letters*, 76:4737–4740, 1996.
- [7] M. Terrones, W. K. Hsu, H. Terrones, J. P. Zhang, S. Ramos, J. P. Hare, R. Castillo, K. Prassides, A. K. Cheetham, H. W. Kroto, and D. R. M. Walton. Metal particle catalysed production of nanoscale bn structures. *Chemical Physics Letters*, 259:568–573, 1996.
- [8] D. Golberg, Y. Bando, M. Eremets, K. Takemura, K. Kurashima, and H. Yusa. Nanotubes in boron nitride laser heated at high pressure. *Applied Physics Letters*, 69:2045–2047, 1996.
- [9] R. S. Lee, J. Gavillet, M. Lamy de la Chapelle, A. Loiseau, J.-L. Cochon, D. Pigache, J. Thibault, and F. Willaime. Catalyst-free synthesis of boron nitride single-wall nanotubes with a preferred zig-zag configuration. *Physical Review B*, 64:121405, 2001.

- [10] W. Han, Y. Bando, K. Kurashima, and T. Sato. Synthesis of boron nitride nanotubes from carbon nanotubes by a substitution reaction. *Applied Physics Letters*, 73(21):3085–3087, 1998.
- [11] D. Golberg, Y. Bando, K. Kurashima, and T. Sato. Moo_3 -promoted synthesis of multi-walled bn nanotubes from c nanotube templates. *Chemical Physics Letters*, 323:185–191, 2000.
- [12] O.R. Lourie, C.R. Jones, B.M. Bartlett, P.C. Gibbons, R.S. Ruoff, and W.E. Buhro. Cvd growth of boron nitride nanotubes. *Chemistry of Materials*, 12:1808–1810, 2000.
- [13] W.L. Wang, X.D. Bai, K.H. Liu, Z. Xu, D. Golberg, Y. Bando, and E.G. Wang. Direct synthesis of b-c-n single-walled nanotubes by bias-assisted hot filament chemical vapor deposition. *Journal of the American Chemical Society*, 128:6530–6531, 2006.
- [14] Y. Chen, J. Fitz Gerald, J. S. Williams, and S. Bulcock. Synthesis of boron nitride nanotubes at low temperatures using reactive ball milling. *Chemical Physics Letters*, 299:260–264, 1999.
- [15] J.J. Velázquez-Salazar, E. Munoz-Sandoval, J.M. Romo-Herrera, F. Lupo, M. Rühle, H. Terrones, and M. Terrones. Synthesis and state of art characterization of bn bamboo-like nanotubes: Evidence of a root growth mechanism catalyzed by fe. *Chemical Physics Letters*, 416:342–348, 2005.
- [16] J. Fengqiu, C. Chuanbao, X. Hong, and Ziguang Y. Mechano-synthesis of boron nitride nanotubes. *Chinese Journal of Chemical Engineering*, 14:389–393, 2006.
- [17] D.L. Carrol, Ph. Redlich, X. Blase, J.-C. Charlier, S. Curran, P.M. Ajayan, S. Roth, and M. Rühle. Effects of nanodomain formation on the electronic structure of doped carbon nanotubes. *Physical Review Letters*, 81:2332, 1998.
- [18] X. Blase, J.-C. Charlier, A. de Vita, and R. Car. Theory of composite $\text{B}_x\text{C}_y\text{N}_z$ nanotube heterojunctions. *Applied Physics Letters*, 70:197, 1997.

- [19] V. Meunier, C. Roland, J. Bernholc, and M.B. Nardelli. Electronic and field emission properties of boron nitride/carbon nanotube superlattices. *Applied Physics Letters*, 81:46, 2002.
- [20] D. M. Ceperley and B. J. Alder. Ground state of the electron gas by a stochastic method. *Physical Review Letters*, 45:566–569, 1980.
- [21] J.P. Perdew and A. Zunger. Self-interaction correction to density-functional approximations for many-electron systems. *Physical Review B*, 23:5048, 1981.
- [22] P. Hohenber and W. Kohn. Inhomogeneous electron gas. *Physical Review*, 136: B864–B871, 1964.
- [23] W. Kohn and L. J. Sham. Self-consistent equations including exchange and correlation effects. *Physical Review*, 140:A1133–A1138, 1965.
- [24] N. Troullier and J. L. Martins. Efficient pseudopotentials for plane-wave calculations. *Physical Review B*, 43:1993–2006, 1991.
- [25] L. Kleinman and D. M. Bylander. Efficacious form for model pseudopotentials. *Physical Review Letters*, 48:1425–1428, 1982.
- [26] J. M. Soler, E. Artacho, J. D. Gale, A. García, J. Junquera, P. Ordejón, and D. Sánchez-Portal. The siesta method for ab-initio order-N materials simulation. *Journal of Physics: Condensed Matter*, 14:2745–2779, 2002.
- [27] J. Junquera, O. Paz, D. Sánchez-Portal, and E. Artacho. Numerical atomic orbitals for linear-scaling calculations. *Physical Review B*, 64(23):235111, Nov 2001. doi: 10.1103/PhysRevB.64.235111.
- [28] J. Choi, Y.-H. Kim, K.J. Chang, and D. Tománek. Itinerant ferromagnetism in heterostructured c/bn nanotubes. *Physical Review B*, 67:125421, 2003.
- [29] J.D. Guo, C.Y. Zhi, X.D. Bai, and E.G. Wang. Boron carbonitride nanojunctions. *Applied Physics Letters*, 80:124, 2002.
- [30] M. Terrones, J.-C. Charlier, A. Gloter, E. Cruz-Silva, E. Terrés, Y.B. Li, A. Vinu, Z. Zanolli, J.M. Dominguez, H. Terrones, Y. Bando, and D. Golberg.

- Experimental and theoretical studies suggesting the possibility of metallic boron nitride edges in porous nanourchins. *Nano Letters*, pages 1026–1032, 2008.
- [31] T. Sugino, C. Kimura, and T. Yamamoto. Electron field emission from boron-nitride nanofilms. *Applied Physics Letters*, 80(19):3602–3604, 2002.
- [32] A. G. Rinzler, J. H. Hafner, P. Nikolaev, P. Nordlander, D. T. Colbert, R. E. Smalley, L. Lou, S. G. Kim, and D. Tomanek. Unraveling nanotubes: Field emission from an atomic wire. *Science*, 269:1550–1553, 1995.
- [33] D. Golberg, Y. Bando, K. Kurashima, and T. Sato. title. *Chemical Physics Letters*, 323:185–191, 2000.
- [34] D. Golberg, Y. Bando, K. Kurashima, and T. Sato. title. *Solid State Communications*, 116:1–6, 2000.
- [35] H.J. Monkhorst and J.D. Pack. title. *Physical Review B*, 13:5188–5192, 1976.
- [36] X. Blase, A. Rubio, S.G. Louie, and M.L. Cohen. Quasiparticle band structure of bulk hexagonal boron nitride and related systems. *Physical Review B*, 51:6868–6875, 1995.
- [37] T. Kawai, Y. Miyamoto, O. Sugino, and Y. Koga. Graphitic ribbons without hydrogen-termination: Electronic structures and stabilities. *Physical Review B*, 62:R16349–R16352, 2000.
- [38] J. Nakamura, T. Nitta, and A. Natori. Electronic and magnetic properties of bnc ribbons. *Physical Review B*, 72:205429, 2005.

Chapter 5

Studies of non-graphitic carbon nanostructures

5.1 The Coalescence Induced Mode

While studying the process of Boron doping of double-walled carbon nanotubes (DWNT) by heat treatment, a new vibrational mode of carbon systems was observed by Endo et al. [1] close to 1855cm^{-1} . By comparing the Raman spectra of these samples with high resolution transmission electron microscope images, it was correlated with the coalescence process that takes place at critical temperatures, and hence it was termed “Coalescence Induced Mode”, or CIM.

The mentioned double walled nanotubes were highly purified by a two-step purification process, involving a 10 hours bath in hydrochloric acid (HCl) at 100°C to remove metal particles and a 30 minutes oxidation in air at 500°C , which removes the amorphous carbon. The resulting product after filtration is a dark paperlike sheet, consisting of double walled nanotubes with a very narrow diameter distribution. This procedure is described in more detail by Endo et al. [2].

For the boron doping process, DWNT were mixed with 0.05 wt % of elemental boron, and then were thermally treated at different temperatures from 1000 to 2000°C in a graphite-resistance furnace in a high purity argon atmosphere (99.999%) for 30 minutes [3]. Control samples without boron were subject to a high temperature treatment (HTT) under the same conditions.

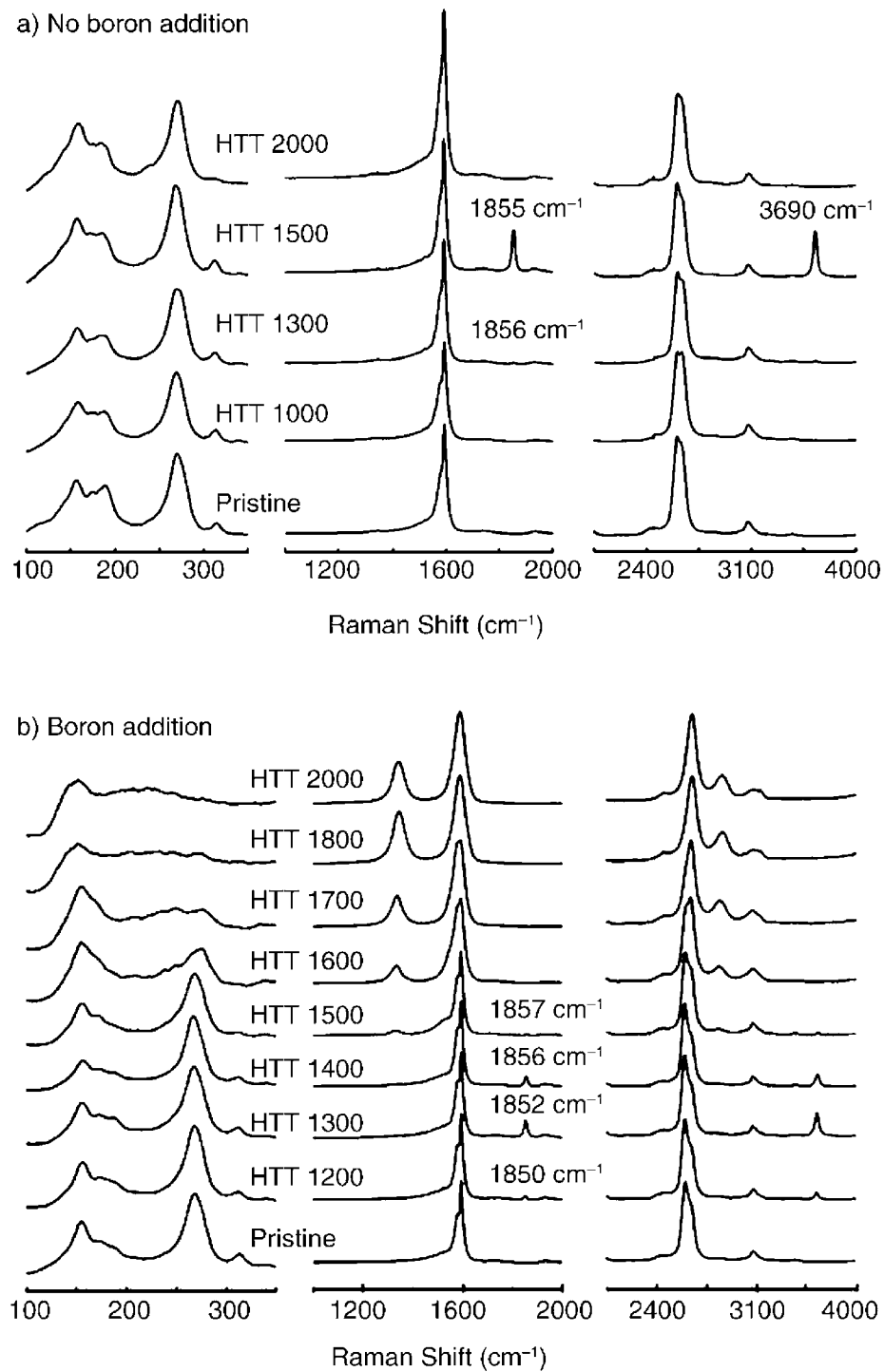


Figure 5.1: Raman spectra of double-walled carbon nanotubes taken at 2.33eV, either pristine or at different heat treatment temperatures (HTT). a) Without boron doping, and b) with boron doping. Adapted from [1]

While comparing the Raman spectra (taken at 2.33 eV) of the undoped samples treated at different heat treatment temperatures, shown in figure 5.1a, it was noticed that for the 1300°C sample, a very weak Raman-active mode suddenly appears close to $\omega_{\text{CIM}} = 1856\text{cm}^{-1}$. In the spectra of the 1500°C sample, a sharp peak appears at $\omega_{\text{CIM}} = 1855\text{cm}^{-1}$, along with a correlated sharp peak located close to $2\omega_{\text{CIM}}$, at $\omega_{2\text{CIM}} = 3690\text{cm}^{-1}$, that is, it is its second harmonic.

For the boron-doped case shown in figure 5.1b, it can be seen that the CIM feature appears at lower temperatures. No feature is present for the pristine case, but for the 1200°C, a small peak is observed, while it gains intensity for the 1300 and 1400°C, and decreases again for the 1500°C. At this temperature, the radial breathing mode (RBM) peak corresponding to the narrower diameter tubes starts broadening, and its intensity is reduced for higher temperatures, while the CIM feature is no longer observed.

Comparing the Raman spectra with high resolution images (see figure 5.2) of the heat treated double walled nanotubes, a correlation between the CIM feature and the coalescence of double walled nanotubes can be proposed. For the undoped case, both Raman and HRTEM images show that there is no major structural changes even for a 2000°C treatment. Opposed to this, for the boron doped case there are noticeable structural changes. The sample keeps its hexagonal structure and nanotube size uniformity up to 1300°C, although at this temperature the CIM peak has its highest intensity. The sample treated at 1400°C already shows evidence of coalesced nanotubes (fig. 5.2e), and it has the second highest peak in ω_{CIM} . At 1500°C, bi-cable structures and fully coalesced nanotubes are observed, while the CIM feature in the Raman spectra is diminished. For the 1600 and 1700°C samples, larger diameter nanotubes and small nanographite domains are seen, while the CIM feature disappeared and the RBM mode corresponding to small nanotubes is broadened and reduced.

Raman features very close to the range of interest were previously reported by different work groups. In particular, Zhao et al. [4] observed sharp and intense Raman bands around 1825 and 1850 cm^{-1} in the Raman spectra of Multiwalled carbon nanotubes (MWCNT), and ascribed those bands to a long linear carbon

chain of more than 100 atoms, and inserted inside a MWCNT core. Later, Jinno et al. [5] described very similar bands, located at 1829 and 1855 cm^{-1} , while heat-treating multi- and double-walled carbon nanotubes. They also ascribed this modes to long linear carbon chains located in the inside of narrow diameter (ca. 0.6nm) carbon nanotubes, while they explained the different frequencies to the possibility of cumulenic ($=C=$) or polyynic ($-C\equiv$) carbon chains.

The 1850 cm^{-1} frequency is consistent with the CIM mode observation, but the

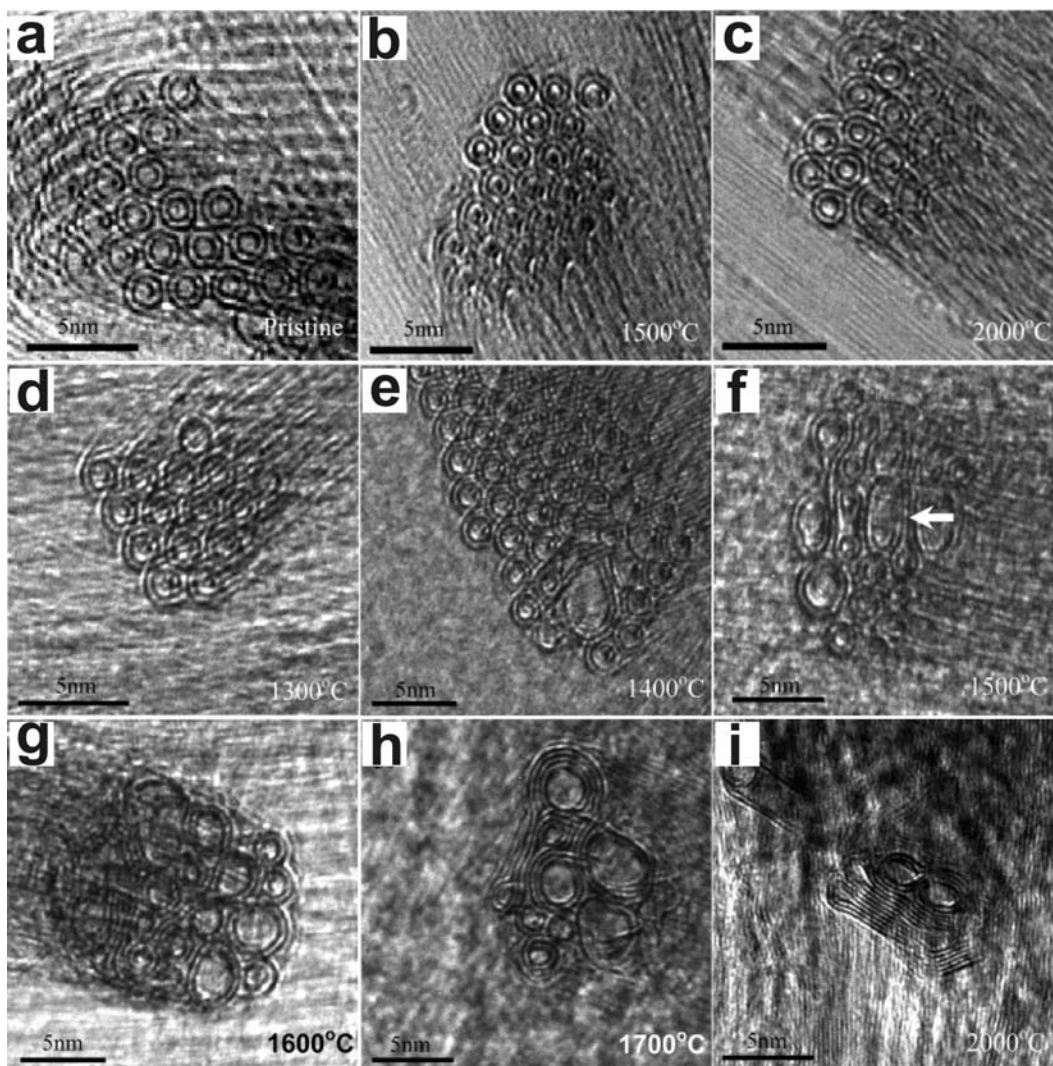


Figure 5.2: High resolution transmission electron micrographs of undoped (a-c) and boron doped (d-i) double walled carbon nanotubes treated at different temperatures. Pristine undoped DWNT (a), DWNT treated at 1500 (b), and 2000°C (c). Boron doped DWNT, treated at 1300 to 1700°C (d-h) and 2000°C (i). Adapted from Endo et al. [3].

sharp peak at 1825 cm^{-1} was not observed in these samples. Also, it is known that a linear chain with one atom per unit cell (cumulenic) does not have a Raman-active mode, as discussed by Rusznyák et al. [6]. They also showed that the interaction of in-tube carbon chains with their host can suppress the Peierls distortion responsible of the polyynic structure. Finally, previous studies of the atomic vibrations of the sp -bonded polyynic structures known as carbynes have shown that the $C\equiv C - C$ stretching mode frequency is over 2000 cm^{-1} [7].

The carbon-carbon stretching modes have a higher energy when the binding is stronger. In sp^3 bonded carbons, the C-C stretching mode have been recorded at frequencies close to 1332 cm^{-1} , sp^2 bonded graphite has a typical 1532 cm^{-1} vibration frequency and for sp -bonded carbynes it has been recorded above 2000 cm^{-1} . The lack of dispersion of the CIM peak with laser energy, its narrow linewidth (ca. 15 cm^{-1}), and the correlation with its second harmonic, made the authors conclude that the CIM is a first order Raman mode. From the high frequency of the CIM, above the maximum 1620 cm^{-1} of the 2D sp^2 carbons, but below the 2000 cm^{-1} frequencies reported for carbyne molecules, this mode was associated with vibrations of short linear chains of carbon.

5.2 Resonant Raman study of the CIM mode

To further characterize this unusual Raman feature, Fantini et al. [8] performed a complete resonance Raman study of the CIM feature using several laser excitation energies from an Ar-Kr ion laser and a dye laser for an energy range of 1.9–2.7eV. It was confirmed that the CIM feature had its maxima for 1500°C heat treatment for undoped samples, and for 1300°C for boron-doped samples, as observed by Endo et al. [1].

From figure 5.1 it is seen that the undoped HTT1500 sample has small features located next to the CIM feature, around 1700 and 1900 cm^{-1} , which correspond to two phonon combination modes (2oTO and iTOLA). The CIM feature is located between them, close to 1850 cm^{-1} . In figure 5.3a, four different spectra obtained at different sample locations are displayed, and it can be seen that the composition

of this feature varies upon the location of the laser spot. It can be seen that at least two and up to four different Lorentzian peaks were needed to fit the collected spectra.

In figure 5.3b the frequency of the Lorentzian peaks is plotted versus the laser

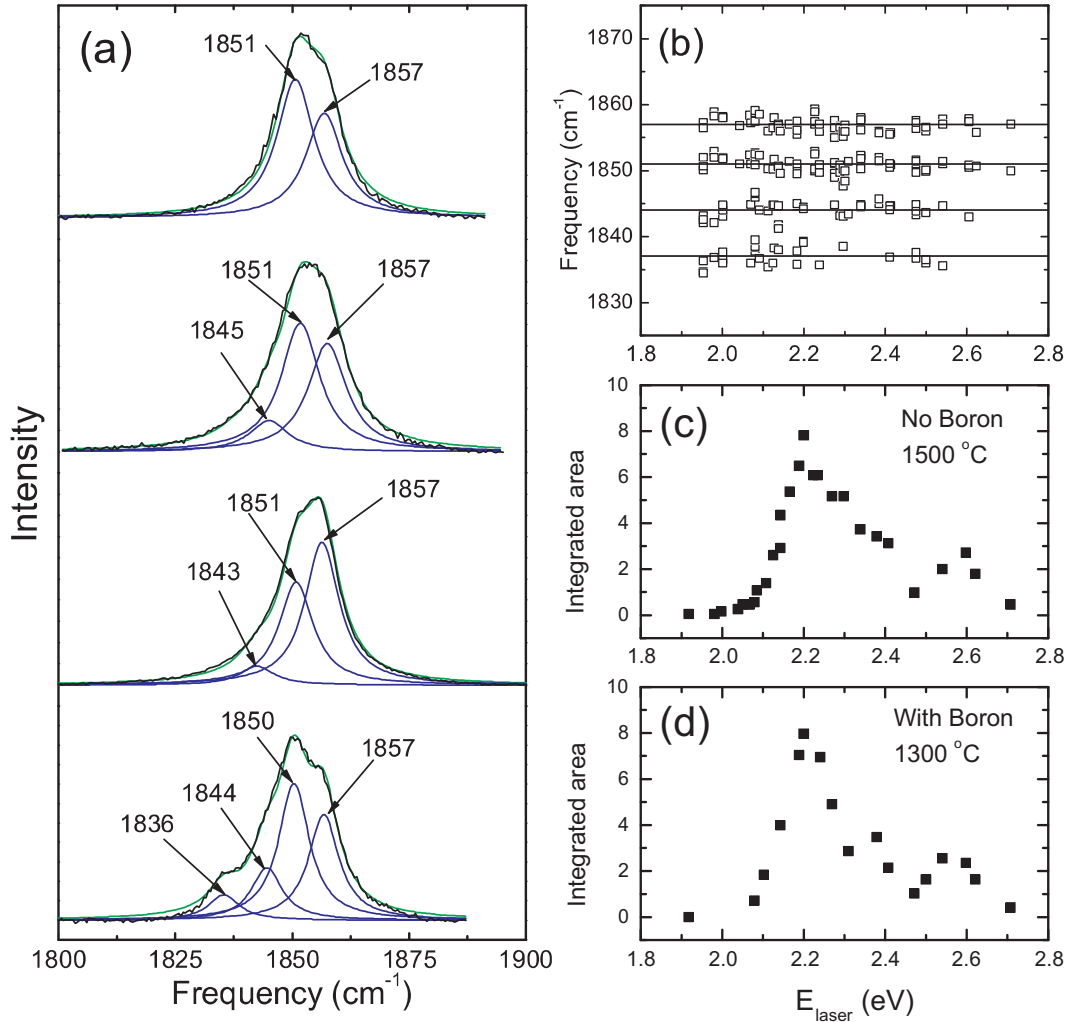


Figure 5.3: a) Deconvolution of the CIM feature obtained at $E_{\text{laser}}=2.2$ eV at different locations of an undoped sample heat treated at 1500°C . Black lines are the collected spectra, blue lines represent the Lorentzian functions and the green lines represent the fitted spectra. b) Frequency vs E_{laser} for all Lorentzian peaks used to fit the CIM feature. Notice the distribution of frequencies around four main values, indicated with continuous lines. c) Resonant Raman profile for the CIM feature of the undoped sample heat treated at 1500°C , and d) for the boron-doped sample heat treated at 1300°C . The arrows indicate the resonance local maxima with E_{laser} . Adapted from Fantini et al. [8].

excitation energy. It is observed that even though the functions are centered at different frequencies, these are located around four different positions, identified as 1837, 1844, 1851, and 1857 cm^{-1} with a precision of $\pm 2\text{cm}^{-1}$. The lack of dispersion in their frequency demonstrate that these peaks are not related with combination modes, and that they correspond to a unique form of carbon.

In figure 5.3c,d the resonance Raman profiles for the CIM feature are shown for both undoped and boron-doped samples heat treated at 1500 and 1300°C, respectively. Their resonance behavior is very similar, with identical position for the global maximum at 2.2 eV, and local maxima also at 2.4 and 2.6 eV, confirming that boron atoms, while helping to reduce the temperature needed for the CIM mode to occur, are not directly involved in the vibration that gives rise to the CIM band.

Further oxidation and chemical doping studies were performed by Muramatsu et al. [9] in order to clarify the location of these carbon chains that appeared when heat treating DWNT in an argon atmosphere. For this purpose, a sample of undoped DWNT thermally treated at 1500°C were then air-oxidized at 400, 500 and 600°C

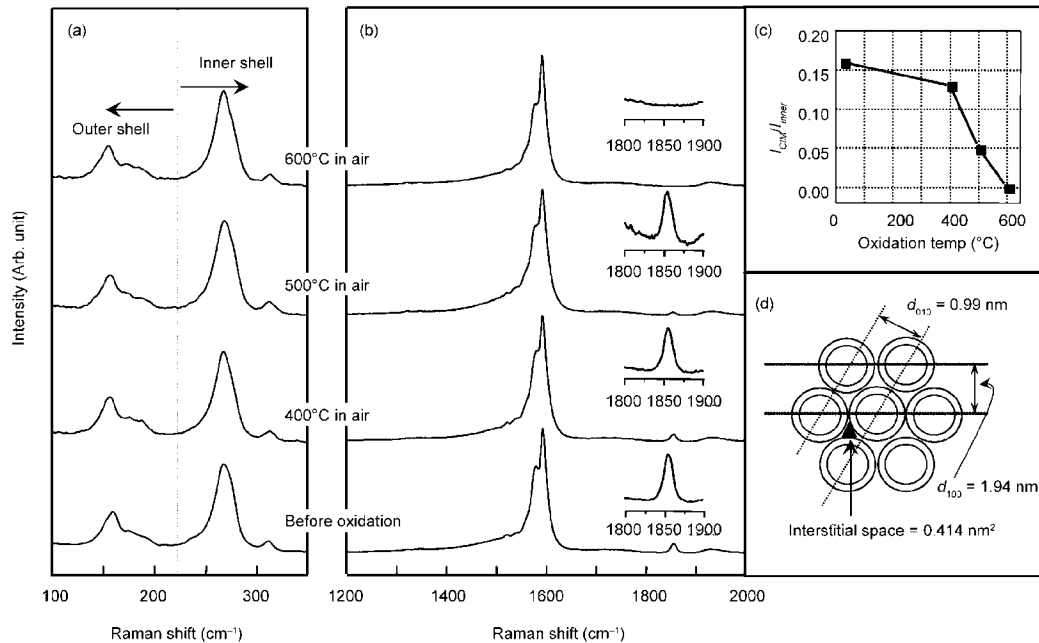


Figure 5.4: Low frequency (a) and first-order Raman spectra (b) from DWNT thermally treated at 1500°C, and their air-oxidized samples at 400, 500 and 600°C. c) Profile of the CIM intensity values with different oxidation temperatures. d) Schematic of the stacking of DWNT as derived from their XRD patterns.

for 30 min. Figure 5.4a,b shows the Raman spectra of these samples, collected at $E_{\text{laser}} = 2.33\text{eV}$. It can be observed that there are no significant changes to the RBM and the G band, and that the D-band is absent up to the 600°C oxidized sample, concluding that no major structural changes occurred in the nanotube samples. From the changes in the CIM feature, it can be observed that it starts to decrease at 400°C, until it finally vanishes for 600°C.

The decrease of the CIM feature with increasing oxidation temperatures (see figure 5.4c) while there are no changes in the RBM, and the D and G bands, suggests that the previous carbon chains are being removed due to a selective oxidation of these chains located interstitially between the DWNT. This is confirmed by the low temperature at which the CIM band starts to decrease, compared to the high oxidation stability of up to 540°C from the experiment of Jinno et al. [5], where carbon chains were located at the interior of MWNTs.

From X-Ray diffraction (XRD) data that shows clear (100) and (010) diffraction peaks, it was concluded that a homogeneous packaging of DWNTs leads to the creation of triangle-like interstitial spacings close to 0.414 nm^2 , as depicted in figure 5.4d. Thermal treatment might create single or cluster carbons, which are energetically stabilized by the confinement in the triangular interstitial spaces of bundled DWNTs. With increasing heat treatment temperatures, thermally activated carbons would be stabilized by a) the formation of short linear carbon chains, like the interconnections between DWNTs; or b) the formation of longer linear carbon chains stabilized by the confinement.

Chemical doping experiments were carried out by treating DWNT in concentrated sulfuric acid at room temperature for 1 minute and by exposing the sample to sulfuric acid vapor at 100°C for 1 minute. Since the inner nanotubes are protected by the outer wall of DWNTs, their response to chemical doping would be selective. If the carbon chains were located in the inner cores of DWNTs, the CIM feature should not be affected by chemical doping due to a protective effect of the outer nanotube. In figure 5.5, it is observed that while the inner tubes are highly protected by the outer shell of the DWNTs and their associated RBM peak remains unchanged, the CIM is increased as the DWNT outer shell RBM mode is depressed,

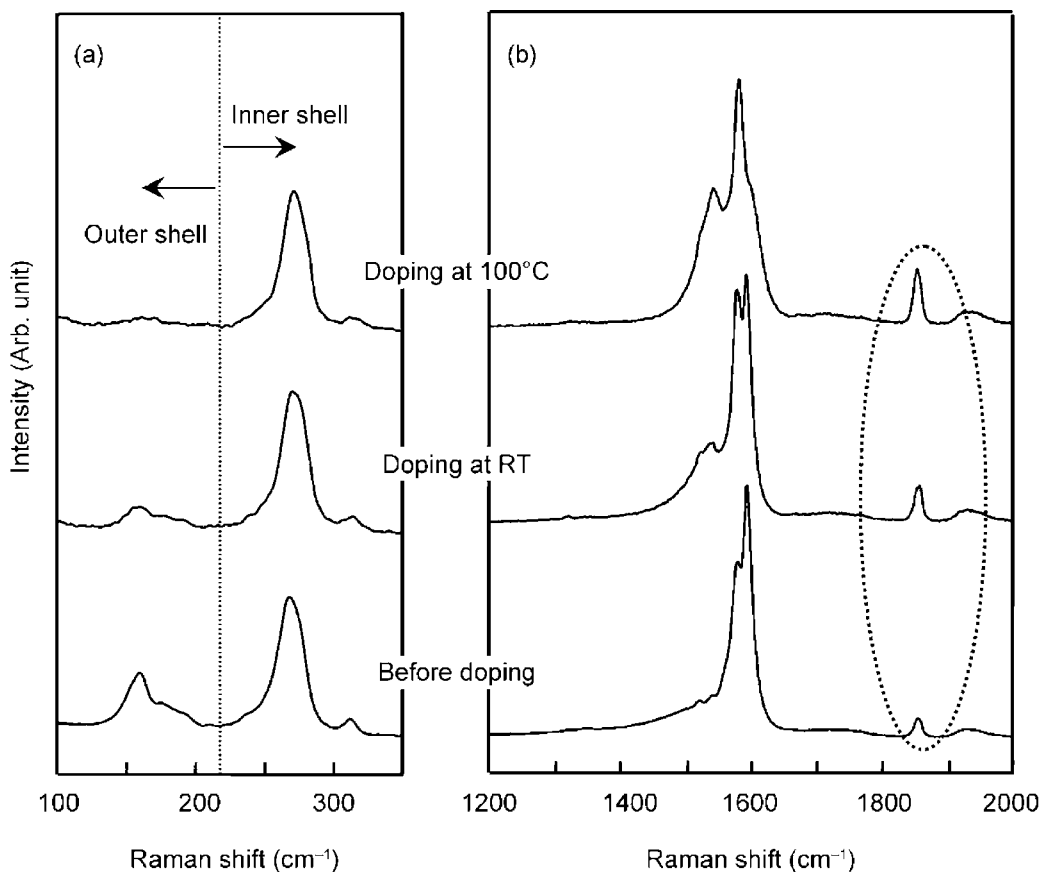


Figure 5.5: Low frequency (a) and first-order Raman spectra (b) from DWNT thermally treated at 1500°C, and their chemically doped samples after treatment in sulfuric acid at room temperature (RT) and 100°C for 1 minute.

indicating that both of them are affected by the charge transfers from the sulfuric ions. This confirms that the carbon chains responsible of the CIM feature could not be encapsulated inside the DWNT core.

Molecular dynamics calculations of two adjacent (5,5) with 12 B atom placed between them were performed using the atom centered density matrix propagation model at the AM1 semi-empirical level of theory with GAUSSIAN03 [10]. These calculations showed that carbon threads appear during the simulation while the nanotube coalescence process is occurring. MD simulations also show carbon chains of 3, 4 and 5 atoms linking the inner and outer tubes covalently, sections of the same nanotube, and as interconnections between inner the inner tubes in a semi-coalesced binocular-like structure.

5.3 *Ab initio* calculations of linear carbon chains

In order to understand the Raman frequencies observed experimentally, theoretical calculations were performed to optimize the geometry and obtain the vibrational frequencies of short linear carbon chains from C_3 to C_{10} , and their boron doped counterparts BC_2 to BC_9 . For this purpose, the ABINIT [11] code was used within the local density approximation using Troullier-Martins pseudopotentials[12].

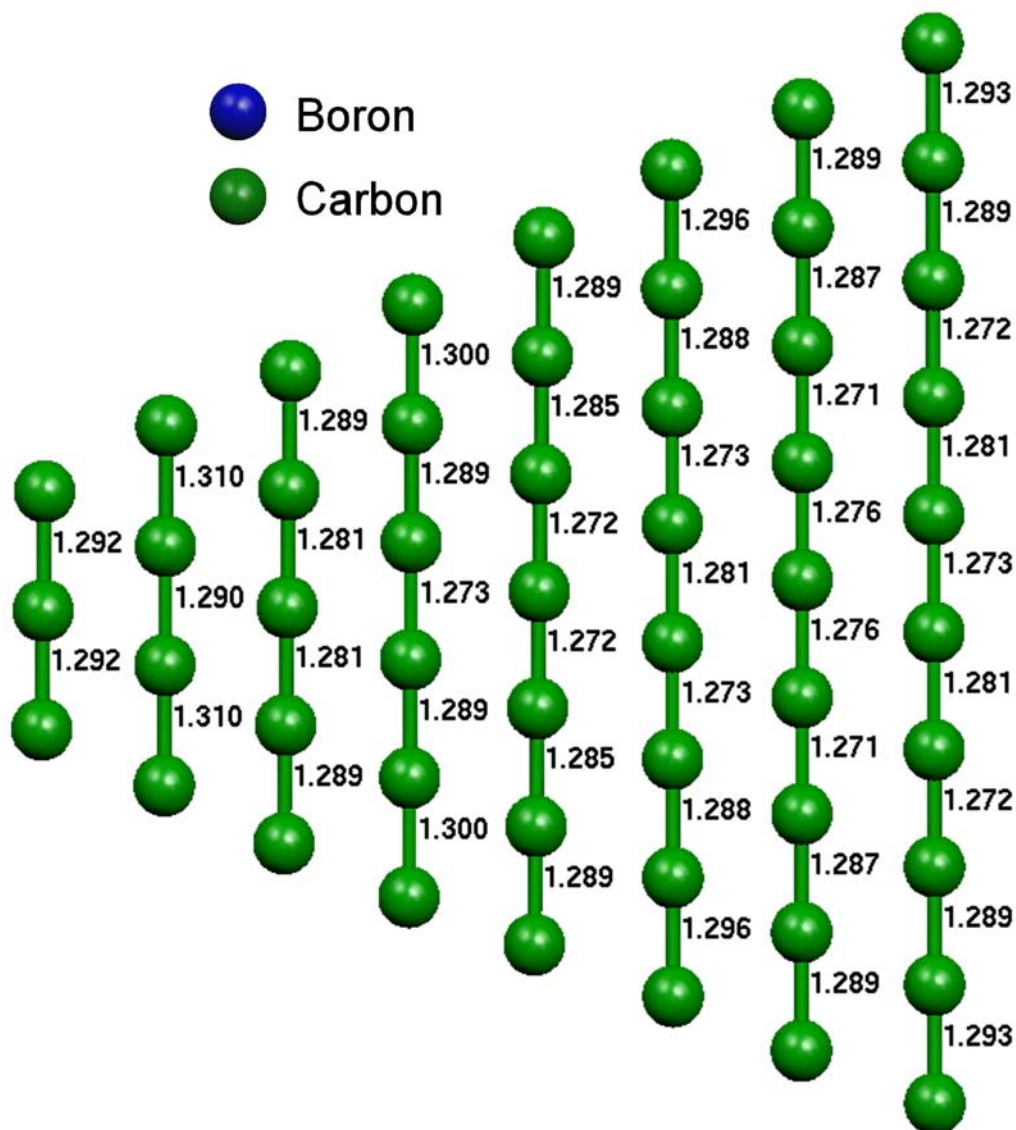


Figure 5.6: Relaxed Structures of carbon chains containing from 3 to 10 atoms. Notice that the outer bonds are longer due to the dangling bonds in the outer atoms.

The proposed model of short carbon chains is based upon the experimental facts

described in the previous sections. The carbon chains were placed in supercells large enough to avoid interactions among them. The structures were then relaxed and the second derivatives of the total energy versus the atomic displacements were calculated. Two different scenarios were proposed, in the first one a free standing chain is analyzed, while in the second scenario the outer atoms of the chain were held at fixed positions and the rest of the atoms were allowed to vibrate freely. The later scenario corresponds to carbon chains that link two structures and hence the outer atoms have a reduced mobility.

Figure 5.6 shows the relaxed structure of these carbon chains. It is observed in the longer chains that the bond length has a small alternation, from center toward the extrema, 1.273-1.281-1.272-1.289-1.293 Å, and that always the outer bond length is longer than the rest of them, due to the presence of dangling bonds in the last atom. This results are very similar to the bond lengths of linear carbon chains reported by

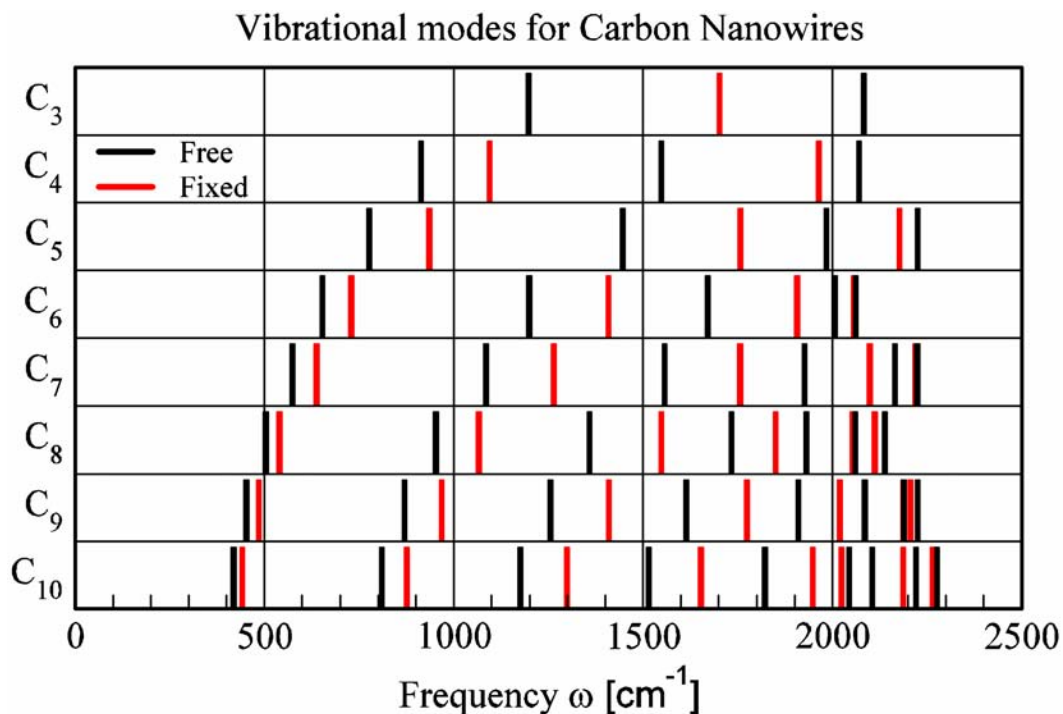


Figure 5.7: Frequencies for the normal vibrational stretching modes for free-standing and fixed-end linear carbon chains. Black lines represent the free chains, while the red lines represent carbon chains with their outer atoms held at fixed positions, resembling atoms that have reduced mobility due to bonding to larger carbon structures.

Agrawal et al. [13]. The calculated vibrational frequencies for these carbon chains are shown in figure 5.7. It is observed that for each chain, the vibration frequencies are blue-shifted when the chain extrema have fixed positions. Here it can also be observed that the frequency of the basal stretching mode has a clear inverse relation to the length of the carbon nanowire for both the free-standing chains and the fixed-end chains. For large nanowires, like the C_{10} chain, the vibration frequencies for the basal mode are very similar for both the free and fixed-end chains. Boron doped carbon chains were also considered, and it was found that the vibration frequencies were red-shifted in all cases upon boron addition. Since the CIM feature does not change its frequency in boron-doped systems, it is concluded that it is unlikely that boron has an active role in the CIM vibrational mode.

Table 5.1 shows the calculated phonon frequencies for the stretching modes and the energy gaps of linear carbon chains with a small number of atoms, from C_3 to C_7 . It should be mentioned that the Energy gaps obtained by this method are underestimated, this being a well-known problem of DFT methods. However, we can assure that even-numbered carbon chains have energy gaps above the visible-light region, since their calculated gaps exceed 3 eV. This leads to the conclusion that the CIM feature is associated with odd-numbered carbon chains. The calculated frequencies for the Raman active stretching modes of the chains with 5 and 7 atoms, located at 1757 and 2098 cm^{-1} , could be related to the experimental value of ca. 1850

Table 5.1: Vibrational stretching mode frequencies (ω_{chain}) and gap energy (E_{gap}) for carbon chains with fixed ends, calculated for carbon chains containing 3–7 atoms. The Raman-active modes are boldface.

No. Atoms	ω_{chain} [cm^{-1}]	E_{gap} [eV]
3	1701	2.19
4	1094, 1964	4.13
5	935, 1757 , 2177	1.98
6	729, 1407 , 1906, 2056	3.02
7	637, 1264 , 1756, 2098 , 2219	1.68

cm^{-1} . It has been found that LDA calculations overestimate the Raman frequencies by 10–15% [14]. Therefore, the Raman mode for the fixed C_7 chain (2098 cm^{-1}) would be in agreement with the experiment. In case of the C_5 chain, the vibration mode at 1757 cm^{-1} is below the experimental value, but when this chain is subject to mechanical stress, like twisting or stretching, upshifts of $100\text{--}150 \text{ cm}^{-1}$ could be achieved. The existence of longer chains is unlikely during the coalescence process. For unfixed (free standing) chains, the Raman active modes have frequencies much higher than those for the fixed chains, so it is concluded that C_5 and C_7 chains with fixed ends are the best candidates for CIM.

It should also be considered that, during DWNT coalescence, different types of compressed, deformed and bent C_5 chains are present. Further calculations of a C_5 chain with phenyl-ring terminations using Hartree-Fock calculations with the 6-311++G(d,p) basis in GAUSSIAN03 [10] shown that it has Raman active modes at 2506 and 1820 cm^{-1} . If this chain is bent to coincide with the curvature of a (10,10) nanotube, the frequency of the later Raman mode is upshift to 1825 cm^{-1} . This result reflects that different peaks that conform the CIM peak could be due to the bending of chains caused by different strains, also affected by different bonding environments.

5.4 Small Carbon Clusters

Recent experimental reports on magnetic properties of carbon have motivated the interest in carbon systems as new magnetic materials made of light elements. Magnetic measurements in nanographite have demonstrated the existence of ferromagnetism. Magnetic force microscopy measurements by Esquinazi et al. [15] performed on proton-irradiated highly oriented pyrolytic graphite (HOPG), demonstrated that it is possible to create ferromagnetic domains with arbitrary shape and size up to $1\mu\text{m}^2$. However, the origin of the magnetic ordering is still unclear.

In the case of carbon clusters, there is a theory by Astala et al. [16] concerning the encapsulation of carbon clusters inside C_{60} , that indicates that the confinement inside the fullerene can stabilize small carbon clusters that otherwise would not exist.

Later, a theoretical work by Liu et al. [17] studied carbon chains, rings, graphitic sheets, bowls, cages and tubes inside carbon nanotubes, finding that carbon species with saturated bonds have a minimum distance of 3.4 Å from the nanotube, and that large carbon species induce deformation in the nanotubes. An experimental group have reported the successful encapsulation of linear $C_{10}H_2$ molecules inside single-walled carbon nanotubes. Also, the works described in section 5.1 [1, 8, 9], detected Raman active modes located around 1855 cm^{-1} on bundles of double-walled carbon nanotubes, associated to the presence of small encapsulated linear carbon chains.

There are several theoretical studies that have addressed the ferromagnetic behavior of carbon systems. In this context, Park et al. [18] used *ab initio* density functional theory to study the magnetic properties of carbon nanotube tetrapods, claiming that the presence of heptagonal carbon rings causes the unusual magnetic behavior.

Also, using tight binding molecular dynamics (TBMD) and *ab initio* methods, Andriotis et al. [19] studied the magnetism in polymerized C_{60} molecules by introducing symmetrical vacancies. Their results conclude that magnetism appears in the rhombohedral phase of the C_{60} (Rh- C_{60}) solid. Later, Chan et al. [20] investigates the structural defects of Rh- C_{60} produced at high pressure and temperature, finding a ferromagnetic state (of $0.34 \mu_B$ per cage), emphasizing that hydrogen atoms play a crucial role in the ferromagnetic coupling of the defects.

In this account, full many body calculations were performed for the total spin operator on different sp^2 carbon clusters, using the Hubbard model [21–24], which in real space is written as:

$$H = \sum_{\langle i,j \rangle} V_{\pi} c_{i\sigma}^{\dagger} c_{j\sigma} + U \sum_i n_{i\uparrow} n_{i\downarrow} \quad (5.1)$$

Where $\langle i, j \rangle$ denotes nearest-neighbor sites, $c_{i\sigma}^{\dagger}$ ($c_{i\sigma}$) refers to the creation (annihilation) operator for an electron at site i with spin σ , $n_{i\sigma}$ is the number operator. V_{π} is the electronic hopping, and U the on-site Coulomb repulsion. This model is solved numerically by expanding its eigenfunctions $|\Psi_n\rangle$ in a complete set of basis states $|\Phi_m\rangle$ which have definite occupation numbers at all orbitals [25]. The Lanczos numerical diagonalization method [26] is used in order to obtain the ground-state

energy and the associated wave function.

Taking into account all possible electronic configurations may imply a considerable numerical effort which in practice sets a drastic limit to the size of the cluster under study. For example, in a cluster with 14 atoms and one-electron per atom, the Hilbert space is approximately 12×10^6 . It was found in the carbon literature that the estimation of the on-site Coulomb repulsion (U) between electrons in the C_{60} molecule is approximately 9 eV, and the electronic hopping V_π is around of 3 eV [27–30], then $\beta = U/V_\pi = 3$. The dimensionless parameter β was varied in order to investigate the role of electronic correlations in different carbon clusters. It is also well known that the Hubbard model with one-electron per atom and large values of β promotes antiferromagnetic correlations. However, for weak values of β , different magnetic transitions could be obtained.

All cluster geometries were generated for 10, 12, and 14 carbon atoms with sp^2 -like hybridized bonds (three coordinated atoms). There were 9, 32, and 138 different isomers for clusters containing 10, 12, and 14 atoms respectively. Figure 5.8 shows all the studied geometries that had a ground state total spin different from zero. It has been observed that the variation of the dimensionless parameter β can give origin to a ground state with $S = 1$. For the 10-atom clusters, it was found that the geometries corresponding to the labels “iso-d” to “iso-i” exhibit $S = 1$. The interval of β where the triplet state appears strongly depends of the cluster geometry as shown in table 5.2.

Table 5.2: Values for dimensionless parameter β for which C_{10} cluster exhibit ferrimagnetic ground state.

C_{10} isomer	Interval	Total Spin
Iso-d	$1.20 \leq \beta \leq 1.56$	$S=1$
Iso-e	$2.80 \leq \beta \leq 3.80$	$S=1$
Iso-f	$0.96 \leq \beta \leq 1.44$	$S=1$
Iso-g	$0.00 < \beta \leq 2.36$	$S=1$
Iso-h	$0.72 \leq \beta \leq 2.36$	$S=1$
Iso-i	$0.00 < \beta \leq 4.50$	$S=1$

For the 12 atoms clusters, there were 12 ferrimagnetic geometries found, which are shown in figure 5.8. The values of β for which these structures display a non-zero total spin are shown in table 5.3. Notice that one of the isomers presents a total spin of $S = 2$, being a unique case. For the 14 atoms clusters, a complete survey of the β values was not possible due to the size of the problem, so it was reduced to representative β values of 0.5, 1.0, 2.0, 3.0, 4.0, 5.0 and 6.0, for which there were 8, 15, 26, 18, 5, 2 and 4 ferrimagnetic clusters, respectively. Notice that the maximum of magnetic clusters is obtained for $\beta = 2$.

It should be noticed that prismane-like molecules are magnetic for the odd-numbered rings, that is, “iso-g” for the 10 atom cluster and “iso-z” for the 14 atom cluster. In the case of the hexagonal prismane-like cluster of 12 atoms, it was no magnetic. In this context, it was previously found that prismane-like molecules could exhibit spin-polarization [31].

Table 5.3: Values for dimensionless parameter β for which C_{12} cluster exhibit ferrimagnetic ground state.

C_{12} isomer	Interval	Total Spin
Iso-a	$0.60 \leq \beta \leq 4.00$	S=1
Iso-b	$0.00 < \beta \leq 4.00$	S=1
Iso-c	$2.40 \leq \beta \leq 4.00$	S=1
Iso-d	$0.00 < \beta \leq 1.30$	S=2
Iso-e	$0.00 < \beta \leq 2.60$	S=1
Iso-f	$0.00 < \beta \leq 2.70$	S=1
Iso-g	$0.00 < \beta \leq 3.60$	S=1
Iso-h	$0.00 < \beta \leq 1.90$	S=1
Iso-i	$0.00 < \beta \leq 1.70$	S=1
Iso-j	$0.00 < \beta \leq 1.70$	S=1
Iso-k	$0.00 < \beta \leq 1.60$	S=1
Iso-l	$0.00 < \beta \leq 2.80$	S=1

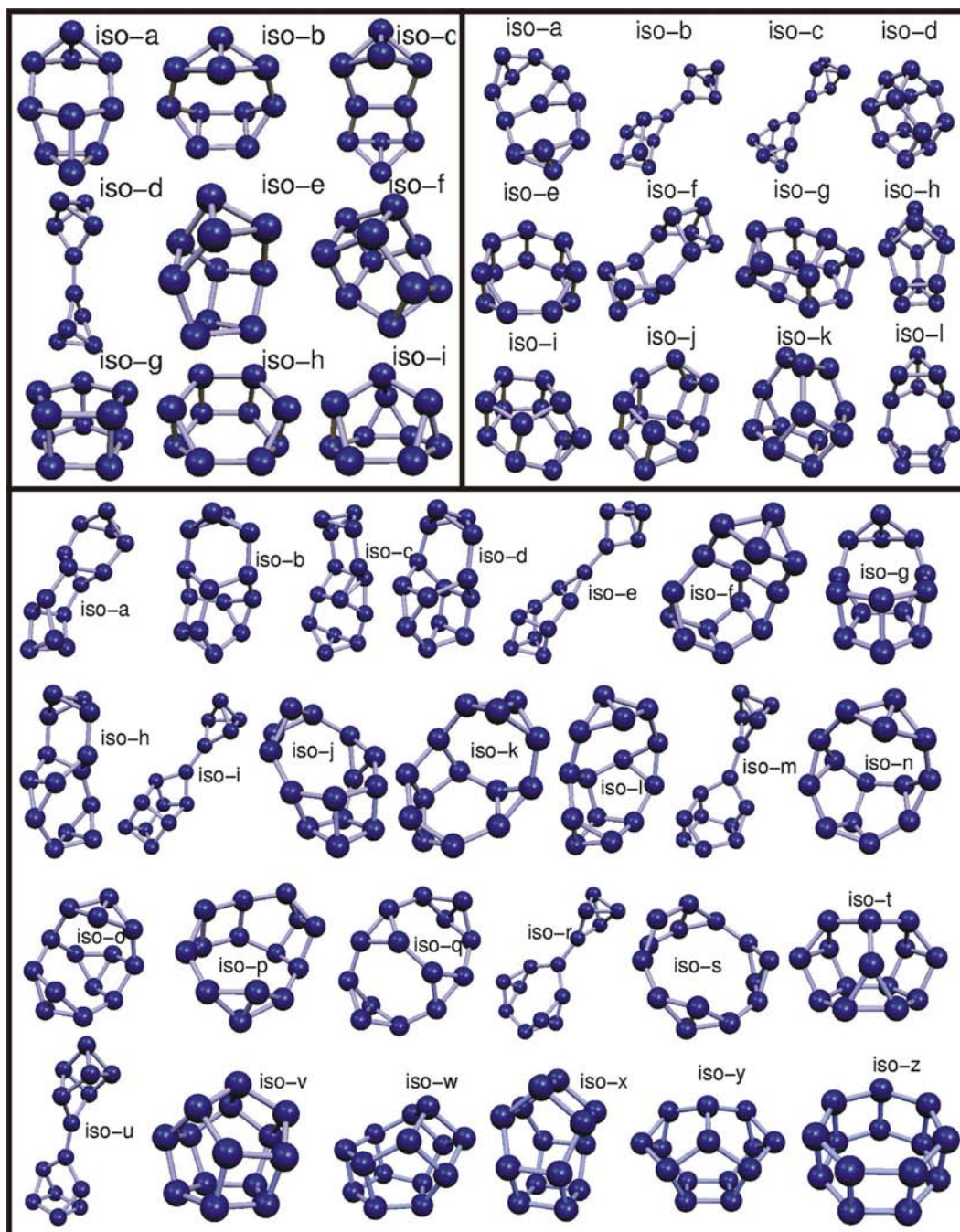


Figure 5.8: Top-left: Geometries of all sp^2 -like carbon clusters with 10 atoms and one π electron per atom. Isomers d to i exhibit a ferrimagnetic ground state. Top-right: Geometries of sp^2 -like carbon clusters with 12 atoms that exhibit a ferrimagnetic ground state. Twenty additional structures were analyzed, displaying a ground state with $S = 0$. Bottom: Ferrimagnetic geometries found for carbon clusters with 14 atoms. All structures have three-coordinated carbon atoms that form highly strained structures, such as carbon chains, as well as triangular and squared rings.

5.5 *Ab initio* calculations of Small Carbon Clusters

In order to find out about the stability and magnetic properties of 10, 12 and 14 atom sp^2 -like clusters (that is, three-coordinated atoms), electronic structure calculations using the Density Functional Theory [32, 33] were carried out within the Local Spin Density Approximation (DFT-LSDA) using the Ceperley-Alder parametrization[34, 35] as implemented in the code SIESTA[36]. Wave functions are represented by a linear combination of pseudo-atomic orbitals using a double-zeta singly polarized basis [37] while core electrons were represented by Norm-conserving Troullier-Martins pseudopotentials in the Kleinman-Bylander non-local form [12, 38]. A full relaxation was performed using conjugate gradient minimization, until all forces were converged to less than $10^{-2}eV/\text{\AA}$, then the total energy and spin polarization was computed.

It was found that from the original 9, 32, and 138 different geometries proposed for 10, 12, and 14 atom clusters, only some of them were both stable and spin-polarized. For the 10 atom clusters, only 7 structures were stable, and from those only 4 structures were spin-polarized. Structures a, g, and i have a total spin of $S = 1$; and structure c has a total spin $S = 2$. The cluster with the lowest total energy was the spin-polarized isomer g, with a binding energy of -8.335 eV/atom, which is about 2.145 eV/atom higher than the graphene binding energy. Isomer g was closely followed by clusters f and i. Results are summarized in table 5.4. Isomer g resembles a prismane molecule, but composed of two pentagonal rings. It was previously found by Izmalkov and Openov [31] that prismane-like molecules could have spin polarization. Also, *ab initio* calculations had a coincidence with the Hubbard model finding magnetism for isomers g and i, but not on isomers a and c, which are magnetic according to the former method. Structures b and d were found unstable, since after relaxation, they unfolded and lost the triple coordination in their atoms.

For the 12-atom clusters, there were 12 structures that were both spin-polarized and stable upon relaxation, as shown in figure 5.9. The most stable 12 atom cluster

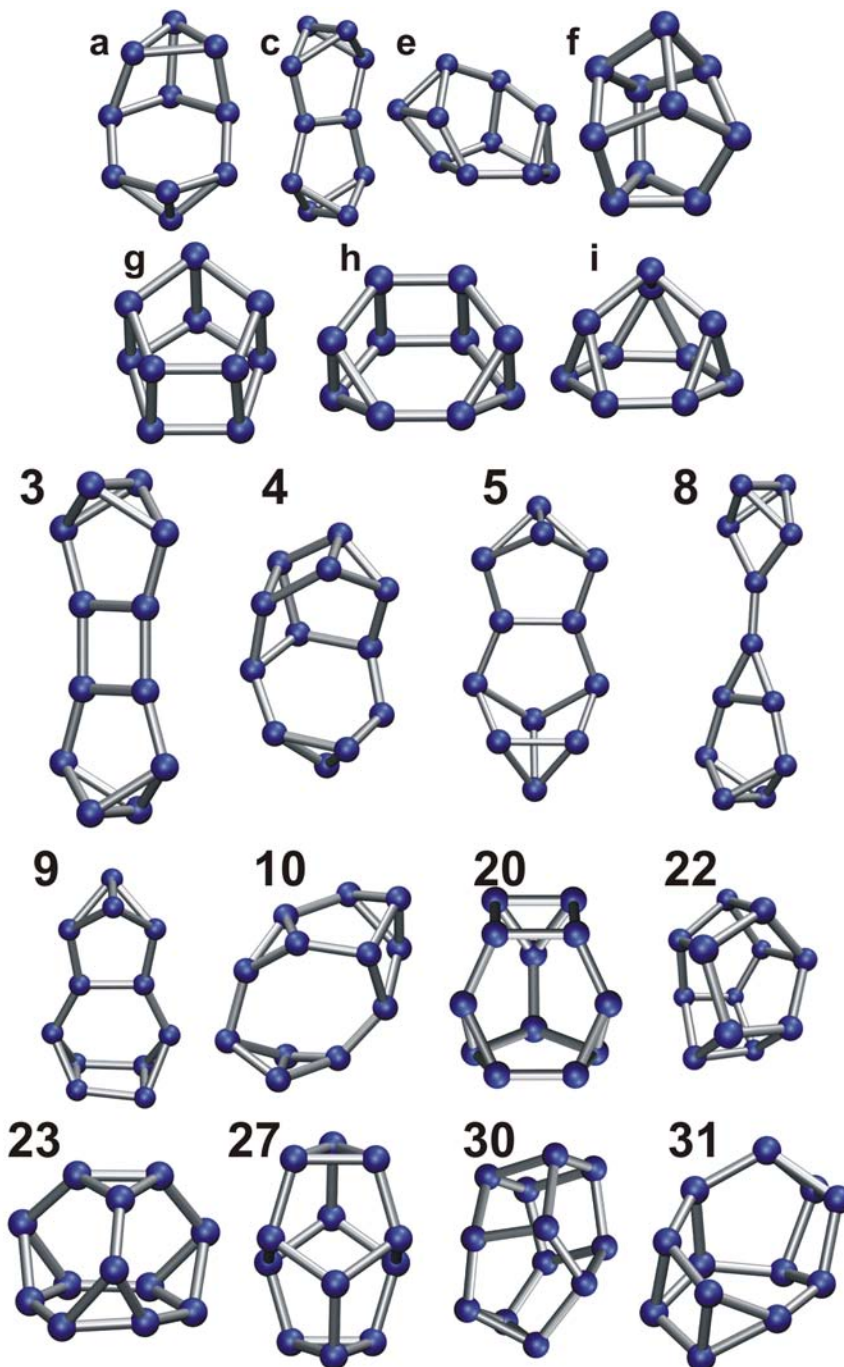


Figure 5.9: Relaxed structures for 10 (letters) and 12 atom (numbers) carbon clusters after relaxation. All stable clusters are shown for the 10 atom case, where clusters a, g, and h have a total spin of $S = 1$ and cluster c has a total spin of $S = 2$. The prismane-like cluster with pentagonal rings is in position g. In the 12 atom case, only spin-polarized clusters that were stable after relaxation are shown. In this case, only cluster number 3 has a total spin of $S = 2$, while the rest have $S = 1$.

was isomer #21, with a binding energy of -8.553 eV/atom and no spin-polarization (not shown). From the spin-polarized clusters, the most stable structure was isomer #30, with a binding energy of -8.495 eV/atom, only 0.0576 eV/atom more than isomer #21, and 1.986 eV/atom more than graphene. The hexagonal prismane-like molecule is not found within the magnetic structures, in coincidence with the Hubbard model. Isomers 22, 30 and 31 are the same as isomers d, i, and j from figure 5.8. All cluster had a total spin of $S = 1$, with the only exception of isomer #3, which had a total spin of $S = 2$.

For the 14-atom cluster case, 138 structures were surveyed in order to find 39 stable and spin-polarized clusters. In this case, the most stable structure is also not spin polarized, and its binding energy is -8.845 eV/atom, which is 1.635 eV/atom higher than in graphene. The most stable spin-polarized cluster is cluster C8, with a binding energy 0.224 eV/atom higher than the previous cluster. Notice that as the cluster size is increased, the binding energy of the most stable cluster is reduced and the energy of the most stable *magnetic* cluster is increased with respect to the former. All stable and spin-polarized clusters of 14 carbon atoms are in figure 5.10. Their ΔE are uniformly distributed between 0.224 and 0.924 eV/atom. Two of these structures have a total spin of $S = 2$, which are E8 and A2. These structures are located in positions eight and two from the highest energy structures. The results

Table 5.4: Total and Binding Energy for several C_{10} clusters, sorted by increasing binding energy. ΔE is the difference in binding energy with the most stable structure. Total spin is also calculated.

C_{10} isomer	Total Energy	Binding Energy	ΔE	Total Spin
iso-g	-1522.39603	-8.335474	0.000000	2
iso-f	-1521.92673	-8.288544	0.046930	0
iso-i	-1521.68131	-8.264002	0.071472	2
iso-h	-1520.98193	-8.194064	0.141410	0
iso-e	-1519.86498	-8.082369	0.253105	0
iso-a	-1518.40314	-7.936185	0.399290	2
iso-c	-1517.47113	-7.842984	0.492490	4

for these structures are summarized in table 5.6.

It has been found that the free double-pentagonal rings exhibit a magnetic moment of $2.0 \mu_B$ (see the DOS in figure 5.11a). However, when this is encapsulated in a C_{60} molecule the magnetic moment is lost due to the interaction between the double-pentagonal rings and C_{60} molecule. The cluster is connected via two bonds with the C_{60} fullerene with an atomic distance of 1.65 \AA approximately and a charge transfer was observed from the cluster to the C_{60} molecule. Figure 5.11b depicts the electronic density of states for the double-5ring inside a C_{60} , exhibiting a reduction of the HOMO-LUMO electronic gap (0.18 eV) in comparison with the single C_{60} fullerene (1.56 eV). Similar results are obtained for the double-pentagonal ring cluster inside C_{70} and C_{80} molecules; the magnetic moment of the cluster disappears. However, states at or close to Fermi level appear. The corresponding electronic density of states can be seen in figures 5.11c and 5.11d. The cluster prefers to attach to the fullerene surface, preferentially to the pentagonal carbon rings.

Table 5.5: Total and Binding Energy for several C_{12} clusters sorted by increasing binding energy. ΔE is the difference in binding energy with the most stable structure. Total spin is also calculated.

C_{12} isomer	Total Energy	Binding Energy	ΔE	Total Spin
iso-30	-1828.794342	-8.4953995	0.057566	2.000000
iso-22	-1828.278515	-8.4524139	0.100552	2.000000
iso-20	-1827.705219	-8.4046392	0.148326	2.000000
iso-27	-1827.048256	-8.3498923	0.203073	2.000000
iso-23	-1826.945499	-8.3413292	0.211636	2.000000
iso-31	-1826.455639	-8.3005076	0.252458	2.000000
iso-5	-1824.554750	-8.1421002	0.410865	2.000000
iso-10	-1824.467053	-8.1347921	0.418173	2.000000
iso-4	-1824.099526	-8.1041648	0.448801	2.000000
iso-9	-1823.587437	-8.0614907	0.491475	2.000000
iso-8	-1820.942101	-7.8410461	0.711919	2.000000
iso-3	-1822.768044	-7.9932080	0.559758	4.000000

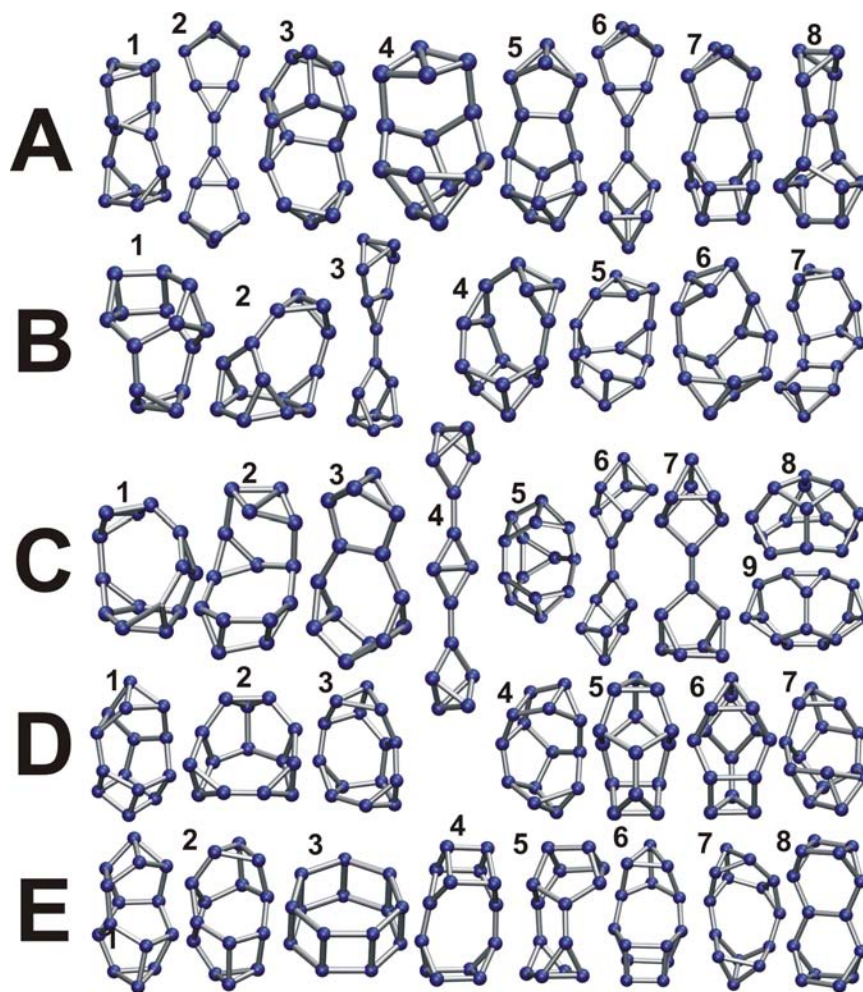


Figure 5.10: Stable structures for 14 atom carbon clusters that exhibit spin-polarization after relaxation. Clusters A2 and E8 exhibit a total spin of $S = 2$, while the rest have $S = 1$. Notice the presence of the prismane-like cluster in position E3, with heptagonal rings.

Table 5.6: Total and Binding Energy for several C_{14} clusters sorted by increasing binding energy. ΔE is the difference in binding energy with the most stable structure. Total spin is also calculated.

C_{14} isomer	Total Energy	Binding Energy	ΔE	Total Spin
iso-C8	-2135.3561	-8.6213034	0.2241111	1
iso-E3	-2134.7654	-8.5791171	0.2662975	1
iso-D6	-2134.3340	-8.5482984	0.2971161	1
iso-D3	-2133.7788	-8.5086410	0.3367736	1
iso-D1	-2133.5047	-8.4890644	0.3563502	1
iso-C5	-2133.2480	-8.4707285	0.3746861	1
iso-D5	-2133.1065	-8.4606196	0.3847949	1
iso-C9	-2132.8827	-8.4446374	0.4007772	1
iso-D7	-2132.8747	-8.4440652	0.4013494	1
iso-D4	-2132.6536	-8.4282677	0.4171469	1
iso-D2	-2132.6475	-8.4278344	0.4175802	1
iso-B2	-2132.1087	-8.3893467	0.4560679	1
iso-B4	-2131.8343	-8.3697516	0.4756630	1
iso-C1	-2131.8201	-8.3687368	0.4766778	1
iso-E2	-2131.8036	-8.3675551	0.4778594	1
iso-E1	-2131.5570	-8.3499401	0.4954744	1
iso-B1	-2131.3373	-8.3342530	0.5111616	1
iso-B5	-2131.1079	-8.3178632	0.5275514	1
iso-A4	-2131.0659	-8.3148671	0.5305475	1
iso-B6	-2131.0283	-8.3121761	0.5332384	1
iso-E6	-2130.9358	-8.3055732	0.5398414	1
iso-A8	-2130.9084	-8.3036129	0.5418016	1
iso-E4	-2130.2155	-8.2541203	0.5912943	1
iso-A7	-2130.2053	-8.2533947	0.5920199	1
iso-A5	-2130.1660	-8.2505851	0.5948295	1
iso-E7	-2130.0936	-8.2454147	0.5999999	1
iso-A3	-2129.9394	-8.2344013	0.6110133	1
iso-E5	-2129.9072	-8.2321006	0.6133140	1
iso-C3	-2129.6283	-8.2121805	0.6332341	1
iso-B7	-2128.8886	-8.1593424	0.6860721	1
iso-C2	-2128.8186	-8.1543414	0.6910732	1
iso-E8	-2128.2122	-8.1110293	0.7343853	2
iso-A1	-2128.0637	-8.1004229	0.7449916	1
iso-C7	-2127.4934	-8.0596880	0.7857266	1
iso-C6	-2127.2552	-8.0426722	0.8027424	1
iso-B3	-2127.0331	-8.0268060	0.8186086	1
iso-A6	-2126.8808	-8.0159254	0.8294892	1
iso-A2	-2126.2061	-7.9677329	0.8776816	2
iso-C4	-2125.5527	-7.9210609	0.9243536	1

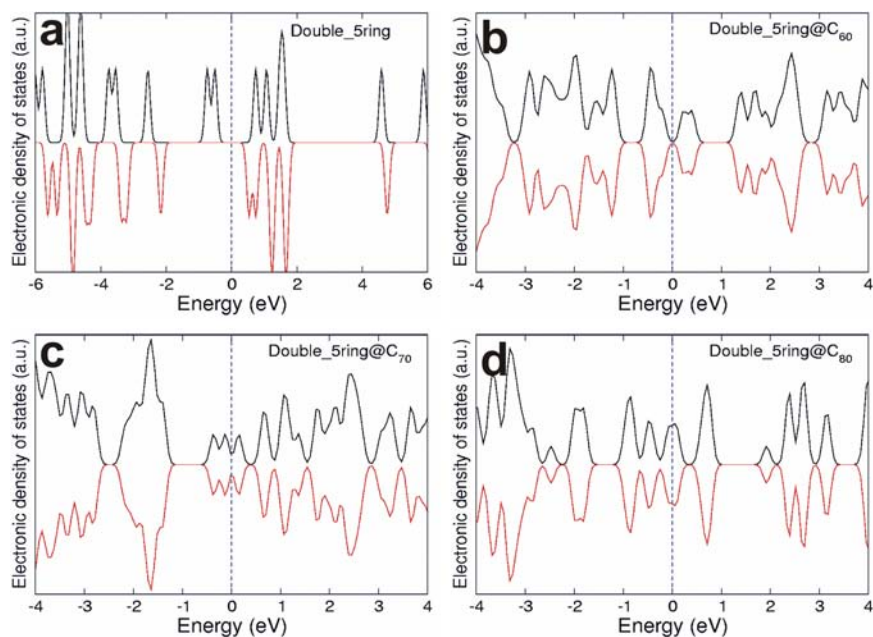


Figure 5.11: Electronic Density of States (DOS) calculated for (a) an isolated pentagonal prismane-like molecule (iso-g from figure 5.9. b) Prismane-like cluster inside a C₆₀ molecule, (c) a C₇₀ molecule, and (d) a C₈₀ fullerene. Each figure has independent Spin-up (black) and Spin-down (red) plots. The system was first relaxed using conjugate gradient. The Fermi level has been shifted to zero, and represented by the vertical dashed line.

5.6 Conclusions

The coalescence induce mode, or CIM, was identified in heat-treated double-walled carbon nanotubes. Although different groups have observed this vibrational mode before in multiwalled carbon nanotubes, they were not conclusive about the carbon structure that gave origin to this vibration. Further experimental work concluded that these chains are likely located in the interstitials of the nanotube hexagonal arrangement. The proposed model of short linear carbon chains has a reasonable fit within the experimental data, and seems like a possible explanation to this behavior. Additional calculations with Hartree-Fock methods, gave a confirmation that short carbon chains could have vibrational modes with frequencies close to the experimental values.

Small Carbon clusters can be synthesized spontaneously during irradiation of graphite; or during chemical vapor depositions with a cooling process fast enough to avoid annealing of the sample. These carbon clusters could eventually be stabilized by encapsulation in larger carbon forms, like fullerenes or nanotubes. Their properties are still very dependant of their environment, but it is possible that these clusters could exhibit unusual magnetic properties. It was shown by *ab initio* calculations that isolated small carbon clusters are spin polarized, and although its polarization is very sensitive to their environment, they remain stable after encapsulation inside larger carbon forms. It is expected that these clusters, although preserving a triple coordination of their atoms, do not posses an sp^2 hybridization, since the large strain induced by bonding angles will push for an sp^3 hybridization, leaving dangling bonds that could mix in dangling-bond states, as seen in chapter 4, in order to reduce their energy. These dangling bonds make these clusters chemically active, and combined with their low binding energy, support the hypothesis that they would be highly unstable.

References

- [1] M. Endo, Y.A. Kim, T. Hayashi, H. Muramatsu, M. Terrones, R. Saito, F. Villalpando-Paez, S.G. Chou, and M.S. Dresselhaus. Nanotube coalescence-inducing mode: A novel vibrational mode in carbon systems. *Small*, 2:1031–1036, 2006.
- [2] M. Endo, H. Muramatsu, T. Hayashi, Y. A. Kim, M. Terrones, and M. S. Dresselhaus. Nanotechnology: ‘buckypaper’ from coaxial nanotubes. *Nature*, 433:476, 2005.
- [3] M. Endo, H. Muramatsu, T. Hayashi, Y.-A. Kim, G. Van Lier, J.-C. Charlier, H. Terrones, M. Terrones, and M.S. Dresselhaus. Atomic nanotube welders: Boron interstitials triggering connections in double-walled carbon nanotubes. *Nano Letters*, 5:1099–1105, 2005.
- [4] X. Zhao, Y. Ando, Y. Liu, M. Jinno, and T. Suzuki. Carbon nanowire made of a long linear carbon chain inserted inside a multiwalled carbon nanotube. *Phys. Rev. Lett.*, 90:187401, 2003.
- [5] M. Jinno, Y. Ando, S. Bandow, J. Fan, M. Yudasaka, and S. Iijima. Raman scattering study for heat-treated carbon nanotubes: The origin of $\approx 1855\text{cm}^{-1}$ raman band. *Chemical Physics Letters*, 418:109–114, 2006.
- [6] Á. Ruzsnyák, V. Zólyomi, J. Kürti, S. Yang, and M. Kertesz. Bond-length alternation and charge transfer in a linear carbon chain encapsulated within a single-walled carbon nanotube. *Physical Review B*, 72:155420, 2005.
- [7] J. Kurti, C. Magyar, A. Balazs, and P. Rajczy. Vibrational analysis for short carbon chains with alternating and cumulenic structure. *Synthetic Metals*, 71:1865–1866, 1995.
- [8] C. Fantini, E. Cruz, A. Jorio, M. Terrones, H. Terrones, G. Van Lier, J-C Charlier, M. S. Dresselhaus, R. Saito, Y. A. Kim, T. Hayashi, H. Muramatsu, M. Endo, and M. A. Pimenta. Resonance raman study of linear carbon chains

- formed by the heat treatment of double-wall carbon nanotubes. *Physical Review B*, 73:193408, 2006.
- [9] H. Muramatsu, Y.A. Kim, T. Hayashi, M. Endo, M. Terrones, and M.S. Dresselhaus. Oxidation and thermal stability of linear carbon chains contained in thermally treated double-walled carbon nanotubes. *Small*, 3:788–792, 2007.
- [10] M. J. Frisch, G. W. Trucks, H. B. Schlegel, G. E. Scuseria, M. A. Robb, J. R. Cheeseman, J. A. Montgomery, Jr., T. Vreven, K. N. Kudin, J. C. Burant, J. M. Millam, S. S. Iyengar, J. Tomasi, V. Barone, B. Mennucci, M. Cossi, G. Scalmani, N. Rega, G. A. Petersson, H. Nakatsuji, M. Hada, M. Ehara, K. Toyota, R. Fukuda, J. Hasegawa, M. Ishida, T. Nakajima, Y. Honda, O. Kitao, H. Nakai, M. Klene, X. Li, J. E. Knox, H. P. Hratchian, J. B. Cross, V. Bakken, C. Adamo, J. Jaramillo, R. Gomperts, R. E. Stratmann, O. Yazyev, A. J. Austin, R. Cammi, C. Pomelli, J. W. Ochterski, P. Y. Ayala, K. Morokuma, G. A. Voth, P. Salvador, J. J. Dannenberg, V. G. Zakrzewski, S. Dapprich, A. D. Daniels, M. C. Strain, O. Farkas, D. K. Malick, A. D. Rabuck, K. Raghavachari, J. B. Foresman, J. V. Ortiz, Q. Cui, A. G. Baboul, S. Clifford, J. Cioslowski, B. B. Stefanov, G. Liu, A. Liashenko, P. Piskorz, I. Komaromi, R. L. Martin, D. J. Fox, T. Keith, M. A. Al-Laham, C. Y. Peng, A. Nanayakkara, M. Challacombe, P. M. W. Gill, B. Johnson, W. Chen, M. W. Wong, C. Gonzalez, and J. A. Pople. Gaussian 03, Revision B.05. Gaussian, Inc., Wallingford, CT, 2004.
- [11] X. Gonze, J. M. Beuken, R. Caracas, F. Detraux, M. Fuchs, G. M. Rignanese, L. Sindic, M. Verstraete, G. Zerah, F. Jollet, M. Torrent, A. Roy, M. Mikami, Ph. Ghosez, J. Y. Raty, and D. C. Allan. First-principles computation of material properties: the abinit software project. *Computational Materials Science*, 25:478–492, 2002.
- [12] N. Troullier and J. L. Martins. Efficient pseudopotentials for plane-wave calculations. *Physical Review B*, 43:1993–2006, 1991.
- [13] B.K. Agrawal, S. Agrawal, and S. Singh. Structural and vibrational properties

- of small carbon clusters. *Journal of Nanoscience and Nanotechnology*, 5:442–447, 2005.
- [14] O. Dubay and G. Kresse. Accurate density functional calculations for the phonon dispersion relations of graphite layer and carbon nanotubes. *Physical Review B*, 67:035401, 2003.
- [15] P. Esquinazi, D. Spemann, R. Höhne, A. Setzer, K.-H. Han, and T. Butz. Induced magnetic ordering by proton irradiation in graphite. *Phys. Rev. Lett.*, 91:227201, 2003.
- [16] R. Astala, M. Kaukonen, R. M. Nieminen, G. Jungnickel, and T. Frauenheim. Properties of small carbon clusters inside the c_{60} fullerene. *Physical Review B*, 65:245423, 2002.
- [17] Y. Liu, R. O. Jones, X. Zhao, and Y. Ando. Carbon species confined inside carbon nanotubes: A density functional study. *Physical Review B*, 68:125413, 2003.
- [18] N. Park, M. Yoon, S. Berber, J. Ihm, E. Osawa, and D. Tománek. Magnetism in all-carbon nanostructures with negative gaussian curvature. *Physical Review Letters*, 91:237204, 2003.
- [19] A.N. Andriotis, M. Menon, R.M. Sheetz, and L. Chernozatonskii. Magnetic properties of C_{60} polymers. *Physical Review Letters*, 90:026801, 2003.
- [20] J. A. Chan, B. Montanari, J. D. Gale, S. M. Bennington, J. W. Taylor, and N. M. Harrison. Magnetic properties of polymerized C_{60} : The influence of defects and hydrogen. *Physical Review B*, 70:041403, 2004.
- [21] J. Hubbard. Electron correlations in narrow energy bands. *Proc. R. Soc. A*, 276:238, 1963.
- [22] J. Hubbard. Electron correlations in narrow energy bands iii. an improved solution. *Proc. R. Soc. A*, 281:401, 1964.

- [23] J. Kanamori. Electron correlation and ferromagnetism of transition metals. *Prog. Theor. Phys.*, 30:275, 1963.
- [24] M.C. Gutzwiller. Effect of correlation on the ferromagnetism of transition metals. *Physical Review Letters*, 10:159, 1963.
- [25] F. López-Urías and G. M. Pastor. Exact numerical study of the ground-state magnetic properties of clusters. *Physical Review B*, 59:5223–5232, 1999.
- [26] C. Lanczos. An iteration method for the solution of the eigenvalue problem of linear differential and integral operators. *J. Res. Nat. Bur. Stand.*, 45:255, 1950.
- [27] L. Bergomi, J. P. Blaizot, Th. Jolicœur, and E. Dagotto. Generalized spin-density-wave state of the hubbard model for C_{12} and C_{60} clusters. *Physical Review B*, 47:5539–5542, 1993.
- [28] G. Stollhoff. Anomalous electron-lattice coupling in C_{60} . *Physical Review B*, 44:10998–11000, 1991.
- [29] D. Coffey and S. A. Trugman. Magnetic properties of undoped C_{60} . *Physical Review Letters*, 69:176–179, 1992.
- [30] S. Chakravarty, M.P. Gelfand, and S. Kivelson. Electronic Correlation Effects and Superconductivity in Doped Fullerenes. *Science*, 254:970–974, 1991.
- [31] A.A. Izmalkov and L.A. Openov. Metastable spin-polarized carbon clusters C_8 and their ensembles. *Phys. Low-Dim. Struct.*, 7/8:65–76, 2002.
- [32] P. Hohenber and W. Kohn. Inhomogeneous electron gas. *Physical Review*, 136: B864–B871, 1964.
- [33] W. Kohn and L. J. Sham. Self-consistent equations including exchange and correlation effects. *Physical Review*, 140:A1133–A1138, 1965.
- [34] D. M. Ceperley and B. J. Alder. Ground state of the electron gas by a stochastic method. *Physical Review Letters*, 45:566–569, 1980.

-
- [35] J.P. Perdew and A. Zunger. Self-interaction correction to density-functional approximations for many-electron systems. *Physical Review B*, 23:5048, 1981.
- [36] J. M. Soler, E. Artacho, J. D. Gale, A. García, J. Junquera, P. Ordejón, and D. Sánchez-Portal. The siesta method for ab-initio order-N materials simulation. *Journal of Physics: Condensed Matter*, 14:2745–2779, 2002.
- [37] J. Junquera, O. Paz, D. Sánchez-Portal, and E. Artacho. Numerical atomic orbitals for linear-scaling calculations. *Physical Review B*, 64(23):235111, Nov 2001. doi: 10.1103/PhysRevB.64.235111.
- [38] L. Kleinman and D. M. Bylander. Efficacious form for model pseudopotentials. *Physical Review Letters*, 48:1425–1428, 1982.

Chapter 6

Perspectives

It has been discussed in this dissertation that carbon nanotubes have a great potential for technological applications. All these applications of carbon nanotubes rely on the interactions with their environment. However, carbon nanotubes are highly inert, but the interactions can be promoted by inserting atoms of different elements that could modify the nanotube's physical and chemical properties.

Another interesting method for promoting these interactions is by covalent functionalization, that is, inserting functional groups that can trigger specific chemical reactions. Covalent functionalization of carbon nanotubes has been widely used to add radical groups but at expenses of nanotube mechanical and electronic properties, and normally is an irreversible modification which requires additional reaction steps and separations.

Non-covalent functionalization approaches, such as ionic or van der Waals interactions, are useful when fine tuning of nanotube properties or a reversible functionalization is needed. Due to their high polarizability and smooth surface, carbon nanotubes can form strong van der Waals interactions [1].

In studies of adsorption of gaseous nitrogen, it has been found that SWNT have a large surface area (ca. 400 m²/g), and that this increases after treatment in hydrochloric acid due to a higher availability of the interior surface of the nanotubes [2]. This was also true for benzene and methanol after treating in nitric acid. It has been also observed experimentally that Ne [3], Xe [4], and methane [5] adsorb only in groove sites of the nanotube bundles, with a binding energy that is 75%

greater than the same molecule in planar graphite, increase that is in accordance to theoretical calculations [6].

Other interesting interactions between adsorbed molecules and nanotubes is that of $\pi-\pi$ stacking between SWNT and organic molecules. A study from Sumanasekera et al. on cyclic hydrocarbons with increasing number of π electrons (cyclohexane, cyclohexene, cyclohexadiene and benzene) found that the highest adsorption energy was for benzene, which has the largest π -electron system, and the lowest energy was for cyclohexane, which has no π -electrons [7]. In that sense, studies of H.J. Dai's group with pyrene, a molecule with a large π -electron aromatic system, found that it has a strong interaction with the nanotube surface [8, 9]. Derivatives of pyrene were deposited in the surface of SWNT with a high surface coverage. The interaction is so strong that functionalized pyrenes were used to anchor biomolecules [8] and polymerization catalyst to the nanotubes [9]. Other organic groups successfully attached to nanotubes surfaces via non-covalent interactions are anthracenes [10], porphyrins [11], and phthalocyanins [12].

Experimentally, it can be difficult to identify whether an endohedral or exohedral adsorption occurred. Infrared spectroscopy (IR) is a very useful technique in the study of adsorbed molecules into SWNT, since dispersive interactions cause a softening of the adsorbed molecule bonds, resulting in a red-shift in the vibrational modes of the IR spectra. Depending of the magnitude of the shift, it is possible to identify the adsorption as endohedral or exohedral [13].

The aim is to theoretically study and characterize physically and chemically adsorbed organic molecules in the surface of pristine and doped carbon nanotubes, graphite nanoribbons, metallic surfaces and other systems of interest, by means of ab initio first principles calculations, using the density functional theory approach (DFT). Systems of interest include the adsorption of alkanes, aromatic, and polyaromatic molecules into nanotubes. The adsorption properties of these molecules on nitrogen, boron, and phosphorus doped nanocarbons are also considered.

First principles molecular dynamics (MD) will be used to study the adsorption process, identify possible configurations, and evaluate the thermal stability of the adsorbate into the nanotube or nanoribbon. The effects of adsorbates into nanotubes

electronic structure, vibrational properties as well as effects in linear response transport properties will be also studied. The variations in adsorbate molecules due to the interactions with the host systems, such as bending (for large aromatic molecules), bond relaxation due to charge transfer, and changes in vibrational properties will be also considered.

The interactions leading to adsorption will have effects in vibrational spectroscopic data, such as Infrared, Raman or Inelastic Neutron Scattering (INS). Use of public and commercially available ab-initio and spectroscopy codes such as SIESTA, VASP, abinit, and aCLIMAX will help in the determination of these effects, by examining changes in the spectroscopic data, such as peak shifts, as well as the appearance, disappearance, broadening or splitting of vibrational modes.

Collaboration with experimental groups will be looked forward, analyzing experimental spectroscopic data and comparing with theoretical spectroscopic predictions in order to have a better understanding of the adsorbate–host interactions.

References

- [1] L.A. Girifalco, M. Hodak, and R.S. Lee. Carbon nanotubes, buckyballs, ropes, and a universal graphitic potential. *Physical Review B*, 62:13104–13110, 2000.
- [2] M. Eswaramoorthy, R. Sen, and C.N.R. Rao. A study of micropores in single-walled carbon nanotubes by the adsorption of gases and vapors. *Chemical Physics Letters*, 304:207–210, 1999.
- [3] S. Talapatra, A.Z. Zambano, S.E. Weber, and A.D. Migone. Gases do not adsorb on the interstitial channels of closed-ended single-walled carbon nanotube bundles. *Physical Review Letters*, 85:138–141, 2000.
- [4] A.J. Zambano, S. Talapatra, and A.D. Migone. Binding energy and monolayer capacity of Xe on single-wall carbon nanotube bundles. *Physical Review B*, 64:075415, 2001.
- [5] S.E. Weber, S. Talapatra, C. Journet, A. Zambano, and A.D. Migone. Determination of the binding energy of methane on single-walled carbon nanotube bundles. *Physical Review B*, 61:13150–13154, 2000.
- [6] G. Stan, M.J. Bojan, S. Curtarolo, S.M. Gatica, and M.W. Cole. Uptake of gases in bundles of carbon nanotubes. *Physical Review B*, 62:2173–2180, 2000.
- [7] G.U. Sumanasekera, B.K. Pradhan, H.E. Romero, K.W. Adu, and P.C. Eklund. Giant thermopower effects from molecular physisorption on carbon nanotubes. *Physical Review Letters*, 89:166801, 2002.
- [8] R.J. Chen, Y. Zhang, D. Wang, and H. Dai. Noncovalent sidewall functionalization of single-walled carbon nanotubes for protein immobilization. *Journal of the American Chemical Society*, 123:3838–3839, 2001.
- [9] F.J. Gómez, R.J. Chen, D. Wang, R.M. Waymouth, and H. Dai. Ring opening metathesis polymerization on non-covalently functionalized single-walled carbon nanotubes. *Chemical Communications*, pages 190–191, 2003.

- [10] J. Zhang, J.-K. Lee, Y. Wu, and R.W. Murray. Photoluminescence and electronic interaction of anthracene derivatives adsorbed on sidewalls of single-walled carbon nanotubes. *Nano Letters*, 3:403–407, 2003.
- [11] H. Li, B. Zhou, Y. Lin, L. Gu, W. Wang, K.A.S. Fernando, S. Kumar, L.F. Allard, and Y.-P. Sun. Selective interactions of porphyrins with semiconducting single-walled carbon nanotubes. *Journal of the American Chemical Society*, 126:1014–1015, 2004.
- [12] W. Qiu X. Wang, Y. Liu and D. Zhu. Immobilization of tetra-*tert*-butylphthalocyanines on carbon nanotubes: a first step towards the development of new nanomaterials. *Journal of Materials Chemistry*, 12:1636–1639, 2002.
- [13] W.-L. Yim, O. Byl, Jr. J.T. Yates, and J.K. Johnson. Vibrational behavior of adsorbed CO₂ on single-walled carbon nanotubes. *The Journal of Chemical Physics*, 120:5377–5386, 2004.